Low Temperature Electrolysis of Rare Earth Elements: Immobilization of Rare Earth Elements in Novel Cathodes

A Dissertation
Presented in Partial Fulfillment of the Requirements for the
Degree of Doctor of Philosophy
with a
Major in Nuclear Engineering
in the
College of Graduate Studies
University of Idaho
by
Eugene Tettey Engmann

Approved by:
Major Professor: Haiyan Zhao, Ph.D.
Committee Members: Indrajit Charit, Ph.D.; Vivek Utgikar, Ph.D.; Luis Diaz-Aldana, Ph.D.
Department Administrator: Indrajit Charit, Ph.D.

May 2023

Abstract

The electrochemical immobilization of rare earth elements (REEs) provides a promising approach for retrieving REEs from mining ores and end-of-life products (recyclability). Conventional methods such as solvents extraction, ion exchange, and molten salt reduction have proven to be effective ways of extracting REEs but consume lots of energy or chemicals or both. Furthermore, during application of these conventional approaches, there is degradation of the anode and electrolyte. An alternative and promising pathway for REEs capture is low temperature (< 40 °C) electrochemical immobilization of REEs using metal and metal oxides in aqueous solution. The use of metal oxide lies in the fact that the disproportionation reaction of some metal oxides such as Ga_2O, can entrain metal ions of interest (a novel approach being investigated for REE capture.) from aqueous solution. On the other hand, certain metal oxides such as MnO_2, or graphite base materials provide weaker van der Waal gaps between atomic lattices to host potential metal ions such as REEs (another novel approach). This approach addresses several gaps and overcomes disadvantages of current conventional methods such as high temperature, large amount of chemical exhaustion, anode degradation, high safety risk and hazard prone environments.

My Ph.D. work seeks to investigate two methods for REEs immobilization. The first is the electrochemical formation of REE alloys. This would employ a non-toxic low temperature melting metal, Ga as cathode. The electrochemistry of the REE, Pr, will be investigated at a liquid Ga cathode to study the possibility of Pr deposition on the Ga cathode. Alloy formation will also harness the disproportionation of Ga oxide for the entrainment of REEs. Secondly, immobilization of REEs into metal oxides via pseudo-intercalation and pseudo-capacitance will be investigated and studied. Intercalation will take advantage of the weaker van der Waal forces between the gaps of the atomic lattices of certain metal oxides for the possible capture of REEs.

Electrochemical techniques such as cyclic voltammetry and chronoamperometry are employed to evaluate various cathodic materials including Ga, MnO_2, and turbostratic carbon (Vulcan XC-72R). This work will focus on the REEs Pr and Nd. Electrochemistry measurements will be performed, taking into account REE concentration, metal oxide loading capacities, and reduction potentials. Following initial experimentation, it was observed that REEs were immobilized into various cathodes. These results are encouraging for the recovery of REEs using low temperature electrochemical reduction beyond established methods.

Acknowledgments

I would like to acknowledge the tremendous support from my advisor Dr. Haiyan Zhao, for her advice and mentorship throughout my PhD program. And for helping me secure the opportunity to do my research with the Idaho National Laboratory. I would also like to thank Dr. Tedd Lister and Dr. Luis Diaz for their unwavering mentorship and interest in seeing that I succeeded during my PhD program. Their expertise and background enabled the success of my research. I would also like to thank Byron White and Brittany Tague for helping me with the waves of analysis I had to perform on experimental work. I would like to thank my group members for cheering me on every day in the laboratory. I would like to also thank the Idaho National Laboratory along with the Critical Materials Institute for providing the necessary funding, training, skills, and space to accomplish this work.

Dedication

I would love to thank my wife Dora Engmann for her unwavering support during my PhD work and my children Mikhael-Eugene, Mykhie-Elaine, and Mykhyn-Elixir for rooting for their daddy. I would also like to thank my dad and mom for their encouragement and support during these past years, and their investments into my education as a child. I would love to thank my siblings and dear friends who were always there to lend a helping hand. I would love to thank and finally dedicate this work to my friend Winfred Sowah for his unrelenting words of encouragement and for being a beacon of hope.

Table of Contents

List of Tables

List of Figures

Statement of Contribution

Eugene Engmann: Facilitator of experiments, Compilation of results, Document writing, and editing

Tedd Lister: Originator of ideas for low temperature separation on REEs in aqueous and ionic media, Mentor at Idaho National Laboratory, Technical editor of published papers

Luis Diaz: Mentor at Idaho National Laboratory, Technical editor of published papers

Haiyan Zhao: Major Professor, Technical advice, Document editing

Chapter 1: Introduction to Rare Earth Elements: Extractive Technologies – A Review

Importance and Significance of Rare Earth Elements

Designated as elements Scandium (Sc), Yttrium (Y), Lanthanum (La), Cerium (Ce), Praseodymium, (Pr), Neodymium (Nd), Promethium (Pr), Samarium (Sm), Europium (Eu), Gadolinium (Gd), Terbium (Tb), Dysprosium (Dy), Holmium (Ho), Erbium (Er), Thulium (Tm), indium (In), Ytterbium (Yb) and Lutetium (Lu) with atomic number from 21, 39 and 57 to 71 [1]–[8] respectively, rare earth elements (REEs) have garnered interest among researchers. This is due to the intrinsic improvements they contribute to materials they are employed in [9]. REEs are used in metal alloys, rechargeable batteries, automotive catalysts, ceramics, cracking catalysts, polishing powders, permanent magnets, lighting displays, laser and wavelength amplifiers, military defense applications and agricultural applications [1], [10]–[13]. Table 1.1 is a list of the many uses of REEs and the percentages of REEs employed in these technologies [14] [15]. REEs also play a critical role in the world's shift to a greener and carbon free economy. With rise in electric vehicles, hybrid cars, and the demand of permanent magnets, rechargeable batteries and a host of other technologies, the demand and prices for/of REEs have skyrocketed [15], [16].

Table 1.1 Percentage of REEs used in application listed*[15]

Application	La	Ce	Pr	Nd	Sm	Eu	Gd	Tb	Dy	Y	Other
Magnets			23.4	69.4			2	0.2	5		
Battery alloys	50	33.4	3.3	10	3.3						
Metallurgy	26	52	5.5	16.5							
Auto catalysts	5	90	2	3							
FCC	90	10									
Polishing powders	31.5	65	3.5								
Glass additives	24	66	1	3						2	4
Phosphors	8.5	11				4.9	1.8	4.6		69.2	
Ceramics	17	12	6	12						53	
Others	19	39	4	15	2		1			19	

*The percentages listed in Table 1 vary from manufacturer to manufacturer

Forecasting from 2015 to 2025, in 2011, the United states department of energy (DOE) [17] pronounced Nd, Dy, Eu, Y, and Tb as the most critical materials with a high supply risk as seen in Figure 1.1. Furthermore, among the leading technologies for clean energy which employ the use of REEs, DOE lists them as photovoltaic films coating, wind turbines magnets, vehicle magnets and

batteries, and lighting phosphors [17]. Also, with the increase and growth of technology, the demand for REEs such as Nd and Dy, is expected to grow to a staggering 2600% to 700% respectively [18].

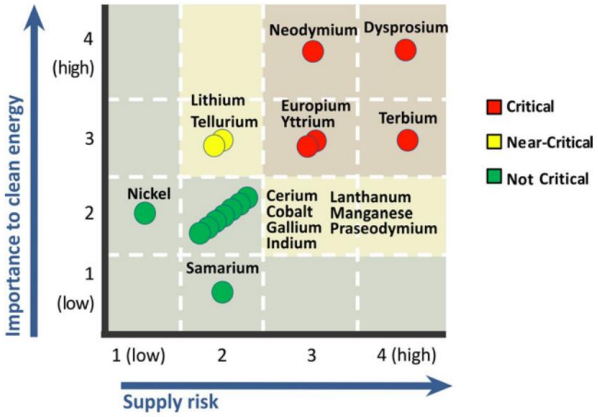

Figure 1.1 Department of Energy Medium Term (2015-2025) Criticality Matrix showing the most critical REEs [17].

However, majority of the world REEs are mined in China, a major stakeholder in the REE market [19][20]. To meet its increasing domestic need for REEs, China reduced its export supply of REEs from 50,145 tons to 31,130 tons in 2009 [15], and this number keeps declining. In recent years, the recycling of REEs from end-of-life consumer products has gained traction among researchers. This is in part because of the three-pillar strategy of DOE to address the issue of critical materials [17]. DOE identifies these pillars as:

- Having diversified global supply chain
- Developing substitutes to support a diversified supply chain
- Recycling and Reuse

The second and third pillars focus on the development of clean energy technologies to extract REEs in ways that create flexibility and meet the REE supply need. Furthermore, recycling will help reduce the demand of newly extracted materials [17]. This is one of the motivations for the present work. This work discusses current technologies for the separation of REEs and greener technology for the immobilization of REEs.

Review on Existing Technologies for REEs Extraction

REEs are found naturally as oxides in the form of silicates, carbonates, phosphates and titano-tantaloniobates [21], and in very little quantities in the earth's crust as seen in Table 1.2. Conventional methods for the chemical and electrochemical reduction, separation and capture of REEs include electrowinning or molten salt electrolysis [22]–[26], metallothermic reduction [27]–[34], solvent

extraction [1], and ion exchange extraction [1]. These processes are either chemical intensive; in the case of solvents extraction, or energy intensive, or create hazardous environmental conditions. The following is an overview of various methods used for REEs extraction and recovery.

Table 1.2. Typical composition of lanthanides in monazite, xenotime, and bastnasite [21]

	Lanthanide oxide	Monazite/%	Xenotime/%	Bastnasite/%
Light	La_2O_3	23	0.5	32
	CeO_2	46.5	5	49
	Pr_6O_{11}	5.1	0.7	4.4
	Nd_2O_3	18.4	2.2	13.5
Heavy	Sm_2O_3	2.3	1.9	0.5
	Eu_2O_3	0.07	0.2	0.1
	Gd_2O_3	1.7	4	0.3
	Tb_4O_7	0.16	1	0.01
	Dy_2O_3	0.52	8.7	0.03
	Ho_2O_3	0.09	2.1	0.01
	Er_2O_3	0.13	5.4	0.01
	Tm_2O_3	0.013	0.013	0.2
	Yb_2O_3	0.061	6.2	0.01
	Lu_2O_3	0.006	0.4	0.1
	Y_2O_3	2	60.8	0.1

Electrowinning of REEs using Molten Salt Electrolysis

Electrowinning of REEs is an extractive method which uses a direct current to extract metals from their oxides, chlorides, or fluorides with the aid of an electrolytic cell [22] as seen in Figure 1.2. The electrolytic cell consists of an insoluble anode commonly made from graphite, lead [24], or titanium coated with platinum [23], and a suitable cathode such as tungsten [35] for the deposition of the metal of interest [22]. During electrowinning of REEs, the metal of interest is first dissolved into chloride solutions using acids [23]. Under an external potential, metal ions are transported from the electrolyte to the cathode and electrochemically reduced with potentials as low as 4 V. [36]. Commons metals that have been electrowon are cobalt, zinc, copper, manganese, titanium and nickel [25] [35], [37]–[39]. The decomposition potential of a single salt can be described using the equation:

$$V_d = -\frac{\Delta G}{nF} \qquad [1.1]$$

where V_d is the decomposition potential, ΔG is the change is free energy, and n is the valence potential [40]. The decomposition potential can be derived by the Nernst equation:

$$E_{M^{n+}/M} = E^0 + \frac{RT}{nF}\ln\frac{a_{M^{n+}}}{a_M} \qquad [1.2]$$

where E^0 is the electrode potential, n is the number of electrons, F is Faradays constant, R is the gas constant, T is the absolute temperature, $a_{M^{n+}}$ and a_M are the activities of the M^{n+} and reduced metal species respectively [41] . Based on Nernst equation, as temperature increases, the decomposition potential decreases.

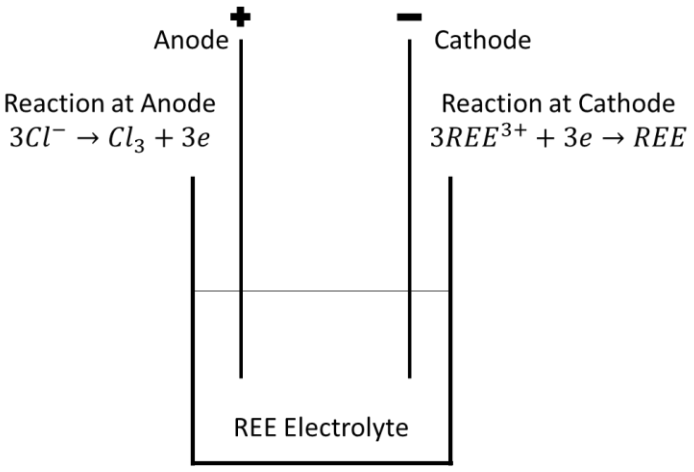

Figure 1.2 Basic electrowinning cell.

Electrowinning of REEs have gained attention in recent years owing to growth of REEs alloys [26], [42]–[45]. Temperature plays a significant role in the electrowinning of the wide range of REEs. Low melting temperature REEs such as lanthanum, cerium, praseodymium, and neodymium can be liquified via electrolysis with chlorides between 650 °C and 1100 °C [46]. High melting temperature REEs such as gadolinium, dysprosium, and yttrium can be recovered using fluorides salts at temperatures ranging from 1300 to 1700 °C. Due to exhaust gas pollutions, low yields and the ease of moisture adsorption, technology involving REE chlorides [35] was halted. Current efficiency is affected by the presence of multivalent REEs such as Sm and Eu, and the formation of oxychlorides during electrolysis. For example, $SmCl_3$ reacts with Sm in the electrolyte to produce $SmCl_2$ at the anode or cathode simultaneously. The reduction of Sm^{3+} to Sm^{2+} consumes a high amount of current and leads to low efficiency [36]. Furthermore, with low conductivity, high melting point and low solubility, oxychlorides increase the viscosity of the electrolyte, reduces the mobility of ion, and thus decrease current efficiency [36].

Beginning as early as 1875 [47], prior chloride experiments [48]–[50] resulted in electrode contamination of the electrowon metal due to poor choice of electrodes, electrolyte, and cell materials. Later experiments used molybdenum and tungsten as cathodes to reduce electrode

contamination [51], [52]. Improvement of the purity of the salt, electrode type, and presence of a non-oxidizing environment, influenced high current efficiencies [53]–[55].

On a commercial scale, cells consisted of a bath made from iron or graphite or a refractory steel lined vessel [36] [43], [52], [56]. Cathode material was either the bath surface or iron. Anode material was graphite rods, or a graphite block placed as the bottom of the cell. With a typical graphite anode as shown in the reactions below, CO_2 is liberated when the MgO reacts with the graphite [57] and the REEs (Nd) as follows.

$$MgO + NdCl_3 \rightarrow NdOCl + MgCl \qquad [1.3]$$

$$2MgO + C \rightarrow 2Mg + CO_2 \qquad [1.4]$$

Common electrolytes comprise of $ReCl_3$ and NaCl, KCl or $CaCl_2$, and a purity of more than 99 % REMs is recovered [52]. As a result of the disadvantages with chloride salt chemistry, REE molten salt technology was later developed around fluoride based salts [58]–[60].

The increase in efficiency of fluoride cells over their chloride counterparts stem from the fact that experiments were conducted using purer starting materials in an inert environment. However, when there is a failure of REE metal product to coalesce effectively, loss of current efficiency can occur [61]. Improving current efficiency involves improving cell design (more corrosive resistant materials), prevention of product contamination, incorporation of cathode protection, selection of appropriate temperature, and use of better electrolyte composition.

First reported in 1907, earlier fluoride experiments comprised of the electrolysis of an REO_2 with REF_3, NaF or KF at lower temperature, which yielded products of either Na or K [62], [36].

During fluoride molten salt electrolysis, the oxides of REEs are dissolved in fluoride salts as seen in Figure 1.3. During dissolution, the REE oxides dissociate to form cations of REE and oxygen ions. When a potential is applied to the electrolytic cell, the REEs are reduced at the cathode as metals and the oxygen reacts with the graphite anode to form CO_2 or CO [35], [63]. The following reactions govern the electrolysis of REE molten salt:

Reduction = Cathode Reaction: $REE^{3+} + 3e^- = REE$ [1.5]

Oxidation = Anode Reaction: $2O_2 - 4e^- = O_2(g)$ [1.6]

Redox Reaction: $REE_2O_3 + C = 2REE + CO_2 + CO$ [1.7]

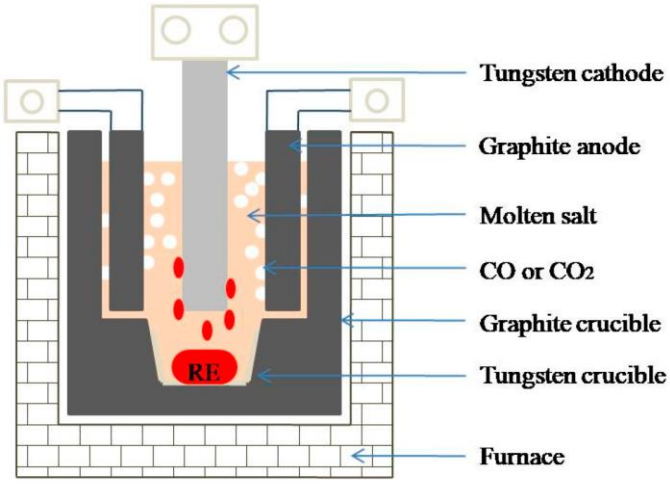

Figure 1.3. Schematic for molten salt electrolysis taken from Liu et al [35].S

Gray achieved the separation of Ce with high purity graphite as anode and molybdenum as cathode [64]. An electrolyte composition of CeO_2 combined with 61 wt% CeF_3 - 27 wt% LiF- 12 wt% BaF_2 was employed and yields of up to 77% for Ce, and purity of 99.7 to 99.8 % were obtained. Extraction of REEs such as Yttrium requires relatively high temperature for better yield and purity, making it a less attractive process [36]. Furthermore, high temperature stresses the cell and increases degradation of cell components [36].

Specific to Nd which is the most REE produced of all the REEs [65], during electrolysis, the oxide of Nd is mixed into the fluoride based molten salt NdF_3-LiF at 1050 °C. The electrolyte comprises of 85% NdF_3 and 15% LiF. During electrolysis, Nd^{3+} ions form complexes with the F^- ions to form $[NdF_6]^{3-}$ [66], [67]. The complex reacts with the tungsten electrode which is strategically placed at the center of the cell, and Nd is reduced to metal. This allows the dripping Nd metal to fall into a molybdenum crucible and later taken out by scooping [63] as seen in Figure 1.4 and this follows the reactions [67]:

Dissolution of Neodymium oxide:

$$Nd_2O_3 + [NdF_6]^{3-} + 9F^- = 3[NdOF_5]^{4-} \qquad [1.8]$$

Anodic Reaction:

$$3[NdOF_5]^{4-} - 6e^- = 1.5O_2 + 3\,Nd^{3+} + 15F^- \qquad [1.9]$$

Cathodic Reaction:

$$2[NdF_6]^{3-} + 6e^- = 2Nd(s) + 12\,F^- \qquad [1.10]$$

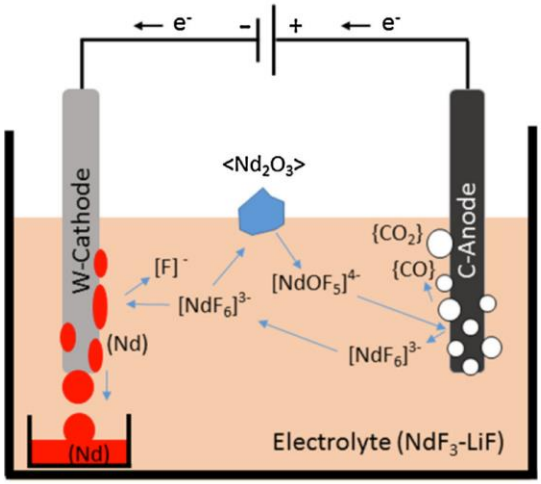

Figure 1.4. Reaction mechanism for Nd oxide during electrolysis. Image take from Vogel et al. [63]

Electrowinning of REEs is a proven method and continue to be effective in extracting REEs for the manufacture of magnets, alloys and other efficiency devices to enhance technological advancement. However, the scalability, high energy consumption, and the use of very harsh chemical have sparked interest in alternate research involving less chemicals and a lesser energy demand.

Metallothermic Reduction and Comproportionation

Suitable for the preparation of heavy REEs, such as Gd, Tb, and Y [35], metallothermic reduction (MR) involves the use of reactive metals such as Na, Li, Al, K, Ca, and Fe, to form halides, sulfides and oxides through reduction [27], [68]–[73]. A typical reaction for MR follows:

$$AX + B \rightarrow A + BX \qquad [1.11]$$

where AX or BX represents oxides, halides, or other compounds, B represents reactive metals, and A is a more electronegative metal. Figure 1.5 is a typical MR cell for the production of tantalum powder.

The commonest metallothermic reduction processes involve (1) reducing REE fluorides with calcium (Ca) metal and (2) reducing REE oxides with calcium hydroxide [28]. An advantage to this process is the > 90% yield is that is achieved. For REEs such as Sm, Eu, Yb, and Tm which have higher vapor pressure, La or Ce are employed as reductants [35] similar to the equation below:

$$2La + RE_2O_3 = 2RE \uparrow + La_2O_3 \qquad [1.12]$$

Furthermore, for REEs Y, Gd, Tb, Dy, Ho, Er, and Lu; Ca is employed as the reductant as follows:

$$2Ca + 2ReF_3 = 2RE + CaF_2 \qquad [1.13]$$

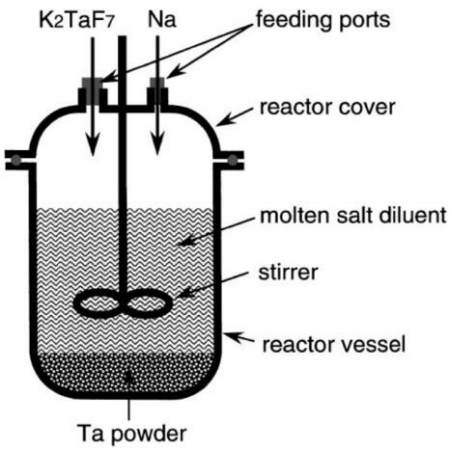

Figure 1.5 Schematic of industrial reactor for tantalum production [29].

In a patent on metallothermic reduction of REEs, Sharma [28] proposes an effective way to separate REEs up to >90 % using Na and Ca as reductants at lower temperatures while stirring. After the reaction is complete, components of the salt separate into layers and REEs can be solidified before separating or drained from the bottom. The equation below governs the reaction used by Sharma:

$$xRECl_n + yM \rightarrow xRE + yMCl \qquad [1.14]$$

Other research has been done in this area as a means of reducing REEs [30]–[33]. Advantages of the MR process includes the ability to breakdown strong chemical bonds at low temperatures, the ability to select a wide range of reductants, and decreased issues with impurities [27]. As a disadvantage, compound mixtures are produced rather than the formation of pure phases leading to the exploration of the comproportionation process.

Comproportionation is also effectively used to reduce REEs such as La, Ce, Pr, and Nd. This involves the use of crucibles laced with MgO and heated to approximately 1100 °C [21]. During the heating process, the REE chlorides vaporize while reacting with the MgO. For some REEs such as Sm, Eu, and Yb, metallothermic reduction is not an effective process because they are only reduced to their divalent states [21] [74]. Comproportionation is especially useful when phase relationships are known and involves the reduction of a REE chloride with a similar REE metal such as the following equations [21]:

$$GdCl_3 + Gd = Gd_2Cl_3 \qquad [1.15]$$

or

$$3CsCl + 2SmCl_3 + Sm = 3CsSmCl_3 \qquad [1.16]$$

Furthermore, Uda et al [75] demonstrated the separation of Pr-Nd and Nd-Sm using the method of comproportionation. They calculated a separation factor for the Nd-Sm mixture to be approximately 570 in contrast to the conventional solvent extraction method of 9.6. In the Pr-Nd system, the separation was less efficient due to the potential difference between $NdCl_2$ and $NdCl_3$. However, a separation factor of 8.1 was achieved in contrast to the conventional solvent method of 1.3 to 1.7. They concluded that with this technique, not only can the REEs addressed here be separated but also other elements as well.

For high melting point REEs such as Gd to La, and Sc, reduction occurs at temperatures of 1500 – 1600 C between their fluorides and Ca in a tantalum crucible [21]. The use of iodine in some cases allows for temperature reduction, and reactivity is a clean flowing slag which can be easily separated [21]. La allows for the separation of Sm, Eu, and Yb at 1000 °C 1300 C under a vacuum. The vapors of the REEs are then distilled by condensing on coolers [21]. This process is great for separating REEs from metals which are not volatile under these conditions [21].

High temperature reactions are also a disadvantage for comproportionation reactions, as well as the need for a non-oxidizing atmosphere [34] [28] . However, using low melting and highly electropositive metals, as well as alkali and alkaline earth metals reduces the temperature [34]. One disadvantage of using low temperature is that pure products are not produced because of the lack of high lattice energy of alkali metals halides as shown in the equations below [34]:

$$SmCl_3 + Na = SmCl_2 + NaCl$$ – high melting point [1.17]

$$Cs + SmCl_3 = CsSmCl_3$$ - low melting point [1.18]

Ion Exchange Extraction

Cation exchange resins enable the separation of REEs through the ion exchange process. During the ion exchange process a cation resin is contacted with the pregnant rich leachate or pulp [76] as seen in Figure 1.6. The presence of resins drive the leaching reaction towards equilibrium and thereby helps in the capture of elements of interest. However, without modification to the acid leachate, present REEs are trapped by the resin due absence of preferential selectivity [21]. The electron affinity of REEs is crucial to REE separation and can be employed with the use of complexing agents to enhance individual or collective separation[77]. This is achieved by passing a buffer solution containing negative ions through the separating column [21]. The buffer solution forms complexes with the REEs and creates competition for REE ions between the aqueous phase and resin phase. As equilibrium is achieved, exchange between complexing ions and resin occur [21]. More stable REEs move faster down the column as a result of difference in stability constants between REEs [21].

Different complexing agents such as citric acid, lactate, and ethylene diamine tetra acetic acid (EDTA) are used as effluents by varying pH using ammonium hydroxide [21]. For practical purposes large surface areas of organic and inorganic solvents are required [78], [79]. Various ion exchange sorption resins for REE such as strong acid resins [80]–[84], carboxylic resins [85]–[87], phosphorus containing resins [88]–[92], and polyfunctional resins [93]–[97] have been explored for the separation of REEs.

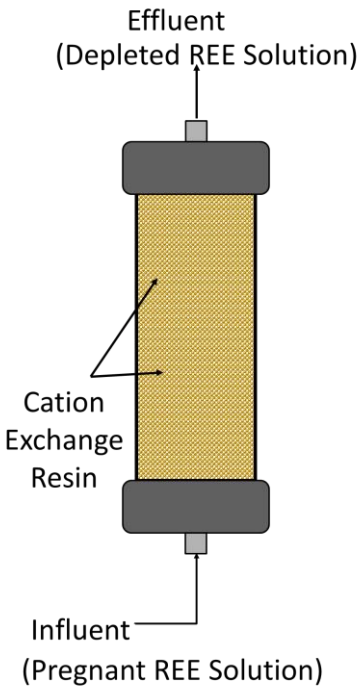

Figure 1.6. Basic ion exchange process.

The presence of resins drive the leaching reaction towards equilibrium and thereby helps in the capture of elements of interest. However, without modification to the acid leachate, present REEs are trapped by the resin due absence of preferential selectivity [21]. The electron affinity of REEs is crucial to REE separation and can be employed with the use of complexing agents to enhance individual or collective separation[77]. This is achieved by passing a buffer solution containing negative ions through the separating column [21]. The buffer solution forms complexes with the REEs and creates competition for REE ions between the aqueous phase and resin phase. As equilibrium is achieved, exchange between complexing ions and resin occur [21]. More stable REEs move faster down the column as a result of difference in stability constants between REEs [21].
Different complexing agents such as citric acid, lactate, and ethylene diamine tetra acetic acid (EDTA) are used as effluents by varying pH using ammonium hydroxide [21]. For practical purposes large surface areas of organic and inorganic solvents are required [78], [79]. Various ion exchange

sorption resins for REE such as strong acid resins [80]–[84], carboxylic resins [85]–[87], phosphorus containing resins [88]–[92], and polyfunctional resins [93]–[97] have been explored for the separation of REEs.

Rychkov et al. investigated the use of polystyrenesulfonic cation exchange resins (divinylbenzene (DVB), Purolite C-100, Purolite Corporation)) to study the exchange behavior between REEs ferric and aluminum ions [84]. They observed that within a pH range of 1.5 - 2.0 concentration of REE from ion exchange solution was achieved in resins with more than 8% DVB. Furthermore, Shokobayev and Dauletbakov studied the recovery of REEs from barren uranium solution using eluents of nitric and ammonium nitrate solutions [83]. The cation resins used were 001 x 7, 005 x8, and D72. It was observed that D72 yielded better adsorption and desorption results for REEs, and that ammonium nitrate is much more efficient than nitric acid. Arnold and Hing, also studied the selectivity of carboxylic ion exchange resins Amberlite IRC 50, Amberlite XE 89, and Zeo-Karb 225 2% divinyl-benzene in the presence of praseodymium and neodymium chloride solution [87]. They concluded that the selectivity of lanthanides increased as the ionic radius of the lanthanides decreased, the opposite for sulphonic resins. They also observed that the interaction of lanthanide ions with the carboxylic resins is stronger than sulphonic resins. Bogochek and Surowiec, modified chloromethylated St DVB polymers with dialkyl phostipes [88]. This modification replaced the chlorine atom in the -CH_2CL group with a phosphorous containing group, yielding cation resins and sorbents with promising properties. In a much earlier study of phosphonic group resins, Bogochek and Surowiec, observed that phosphonic based resins exhibited higher separation factors of alkali, alkali earth metals and transition metals than the sulfonic and carboxylic group resins [89]. Furthermore, they observed that among the phosphonic group of cation resins, such as the nuclei-bound phosphonic group (P-M), the methylene-bound phosphonic group (PP-M), and the aliphatic chain-bound phosphonic group, the P-M showed better separation properties with the highest affinity shown by trivalent ions. Paga et al. compared three chelating resins sulfonic/phosphonic (SP), aminophosphonic (AP) or iminodiacetic (IDA) acid functional group to analyze the selectivity of the resins towards REEs such as La, Sm, and Ho, to more common impurities such as Al, Fe and Th [96]. They observed that for SP and AP resins the tolerance for selectivity towards REE in higher concentration of acid was greater than IDA. However, at higher concertation of Na and Ca, IDA showed superiority in REE adsorption.

Ion exchange for the separation of REEs have been studied vastly and exhibit several advantages. As in the case of polymers, no loss of extractant occurs due to covalent bonding between ligand and polymer[97]. Furthermore regeneration and reuse of polymers, and the absence of organic solvents

make this process environmentally friendly [97]–[100]. However, a downside to the ion exchange extraction process is the possibility of loss of chelant due to solubility. Furthermore, there exists a slow rate of equilibration by some polymer supported reagents [97].

Solvent Extraction

Solvent extraction, commonly known as liquid-liquid extraction [101]–[103] employs the use of an organic solution with an extractant to separate individual REEs from leachates [104], [105]. Extraction, scrubbing or washing, and stripping are the three basic steps of solvent extraction [103], [105]. Figure 1.7 is a schematic representation of the process of solvent extraction with the use of two immiscible liquids namely an aqueous phase and an organic phase.

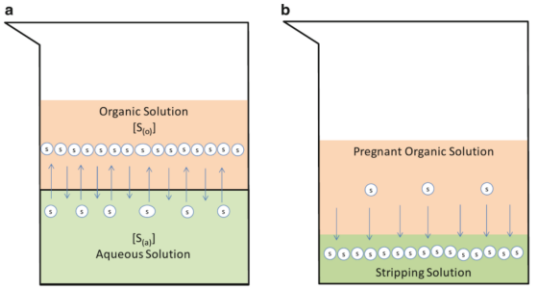

Figure 1.7 Basic schematic representing solvent extraction (a) extraction and (b) Stripping [103]

Prior to the solvent extraction process, REEs are beneficiated and concentrated from ore by either gravitation, floatation, or magnetic processes. Leaching of REEs is then employed using HNO_3, HCl, or H_2SO_4 [104]. Following the leaching process, the solvent extract process then occurs when REEs are contacted with common extractants such as DZEHPA, HEHEHP, VERSATIC 10, TBP and Aliquat 336 [104]. Whereas the aqueous phase contains desirable metals, the organic phase contains an extractant and modifier in a diluent or carrier [103]. The diluent or carrier is usually a product of crude oil fractionation, containing variable compositions of hydrocarbon structures. The main role of the extractant in the diluent or carrier is to transfer metal ions from the aqueous solution to the organic solution via the formation of metal organic complexes [103]. The modifier is added to improve phase disengagement, and metal solubility in the organic phase[103] prior to scrubbing.

During scrubbing, the impregnated organic solution containing the desired material is contacted with a dilute acid, a base solution, or water to remove the undesirable solutes. However, some desired metals are trapped in the scrubbing solution. As a result, the scrubbing solution is channeled back to be recycled with the aqueous feed, while the remaining impregnated solution is stripped [103]. Stripping follows the same principles as extraction. From Figure 1.7 b, the pregnant organic solution is brought into contact with the stripping solution, usually concentrated acid, salt or alkaline. This is

used to pull rare earth metals from the organic solution into the strip solution [103]. Commercially, solvent extraction has taken over ion exchange extraction due to the capability of handling larger volumes of dilute pregnant solution [104], [106]–[108].

Two parameters used to describe and tune the effectiveness of solvent extraction is the distribution ratio coefficient (D_m) and the separation factor (β) [103]–[105]. D_m is the ratio of the molar concentration $[\bar{M}]$ of the metal ion (M) in the organic phase, to the concentration of the metal ion in the aqueous phase [M] show as

$$D_M = \frac{[\bar{M}]}{[M]} \qquad [1.19]$$

Similarly, the separation factor between two metals can be established as the ratio of the distribution ratio of two metals as follows:

$$\beta_{M_1/M_2} = \frac{D_{M_1}}{D_{M_2}} \qquad [1.20]$$

These two parameters are deeply affected by the type of extractant used. Among the many extractants employed for the use of REEs extraction are cation exchangers [109]–[111], chelating extractants [112], [113], solvation extractants [114]–[116] and anion extractants [117]–[119]. For the purpose of the research being proposed, this section would only cover cation exchangers.

Cation Exchangers

The equation governing the interaction of REEs in the organic phase in relation to cation exchange is

$$Ln^{3+} + 3\overline{H_2A_2} = \overline{Ln(HA_2)_3} + 3H^+ \qquad [1.21]$$

where H_2A_2 is the dimeric form of the organic acid, A is the anion in the organic acid and the overscored species are the species present in the organic liquid [104], [120].This suggests that as the pH of the aqueous phase is increased, cation exchange is promoted. The two common acids employed during cation exchange extraction are carboxylic acids and organophosphorus acids.

Banerjee et al. [121] investigated the extraction of REEs from coal fly ash using the carboxylic acid, tartaric acid, citric acid, lactic acid, malonic acid and succinic acid. They observed that tartaric acid showed the highest leaching efficiency, with succinic acids being the lowest for both LREEs and HREEs. Furthermore, they suggested that the pKa value and the number of hydroxyl and carboxylic groups influence leaching efficiency. The lower the pKa value and presence of hydroxyl and carbolic groups in the molecular structure, the better the leaching efficiency. Zhao et al.[122] also employed the use of HEEAMP to separate LREEs from HREEs. Furthermore Shimoho et al. [123] synthesized

a carboxylic extractant (DODGAA) with CHON ligands that performed comparable well to organophosphorus compounds. Shimoho et al. [123] further observed higher selectivity with HREEs. Also, Abreu and Morais [124] investigated three organophosphorus extractants, DEPHA, IONQUEST801 and CYANEX272 in hydrochloric and sulfuric acid aqueous solutions. They observed that the extraction efficiency of DEPHA and IONQUEST were better in hydrochloric media than in the sulfuric acid media. Sato [125] further studied DEHPA and EHEHPA for the separation of REEs from their chlorides in hydrochloric or nitric acid media. Sato [125] observed that DEHPA had a higher selectivity towards lighter REEs than EHEHPA. However, for the extraction of HREEs, EHEHPA is more selective. Furthermore, Banda et al [126], employed the used of Cyanex 272 mixed with other extractants to study the separation of Pr, Na and La. It was observed that the efficiency of extraction decreases with increasing concentration of extractants such as TBP and TOPO. However, when mixed with Cyanex 301 a cation extractant, the extraction of efficiency of La increase whiles that of Pr and Nd remained fairly stable compared to Cyanex 272 as the only extractant. The push for CHON extractants over organophosphorus extraction is the green nature of CHON extraction. Unlike organophosphorus extractants, CHON extractants can be incinerated completely to gaseous products, thus results in waste reduction [123]. Furthermore, finite solubility and phase disengagement of aqueous associated with extractants, modifiers and solvents are significant problems when it comes to solvent extraction [97]. Also, large volumes of organic extractants are needed for very dilute metal ion solutions.

Low Temperature Electrolysis in Aqueous Media for REEs Separation

Studies of chemical processes involving the use of amalgam formation (employing mercury (Hg)) for the separation of REEs were prevalent during the 1940-60s, but was left dormant for the past half century [127]–[131].

The advantages of using liquid electrodes such as Hg over solid electrodes is the high hydrogen evolution over potential, which offers a wider range potential to facilitate amalgam formation. For example, the potential range of platinum is +1 to - 0.3 (vs SCE). However, when amalgamated with mercury, the range expanded from -0.3 V to -2.1 V (vs SCE) [130] [132]. Other advantages of the amalgam electrode is the renewability of the electrode surface without interfering with previous measurements, prevention of interference from contaminates, and absence of cleaning or refreshing electrode [130]. Electron transfer and ion transfer have been speculated to govern the formation of amalgam, and act as the rate determining step during the process [132].

The important factors affecting the electrolytic separation of REEs include valency and atomic numbers. Some REEs are divalent, and others are trivalent. Divalent REEs are easily separable such

as Eu, Sm, and Yb. However, trivalent REEs are much more difficult to separate using electrolysis at the amalgam cathodes due to their critical and electrochemical differences being less pronounced [127]. Electrolysis is difficult to achieve when a REE is complexed in an aqueous solution. However, when REEs are in mixtures the lightest will be easily electrolyzed due to increase in complex stability of ions as atomic number increases [128].

Various extractants are used in conjunction with Hg to extract REEs from aqueous solution. The most wide used extractants are acetates, citrates and tartrates [133]. Furthermore, at very negative potentials, hydroxides of REEs are precipitated in aqueous solution. Past researchers [133], [134], [135] suggest the use of weak alkaline organic solutions. This prevents the hydroxide precipitation of REEs salts on the amalgam. Also, Kolesov and Pankratova [133] give an in-depth review on the separation of rare earth elements by electrolysis at a mercury cathode.

Intercalation of Metal Cations

The atomic lattices of two dimensional crystals are held together in place by covalent bonding and weak van der Waal out of plane interactions due to an interlayer gap[136], [137] as seen in Figure 1.8. Likewise, intercalation is the chemical or electrochemical reversible insertion of foreign molecules or atoms in between the planes of host materials; usually solids, without significantly altering the physical structure of the host solid [138]–[141]. This creates an new material with unique physical and chemical properties [141] Commons host material includes graphite, hexagonal boron nitride, MXenes, and dichalcogenides of transition metals [139].

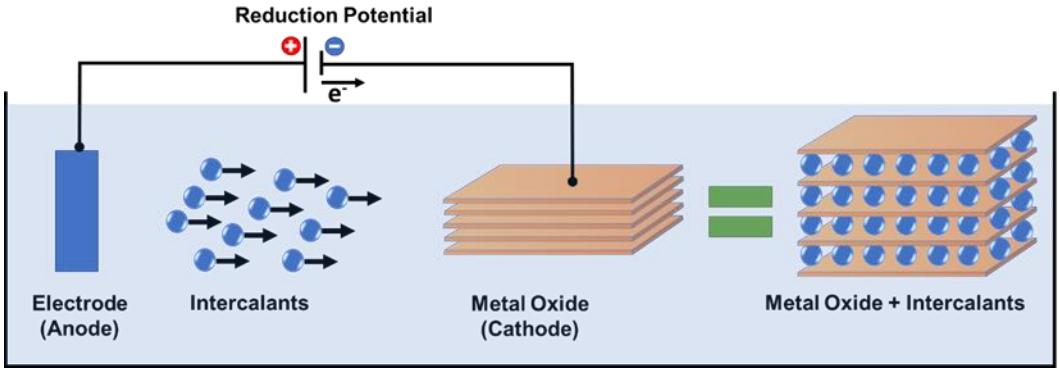

Figure 1.8 The Electrochemical intercalation process.

The most common example of intercalation is the intercalation of Li ions into graphite which led to the inventing of the Li ion battery during the early 1970s [142]–[144]. During discharging (intercalation or loading) lithium ions are inserted into the van der Waal gaps of the layered graphite) and removed during charging (de-intercalation or unloading) [144]. Valency is crucial to storage

capacity with regards to interaction. For example, commonly intercalated ions such as Li^+ and Na^+ which are monovalent in nature involve one ion transfer during chare or discharge. However, when replaced with a trivalent ion such as Al^{3+}, three-ion transfer takes place during charge or discharge. Suggesting that for the same number of ions for Li^+ or Na^+, Al^{3+} provides a larger storage capacity [145]–[147].

Various procedures such as wet chemical intercalation [139], [144] [148]–[152], gas-phase intercalation [153]–[157], and electrochemical intercalation allow for the creation of unique materials [139], [144] [158]–[164]. These procedures produce material with characteristic such as superconductivity, optical transmittance, catalytic activity, and energy storage capabilities [38], [165]–[168]. For example, when Li^+ ions are intercalated into MoS_2, the intercalated material has enhanced optical transmittance and electrical conductivity [167]. Furthermore, the intercalation enables the exfoliation of bulk host materials, leading to the production of nano sheet materials, of which have a wide range of application [158], [169]–[171]. For the purpose of this research, electrochemical intercalation will be the area of focus.

Electrochemical Intercalation

Electrochemical intercalation has gained keened interest among researchers due to its versatility and ability to precisely control intercalation stages [169]. During intercalation, the positively charged or negatively charged ions are driven into the van der Waal gaps of the 2D material by an external potential as seen in Figure 1.8. This creates materials with unique capabilities, stoichiometry, and characteristics.

Depending on the type of ions intercalated, the host material can assume the role of cathode (intercalation of positive ions) or anode (intercalation of negative ions). Concurrently, a cathodic potential (more negative potential) will drive positive ions into the host material, and an anodic potential (more positive potential) would drive negative ions into the host material. During electrochemical intercalation. The stability of the host material under the influence of the external potential is key for a successful intercalation [139].

Many research have focused on the anodic intercalation of various anions into 2D materials [158]–[162], and have focus vastly on the exfoliation of 2D material. Murphy and Hull achieved the intercalation of hydrogen in 2H-TaS_2, 2H-$NbSe_2$, 2H-NbS_2 by reacting with H_2SO_4 at a current density of 40 mA [163], [164]. However, they noted in some of their experiments that the exfoliation of some of their sample was due to the intercalation of excess water molecules [164]. For the purpose of the research being undertaken, we hereby focus the rest of this section on the cathodic intercalation

of positively charged ions with hopes of implementing this technology with the intercalation of trivalent REEs such as Nd into metal oxides.

Cathodic Intercalation of Positively Charges Ions

Metal oxide electrodes have sparked interest among researchers due to their promising characteristics. Compared to metal electrodes, the presence of redox couples permits the enhancement of reaction rates as well as decrease the adsorption of hydrogen or hinder the formation of hydrogen on the metal oxide electrode surface [172] [173].

Cathodic intercalation of positively charge ions involves the use of a reduction potential to move positively ions from the electrolyte to the van der Waal gaps of the host material. This process minimizes the damage of oxidation caused by the 2D crystals and prevents the formation of unwanted chemical complexes [174]. Common examples are the intercalation of cations such as Li [175]–[179], Na [180]–[184], K [185]–[188]and Zn [189]–[191] into metal oxides such as graphite, MnO_2 [191], [192] and MoS_2 [167], [190].

Zhang et al. [191] demonstrated the rechargeability of a zinc-manganese dioxide battery using aqueous zinc triflate as electrolyte $Mn(CF_3SO_3)_2$, MnO_2 as the cathode, Zn as anode and $Mn(CF_3SO_3)_2$ as additive. They observe a stark increase in charge and discharge during the cycling of the battery. Furthermore, they attributed the stability of the β-MnO_2 to the Mn additive which suppresses the dissolution of Mn^{3+} to Mn^{2+} through disproportionation. The successful intercalation of Zn, and the increase in columbic efficiency compared to other conventional cation batteries like Na^+, K^+, and Li^+, can be attributed to the addition of the Mn additive of 0.1 M, and the slight acidity of the electrolyte.

Investigating a different cation intercalant, Yadav et al. [192] studied the intercalation of Cu^{2+} into Bi-δ-MnO_2 and found that the stability of the Bi-δ-MnO_2 structure was enhanced by the presence of Cu^{2+}. Furthermore, in a paper written by Pang et al. [193] . The mechanism governing the intercalation of MnO_2 was suggested as follows:

$$MnO_2 + H^+ + e^- \leftrightarrow MnOOH \qquad [1.22]$$

or

$$MnO_2 + C^+ + e^- \leftrightarrow MnOOC \qquad [1.23]$$

where C represented cation such as Na^+ or K^+ or Li^+ or Nd^{3+}. In another paper by Toupin et al. [194], the thickness and characteristics of MnO_2 was investigated. They concluded that due the agglomeration of MnO_2 when deposited, only a small thickness of the MnO_2 takes part in the

electrochemical reaction. Consequently, they observed that thin films performed better than thick films [194].

Ren at al. [187] studied the intercalation of K^+ ions into MoS_2 and observed successful intercalation and deintercalation. This was corroborated by the formation of a K_xMoS_2 phase. They observed that when x was greater than 0.4, the intercalated material was not stable, causing reduction of MoS_2 to Mo and K_xS species.

The advantages of electrochemical intercalation lie in the fact that:

1. There is a wide variety of intercalants to choose from
2. Intercalation stages and levels can be precisely controlled, and the number of intercalants can be determined
3. Ability of in-situ monitoring
4. Reversible intercalation process and can be used for photoelectric applications [195], [196]

However, the disadvantages of electrochemical intercalation are:

1. Inability to work with insulated materials and this remains an issue
2. Intercalants which require a potential outside their potential will first be oxidized or reduces before they can be intercalated

The procedure to carry out the steps for the successful immobilization of REEs in metal oxides is now addressed.

Summary of Current REE Separation Technologies

Table 1.3 Limitations of current separation and reduction processes.

Separation Process	**Pros**	**Limitations**
Liquid-Liquid Extraction eg. (Solvent extraction)	• Selective organic extractants • High percentage recovery	• Solvent degradation • Loss of efficiency due to degradation of extractants • Large volumes of extractants and reagents • Multiple Stages of separation
Ion Exchange	• No loss of extractant occurs due to covalent bonding that occurs between ligand and polymer. • Regeneration and reuse of polymers • Absence of organic solvents make this process environmentally friendly	• Loss of chelant due to solubility. • Slow rate of equilibration by some polymer supported reagents
Metallothermic reduction/ Comproportionating	• Ease if separation of REE due to formation of layers • Useful for known phase relationships	• Very high operating temperatures • production of toxic gasses • Harsh chemicals • Presence of an oxidizing environment
Electrowinning	• Separation of REEs using applied potential • Dynamic selectivity of electrodes to enhance extraction purity	• Very high operating temperatures • production of toxic gasses • Cell degradation • Loss of current efficiency
Liquid Alloy Oxide Formation	• Recyclable surface of electrode • Reduced number of steps • Less toxicity	• Toxicity of mercury* • Potential less stability

Table 1.3 continued

	• Reduction in capital cost • Dynamic • Adaptable to existing processes • Low temperature	
Metal oxide intercalation	• Alternative anode reaction • Low temperature • Less chemically exhausting • Presumably purer REEs • Wide variety of intercalants to choose from • Precise control and determination of Intercalation stages and levels • Ability of in-situ monitoring • Reversible intercalation	• Potentially instable in ionic liquids • Bulky electrode • Inability to work with insulated materials • Oxidation of reduction of intercalants which require a potential outside their potential will

* Mercury was used in past work, this proposal seeks to replace

Identified gaps and opportunities

1. Though the technologies described above have proven to be efficient in the extraction of REEs, some of them involve large quantities of hazardous, sometimes harmful exhaust gases and high temperature operation – leading to intense energy exhaustion.
2. Anode materials and electrolytes employed in these processes also degrade over time.
3. Due to the cons of the technologies described, there is opportunity in creating a technology or sets of technology which involves less hazardous chemicals and can be functional and efficient at low temperature (<40 °C).
4. Since the ban of mercury (Hg), there haven't been studies demonstrating the capture of REEs using a similar liquid cathode material. Low temperature immobilization of REE using alternative cathode material such as Ga might be possible. Ga is a suggested material due to its similar characteristic to Hg.
5. Intercalation which is an already developed process for the capture of certain cation materials and for battery applications, has not been explored for REEs. Intercalation can be a very promising route for the capture of REE cations into the atomic lattice of commonly used material such as Mn_2O, and graphitic materials.

Chapter 2: Electrochemistry of Praseodymium in Aqueous Solution Using a Liquid Gallium Cathode.

"Electrochemistry of Praseodymium in Aqueous Solution Using a Liquid Gallium Cathode." ***Journal of The Electrochemical Society*** **169.6 (2022): 063519.**

Abstract

The electrochemistry of liquid Ga electrodes in aqueous media was examined in the presence of praseodymium acetate (PrOAc) as an alternate path for low temperature reduction of rare earth elements (REE). This study investigated the aqueous electrochemistry of Ga with and without REEs (Pr). Cyclic voltammetry experiments showed that in the presence of PrOAc, an order of magnitude increase in cathodic current was observed for the Ga electrode, compared to that in the absence of Pr. Decrease in the reduction current with the increase of scan rate, with and without Pr, suggests catalytic reactions following electron transfer, which was attributed to the Ga_2O disproportionation reaction. Chronoamperometric experiments performed in Pr containing solutions formed a precipitate. Over 50% of the Pr ions from the aqueous electrolyte were immobilized in the precipitate; a solid Ga-rich phase. Formation of this precipitate was only possible when Ga oxidation was induced. This condition was achieved by circulation of liquid Ga from the pool via external pump and returned dropwise to the liquid Ga pool. When the collected precipitate was leached in dilute HCl, Pr was unloadd with H_2 evolved as a byproduct, and Ga returned to its initial liquid metallic state. These preliminary results show encouraging new routes that could be applied for the recovery of diluted REE leachates, such as those obtained from magnets, coal fly ash, and ores.

Introduction

The electrochemical reduction of reactive metals, such as rare earth elements (REEs) is hindered in aqueous media due to extremely negative reduction potentials. This setback occurs due to the limited electrochemical window of water favoring the evolution of hydrogen over metal reduction [197]. However, through alloy formation, the chlor-alkali industry has shown that reactive metals such as sodium can be reduced to the metallic state in aqueous media [198], [199]. Hence, the use of amalgam formation (employing mercury) for the processing of REEs was prevalent during the 1940-60s [128]–[131], [200].

Previously, mercury (Hg) has been employed as electrode material for REE alloy formation, offering a high hydrogen evolution overpotential and an increase in the cathodic potential operating range [130], [201]. However, the toxicity of Hg makes its handling and disposal hazardous, expensive, and

highly regulated [202], [203]. These concerns suggest the need of a material substitute with similar characteristics as Hg, but of a nontoxic nature.

Ga and Ga alloys are possible substitutes for Hg electrodes, due to low melting points. Like Hg, Ga possesses a high hydrogen overpotential without compromising electrochemical behavior and offers surface renewability. Ga is non-toxic and has a lower vapor pressure than Hg. However, it also features more negative reduction potential than Hg [203], which makes Ga and its associated oxide formation less stable than Hg.

The electrochemical nature and complexity of Ga has garnered interest among researchers due to the characteristic of easily forming surface oxide layers [204]. Formation of the oxide layer on liquid Ga occurs spontaneously in aqueous solution [205]. In aqueous media, Ga exists as various species with β-Ga_2O_3) as its most stable phase. Trivalent speciation for Ga in aqueous solution is pH dependent and may exist as Ga^{3+}, $Ga(OH)^{2+}$, GaO^{+}, GaO_2^{-}, $HGaO_3^{2-}$, or GaO_3^{3-} [206]. Flamini *et al.* observed that at low current densities, Ga(III) can be reduced to Ga(I) [207]. Recently, Monnens *et al.* showed evidence of the formation of Ga(I) as an intermediate in the reduction of Ga(III) to Ga metal [208]. The presence of Ga(I) in the form of Ga_2O was also reported by Hong et al. [209]. Other studies have reported that Ga_2O undergoes a disproportionation reaction, to form Ga metal and Ga(III) due to its instability in aqueous environments [209], [210].

Furthermore, the ability of Ga to dissolve a host of other metals creates a pathway to produce metal and metal oxides [210]–[212]. Mayyas et al. [213] observed that the application of a potential range to GaSn, GaIn and GaZn alloys led to the capture and unload of Sn, In and Zn. Other studies have also employed the use of Ga to induce mass transport of target elements by converting the effect of an electrical current into mechanical flow [214]–[217].

In this work, a deeper understanding of Ga electrochemistry in the presence of a REE specie was driven by interest in using Ga as a medium to reduce and capture REEs directly from aqueous media. This paper reports on the behavior of Ga in lithium acetate (LiOAc) solutions with and without Pr, where oxides play a role in the formation of products at the cathode. LiOAc was selected due to solubility of REEs at higher pH values.

Experimental

Electrochemical experiments

The working electrode was a liquid Ga (99.99%, Rotometals) pool (approximate surface area of 8.04 cm^2) with a Pt wire as current collector. The area of the Pt wire exposed to solution was coated with Teflon. Measurements were performed at 30 °C to maintain Ga as a liquid. The auxiliary electrode

was either Pt or IrO_2/titanium mesh for cyclic voltammetry (CV) and bulk electrolysis (BE), respectively. A dimensionally stable anode (DSA) coating was applied to both sides of the titanium mesh by brushing H_2IrO_3 diluted in isopropyl alcohol onto the exposed surfaces followed by heating at 550 °C for 2 h to form IrO_2. Potentials were measured and reported versus an Ag/AgCl (3 M NaCl) (BASi) reference electrode. Analytical grade lithium acetate (LiOAc) and praseodymium acetate (PrOAc) hydrate 99.9%, were used for electrolyte preparations in deionized water (DI) (>18 MΩ). Chronoamperometry and potentiodynamic experiments were performed using a BioLogic SP-50 potentiostat controlled by EC-Lab software. IR compensation was applied to CV curves. CV experiments were conducted in a single cell as shown in Figure 2.1a. Bulk electrolysis experiments were conducted in a H-cell depicted in Figure 2.1b. All experiments were conducted in an open atmosphere environment.

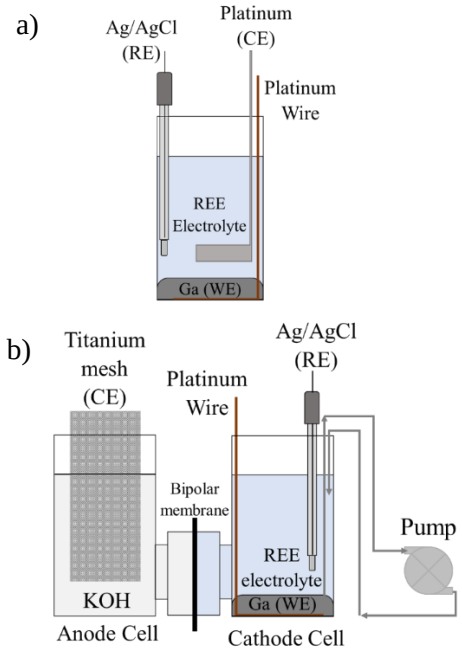

Figure 2.1 a) Single compartment setup for CV experiments, b) H-cell setup for bulk electrolysis experiments (BE). Lines with arrows represent the circulation of Ga.

Analysis and characterization methods

Following electrochemical tests in PrOAc electrolyte, the liquid Ga was separated from the electrolyte, washed with DI water, and stripped in 1 M HCl. For experiments involving formation of a gray precipitate as a product, the electrolyte was centrifuged, and vacuum filtered to recover the precipitate. For analysis, the precipitate was digested in a 3:1 HCl-HNO_3 or 1 M HCl. The elements Pr and Ga were measured using an iCAP Q inductively coupled plasma mass spectrometer (ICP-MS) from Thermo Scientific. Peak analysis, and calculation of charge for reduction and oxidation features

on CV plots was conducted using an EC-Lab V.11.33 by BioLogic Instruments. EC-Lab integration function was employed without background subtraction, for calculating the charge. SEM and EDS analysis were conducted in a JEOL JSM-6610LV and EDAX AMETEK Apollo X controlled by EDAX software, to study surface morphology, elemental composition, and elemental distribution. SEM and EDS samples were prepared by appropriately placing double sided carbon tape unto sample holders and dipping the opposite side of tape in the dried precipitate product. XRD analysis was conducted to determine the crystallinity of the gray precipitate using a PANalytical X-Pert Pro Diffraction System (Co Kα radiation, λ = 1.78897 Å). A complete description of ICP-MS and XRD analysis is presented in the supporting information file. Elemental analysis of the precipitate was obtained using a 836 Series Elemental Analyzer using inert gas fusion technique to measure overall oxygen content. The Raman spectra of the precipitate was collected using a Bruker SENTERRA II dispersive micro Raman spectrometer equipped with a confocal microscope (20x) from 50 to 3500 cm^{-1} at 4 cm^{-1} resolutions using an excitation wavelength of 532 nm (green laser). Laser power was set at 12 mW, while integration time was limited to 2 seconds and 30 scans were accumulated to improve signal-to-noise ratio. The homogenized powdered samples were first pelletized into circular disks, which were then used for the Raman spectroscopic data collection. The Raman data collected at different locations on the pellets of the samples did not show any noticeable change confirming the homogeneity of the samples.

Results and Discussion

Cyclic voltammetry of background electrolyte (0.15 M LiOAc)

The oxidation of Ga to Ga(III), in aqueous media, is thermodynamically favored given the pH of the electrolyte (~6.9) and the potential window (> -0.9 V), used in this work. This is corroborated by the Pourbaix diagram in Figure 2.2.

Furthermore, the formation of Ga(III) oxyhydroxide as suggested, is in agreement with the work done by Varadharaj and Rao [218]. Under these conditions, the Pourbaix diagram for gallium in water [206] suggests:

$$4Ga + 3O_2 + 2H_2O \rightleftharpoons 4GaOOH \qquad [2.1]$$

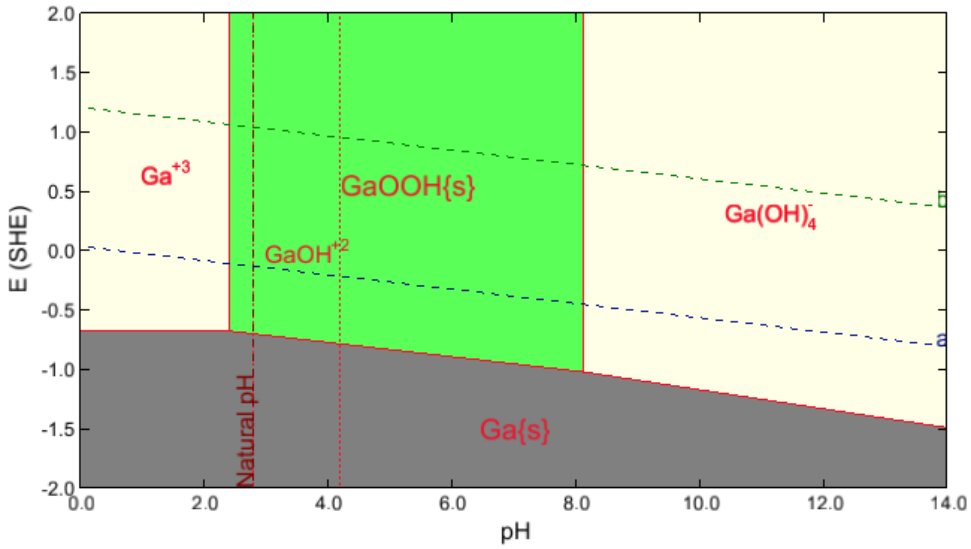

Figure 2.2. Pourbaix diagram for Ga at 30 °C in the presence of 0.15 M HOAc. The natural pH of a 0.15 M HOAc solution is shown by the vertical line. HCl and NaOH were used to vary pH below and above the natural pH.

0.15 M LiOAc background electrolyte was employed for the initial electrochemical studies of liquid Ga electrode. Figure 2.3 shows the current-potential profiles of liquid Ga electrode in the background electrolyte. During potential sweeps, the cathodic limit, $E_{c,}$ was maintained at -1.27 V while the anodic limit, E_a, was incrementally adjusted from -1 to 0.2 V. The selection of -1.27 V as the E_c prevented excessive hydrogen evolution. A reduction peak C_1 at approximately -1.17 V was observed during the first cycle, starting at an initial open circuit potential (OCP) above -0.85 V. However, C_1 decreases significantly in subsequent scans and eventually becomes nonexistent when E_a remains below -0.9 V as shown in Figure 2.3a. As the forward scan approached -1.17 V, the surface of the Ga pool changed from dull to a shiny appearance. This suggests the reduction of surface oxides [207], [212]. As the potential scan passed below -1.2 V the current increase can be attributed to the hydrogen evolution reaction (HER)[207]. Shortly after reversing the potential (Figure 2.3a), peak A^* is observed. Peak A^* can be attributed to reduction of adsorbed hydrogen (H_{ads}). This was verified by varying E_c while maintaining E_a at -1 V (Inset of Figure 2.3a). When E_c is positive of the HER region, A^* disappears. Tsvetanova et al. [219], offered a similar interpretation while studying the anodic dissolution of Ga in acidic aqueous media. Likewise, Varadharaj and Rao [218] also observed a similar phenomenon while studying Ga films in alkaline media.

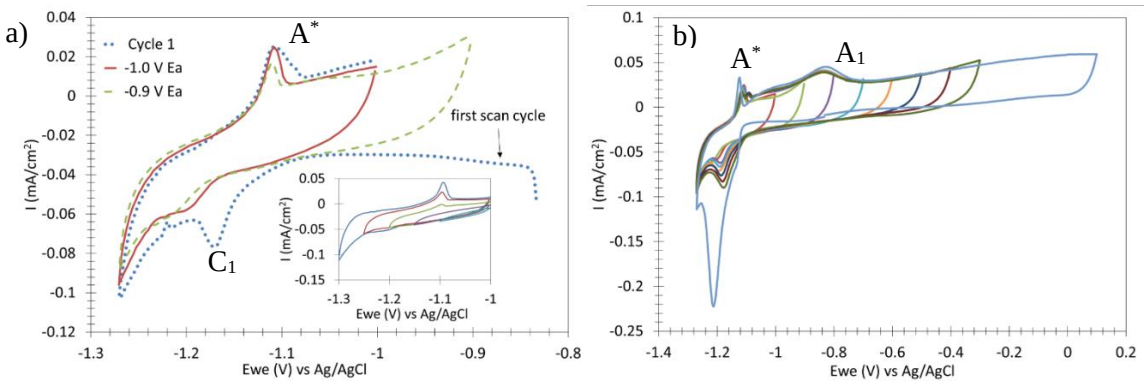

Figure 2.3 Window opening CV scans of Ga electrode at 10 mV/s in LiOAc (first cycle is blue dashed curve). a) CV scan cycles with cathodic switch potential held at -1.27 and varied from -1.0 V (red solid curve), to -0.9 V (green dash curve) with inset showing response while varying the lower switch potential, b) CV scan cycles where the anode switching potential is varied.

Note that with E_a below -0.9 V, no distinct oxidation peak is observed that can be correlated to C_1. The decrease in the reduction peak C_1 following the first cycle (E_a is below -0.9 V) suggests that C_1 is linked to reduction of the native oxide on Ga. This suggests that in this potential range Ga oxidation is nonexistent or kinetically slow.

Figure 2.3b shows that increasing E_a to values greater than -0.9 V introduces the broad oxidation wave A_1 (ca. -0.85 V), and the re-appearance of the reduction peak C_1 during the cathodic scan. As E_a increases more positive of -0.8 V, a clear increase in C_1 peak current and peak area was observed. Perkins observed that the appearance of C_1 was influenced by the reduction of oxide products formed at A_1 [220]. At E_a > -0.8 V A_1 remains unchanged, which could be explained as oxidation of Ga^0 to Ga(I) (Eq-2.3), an intermediate in the formation of trivalent Ga(III) through a disproportionation reaction. Varadharaj and Rao [218] also attributed the first Ga oxidation peak (A_1) to the formation of Ga_2O.

$$2Ga + H_2O \rightleftharpoons Ga_2O + 2H^+ + 2e^- \qquad [2.2]$$

$$3Ga_2O \rightarrow 4Ga + Ga_2O_3 \qquad [2.3]$$

Following peak A_1 a steady increase in current was observed with increasing potential. Perkins suggested that this increase can be attributed to the continuous formation of Ga_2O_3 [221]. Hence, increasing formation of Ga_2O_3 is believed to proceed as described in Equations 2.2 followed by Equation 2.3.

Ga(III) oxides formed from Equations 2.1-2.3 can be electrochemically reduced to Ga metal as suggested by Equation 4. Proposed mechanisms suggest the intermediate formation of Ga_2O

(Equations 2.2 and 2.3) during the reduction of Ga_2O_3. The formation of Ga_2O cannot be ignored because the reduction potential for the redox couples Ga^{3+}/Ga^{+} and Ga^{+}/Ga^{0} -0.40 V and -0.53 vs SHE, respectively, are relatively close [206], [222]. Monnens et al. confirmed the formation of Ga(I) as an intermediate in the formation of Ga^0 (Equations 2.4-2.6) [208] with a rotating ring disk electrode (RRDE) collection experiment in non-aqueous electrolytes. During their experiments, an increase in ring current was attributed to the reduction of Ga(I) species formed at the disk and collected at the ring.

$$Ga_2O_3 + 6H^+ + 6e^- \rightarrow 2Ga + 3H_2O \quad [2.4]$$

$$Ga_2O_3 + 4H^+ + 4e^- \rightarrow Ga_2O + 2H_2O \quad [2.5]$$

$$Ga_2O + 2H^+ + 2e^- \rightarrow 4Ga + H_2O \quad [2.6]$$

Flamini *et al.* [207] also observed that at low current densities, Ga(III) is reduced to Ga(I). Also, the presence of Ga(I) is reported by Hong *et al.* [209].

Figure 2.4 shows the integration of the anodic and cathodic sweeps at various E_a values for the Ga electrode in LiOAc electrolyte. No background subtraction was performed in this analysis. The charge of the cathodic sweep has a gradual increase and plateaus when E_a is over -0.2 V. The anodic sweep charge shows a steady increase as E_a approaches more positive values. A tentative explanation of the greater charge values for oxidation could be the partial dissolution of trivalent gallium species into the electrolyte.

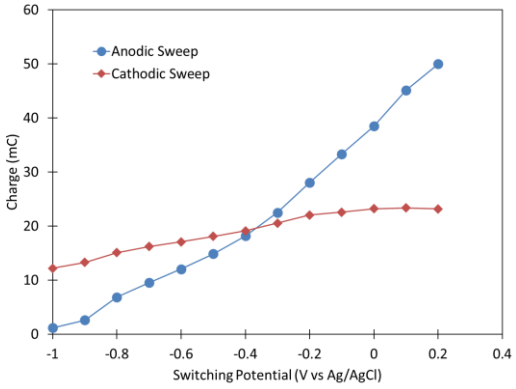

Figure 2.4. Blue line represents the anodic sweep charge, and the red line represents the cathodic sweep charge taken from -1 V to 0.2 V vs Ag/AgCl switch potential.

Accordingly, based on the cathodic peak charge value for peak C_1, the approximate oxide thickness calculated from the reduction peak C_1 is shown in Figure 2.5. This plot shows a relatively thin oxide layer (<10 nm) forming with E_a negative of 0.2 V and growing steeply at more positive values.

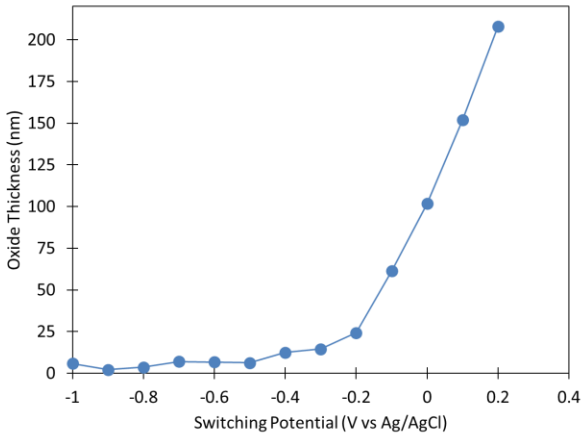

Figure 2.5. Oxide thickness is estimated through integration of peak C_1 as a function of E_a.

Cyclic voltammetry scan rate study in the absence of Pr

Evaluation of the peak current density (j_P) as a function of the scan rate (v) was performed to better understand the redox mechanisms of Ga. The CV curves acquired in these experiments are provided in Figure 2.6 where E_a was held at 0.2 V. Figure 2.7 shows that at lower ν a linear relationship of j_p with v and $\nu^{1/2}$ suggests a diffusion-controlled mechanism.

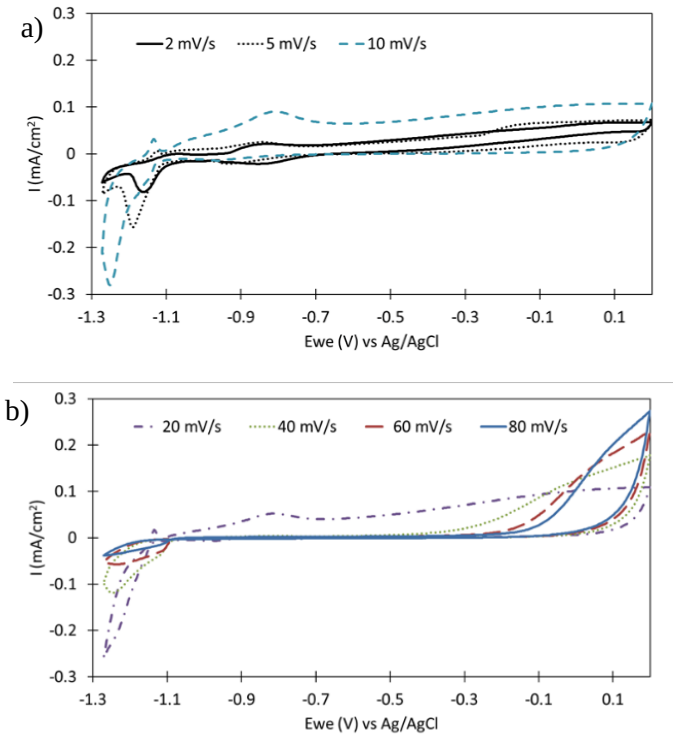

Figure 2.6. Cyclic voltammetry scan rates for 0.15M LiOAc blank solution ranging from a) 2 mV/s (black solid curve), 5mV/s (black dotted curve), 10 mV/s (blue dashed curve) and b) 20 mV/s (purple dotted curve), 40 mV/s (green dotted curve), 60 mV/s (red dashed curve) to 80 mV/s (blue solid curve).

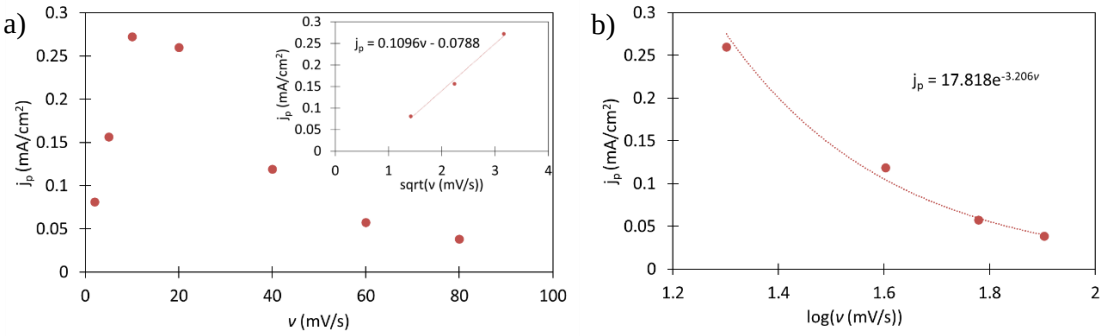

Figure 2.7 Peak current density (j_P) vs scan rate (v) showing a diffusion-controlled mechanism at lower scan rates and a kinetic controlled mechanism at higher scan rates. Suggesting that the Ga-LiOAc system is diffusion and kinetic controlled.

A galvanostatic charging test conducted by Perkins (1979) [220] showed a diffusion-controlled process in a similar potential window. In his work, an *i-t* plot from the galvanostatic charging test displayed a slope characteristic similar to a diffusion-controlled process ($it^{1/2}$), further suggesting that the oxidation region is diffusion controlled.

However, at higher v values, the exponential decrease of j_P with the v, suggests a kinetic controlled process where the electron transfer process is followed by a catalytic reaction. The mechanism as suggested by Nicholson and Shain [223] can follow either a catalytic reaction with reversible charge transfer shown in Equations 2.7-2.8.

$$O + ne \rightleftharpoons R \qquad [2.7]$$

$$R + Z \overset{k'f}{\longrightarrow} O \qquad [2.8]$$

or catalytic reaction with irreversible charge transfer shown in Equations 2.9-2.10.

$$O + ne \overset{k}{\rightarrow} R \qquad [2.9]$$

$$R + Z \overset{k'f}{\longrightarrow} O \qquad [2.10]$$

The first mechanism involves an irreversible catalytic reaction similar to that proposed by Perkins (1972) in Equation 2.2 [221]. This reaction is preceded by a reversible reaction. In both mechanisms, the catalytic reaction could be attributed to the disproportionation of electrochemically formed Ga_2O. The possibility of both reaction mechanisms occurring separately or simultaneously lies in the stability and instability of Ga surface oxides. Consequently, at higher scan rates the disproportionation reaction is the rate limiting step. This affects the amount of Ga_2O_3 accumulated, therefore, the magnitude of the reduction peak C_1 decreases.

Cyclic voltammetry of supporting electrolyte with Pr

Following the CV assessment of Ga in the supporting electrolyte, PrOAc was introduced into the electrolyte. Figure 2.8a shows a reduction peak (approximately -1.2 V), C_1, with a featured current density one magnitude greater (Insert Figure 2.8b) than the reported for peak C_1 in the absence of Pr (Figure 2.3). During the backward scan, the peak corresponding to hydrogen desorption (peak A* in Figure 2.3) is not observed. Subsequent cycles in the same scan range show a gradual decrease in the current density of peak C_1. When E_a is kept below -0.4 V, the current density of C_1 decreases, and eventually C_1 disappears as shown in Figure 2.8a.

Figure 2.8b shows that as E_a was increased above -0.4 V, C_1 reappeared and increased in current density. This suggests that Ga oxides may be key to the formation of Pr-Ga products observed in bulk electrolysis experiments presented below. Also, a nucleation loop (current on return sweep exceeding that of the forward sweep) was observed when more positive E_a values were applied. The appearance of the nucleation loop suggests the presence of an oxide layer whose thickness prevents the diffusion of Ga species. When this occurs, rather than diffusing through the oxide layer, metallic Ga likely accumulates on the surface of the oxide layer, acting as an extension to the surface area. Monnens et al. also observed this phenomenon while investigating the electrochemical behavior and deposition of Ga in 1,2-dimethoxyethane (DME) electrolytes [208].

Concentration of Pr vs current density

CV tests were performed with Pr concentrations from 15 mM to 50 mM to verify that the increase in current density of peak C_1 is directly associated to the presence of Pr. The insert in Figure 2.8a shows a linear relationship between the charge density of peak C_1 and the concentration of Pr, confirming that the increase in current density is due of the presence of Pr in solution and likely associated to Pr reduction.

Cyclic voltammetry scan rate study in the presence of Pr

A scan rate analysis was also performed after introducing Pr into the background electrolyte. Figure 2.9 illustrates CVs used to determine j_P as a function of v, where E_a was maintained at 0.2 V. These curves were analyzed to produce the data in Figure 2.10. The inset for Figure 2.10a shows that in the presence of Pr a linear relationship of j_p with v and $v^{1/2}$ is observed, suggesting a diffusion-controlled mechanism up to 10 mV/s. At higher scan rates an exponential decrease of j_P with v suggests a kinetically controlled process.

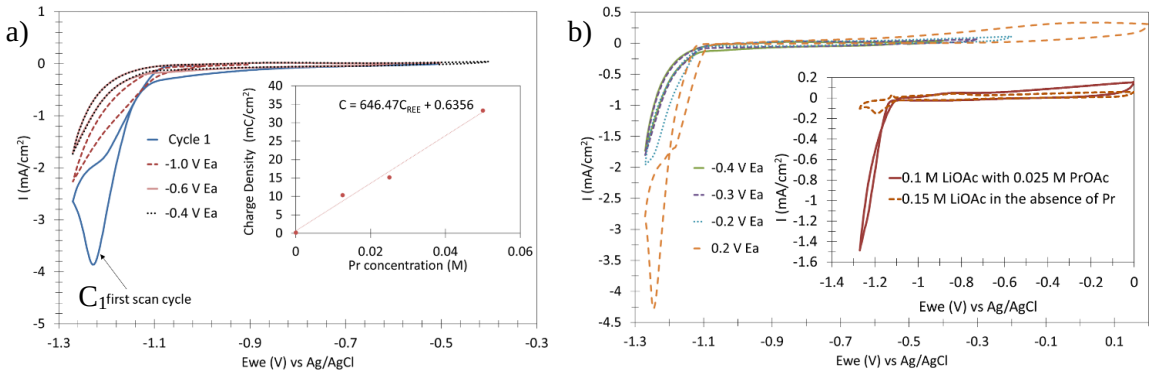

Figure 2.8 CV plots of Ga cathode at 10 mV/s a) in the presence of Pr with E_a -0.4 V (black dotted curve), -0.6V (solid pink curve), -1V (red dashed curve) with insert showing peak current for C_1 as a function of Pr concentration and b) in the presence of Pr with E_a above -0.4 V with insert comparing CV curves with (red curve) and without Pr (dark orange dashed curve).

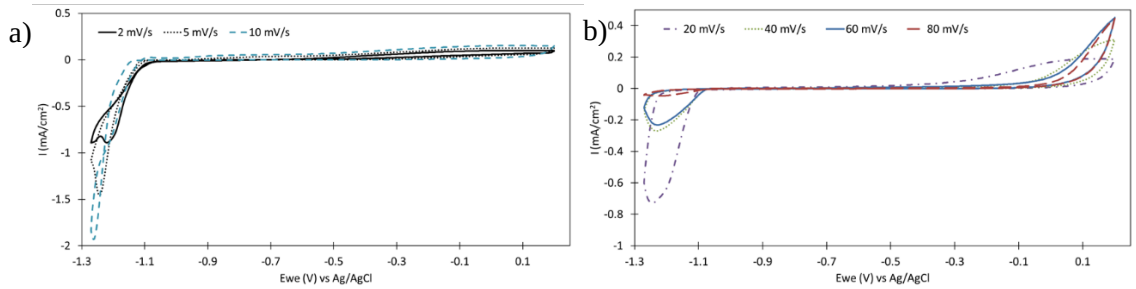

Figure 2.9. Cyclic voltammetry scan rates for 0.125M PrOAc with 0.1M LiOAc blank solution ranging from a) 2 mV/s (black solid curve), 5mV/s (black dotted curve), 10 mV/s (blue dashed curve) and b) 20 mV/s (purple dotted curve), 40 mV/s (green dotted curve), 60 mV/s (blue solid curve) to 80 mV/s (red dashed curve).

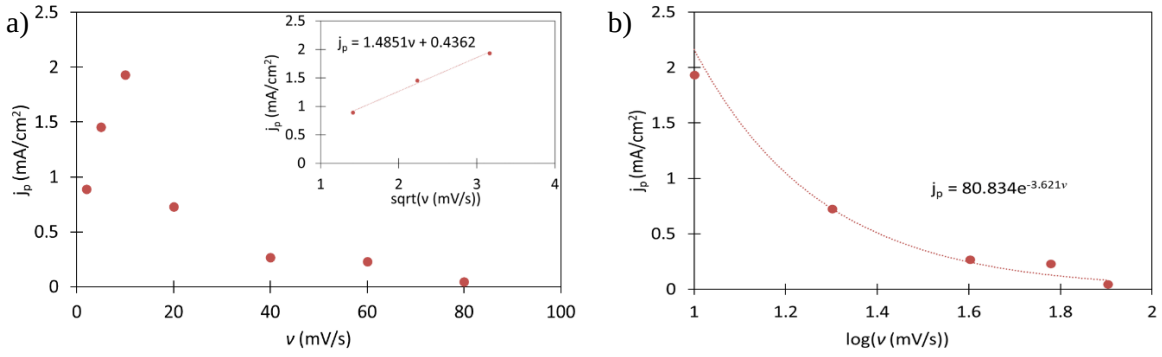

Figure 2.10. Peak current density vs scan rate showing a diffusion-controlled mechanism at lower scan rates and a kinetic controlled mechanism at high scan rates in the presence of Pr.

To this point is not clear what the effect of Pr is on the increase of cathodic current C_1. However, the kinetic analysis suggests that the reduction feature may involve a catalytic step as described in Equations 2.8 and 2.10. Further suggesting that Pr enhances Ga oxide formation possibly via chemical oxidation, prompting further studies.

Dark striations were observed on the surface of Ga as E_a approached more positive values in the presence of Pr. However, these striations disappeared as the sweep potential approached more negative values. These observations prompted a series of bulk electrolysis experiments designed to produce products for analysis.

Bulk electrolysis without flowing Ga cathode

Bulk electrolysis (BE) on a quiescent liquid Ga cathode was conducted in Pr containing electrolytes to investigate formation of Pr-Ga products. Chronoamperometric tests were carried out at potentials positive (-1.0 V) and negative (-1.3 V and -1.5 V) of the C_1 reduction feature. Tests at -1.0 V showed no visible qualitative changes on the surface of the Ga electrode throughout the duration of the experiment. At potentials of -1.3 V and -1.5 V, the formation of a light green precipitate was observed on the surface of the Ga as shown in Figure 2.11 shortly after the Ga surface transitioned from a dull to shinny look. ICP-MS analysis of the catholyte after electrolysis, illustrated in Figure 2.12, shows that the percentage of Pr removed from the catholyte increased (from 13% at -1.0 V, to 21% at -1.3V, and 35% at -1.5 V) as the potential was shifted to more negative values.

Following electrolysis, the liquid Ga was washed with DI water and digested in 1 M HCl to investigate the amount of Pr reduced into the surface of the Ga electrode. ICP-MS results of the digest showed that the amount of Pr captured into the Ga was only 0.1% at -1.0 V, 1.3% at -1.3 V and 1.1% at -1.5 V. These minuscule values do not agree with the loss of Pr removed from the catholyte illustrated in Figure 2.12. From Figure 2.3, it is seen that potentials below -1.2 V fall in the HER region. In this region, the formation of the light green precipitate can be explained as the precipitation of $Pr(OH)_3$ which follows Equations 2.11-2.12.

$$6H_2O + 6e^- \rightarrow 6OH^- + 3H_2 \qquad [2.11]$$

$$2Pr^{3+} + 6OH^- \rightarrow 2Pr(OH)_3 \qquad [2.12]$$

The ICP-MS analysis strongly suggests that the decrease in Pr concentration in the catholyte can be largely attributed to the formation of $Pr(OH)_3$. This analysis also suggests that even at potentials such as -1.0 V where the Ga is not being reduced, the removal of Pr via some other reaction path can be facilitated. XRD analysis of the green precipitate showed a highly amorphous material with a weak

match for $Pr(OH)_3$ as seen in Figure 2.13. However, hydroxide rather than acetate is a more feasible product considering that acetate complexes are weaker. The results of the BE experiments suggest that bulk Pr reduction without stirring of the Ga surface does not take place at potentials below -1.2 V. Furthermore, these results do not provide insight about the increase in current density observed for reduction peak C_1 with Pr present. A key component absent from the initial BE experiments was the presence of Ga oxide which seem to play a significant role in the magnitude of the featured cathodic current.

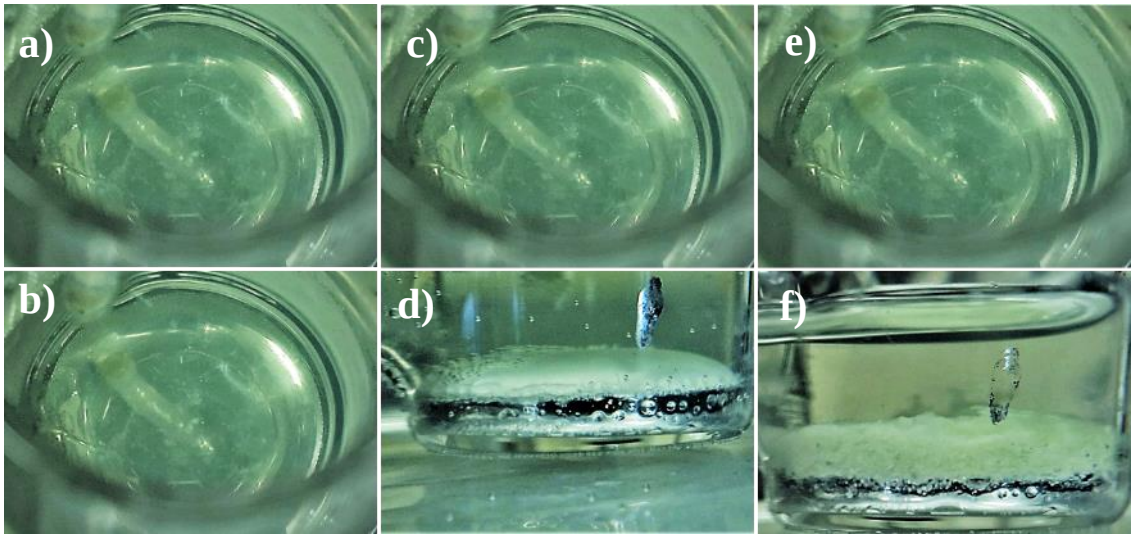

Figure 2.11. Images of non-agitated Ga pool experiments before (top) and after (bottom) experiment, a) -1.0 V vs Ag/AgCl, b) -1.3 V vs Ag/AgCl and c) -1.5 V vs Ag/AgCl.

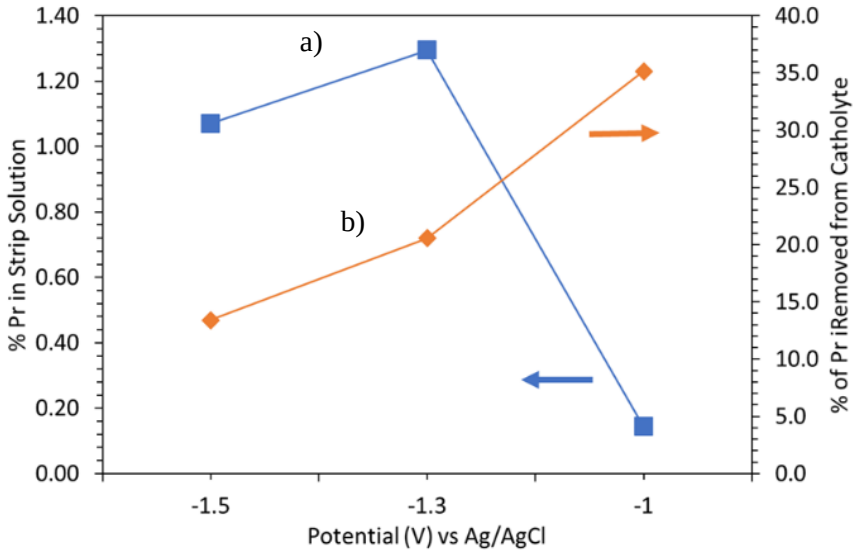

Figure 2.12 a) Blue line (□) represents the percentage of Pr in the leachate after stripping the liquid Ga in 1 M HCl. b) Orange plot (◊) shows the % of Pr removed from the catholyte during the electrolysis.

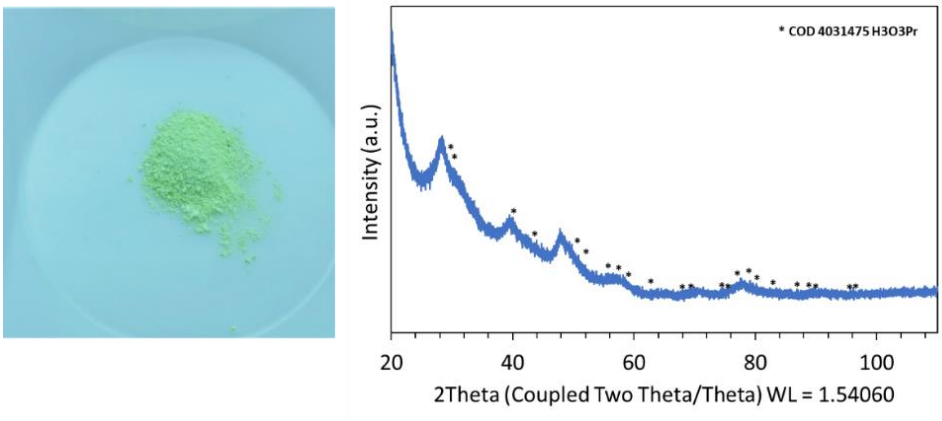

Figure 2.13. XRD analysis of precipitate after performing electrolysis with an applied potential of -1.5 V.

Bulk electrolysis with flowing Ga cathode

Chemical oxidation of Ga was promoted via an external circulation loop where Ga was unloadd drop by drop in the catholyte as a modification to the previous BE experiments. Dropping Ga through the catholyte into the pool allowed the formation of Ga oxides through chemical reaction when outside the pool (Figure 2.1b). Figure 2.14a shows the formation of a gray precipitate in the presence of Pr, which started forming even before any potential was applied. This occurs because the OCP of the Ga in this system is more positive than -0.9 V and lies in the region of Ga oxide formation. This gray precipitate was not observed when Ga was recirculated in LiOAc electrolyte in the absence of Pr, or in DI water. The formation of the gray precipitate, even in the absence of applied potential, was the first experimental suggestion that a disproportionation reaction involving Ga^{+} and Pr^{3+} may play a role in the formation of a Pr-Ga product.

Understanding the effects of potential on the gray precipitate formation and its correlation to Pr, prompted separate 20-hr experiments with Ga recirculation at different potential scenarios. BE experiments were performed at OCP, -1.2 V and -1.3 V in an electrolyte containing LiOAc and PrOAc. For all these conditions, the gray precipitate was produced as Ga was circulated. When -1.2 V was applied to the system, an average current density increase of -0.246 mA/cm^2 was observed as Ga drops fell into the liquid Ga cathode as shown in Figure 2.14b. When filtered from the catholyte, and analyzed, the gray precipitate shown in Figure 2.14c contained >50% of the Pr initially present in the catholyte. The gray precipitate formed a distinctive solid phase that facilitated its separation from the liquid Ga. Digestion of the gray precipitate in 1 M HCl leaves a residue of Ga metal. During HCl digestion H_2 gas formation was observed, suggesting that the gray precipitate could have contained some Pr in the reduced state. While the gray precipitate remained solid after drying at 80 °C, the residual Ga from digestion of the gray precipitate in HCl melted at temperatures close to 30 °C as its original state.

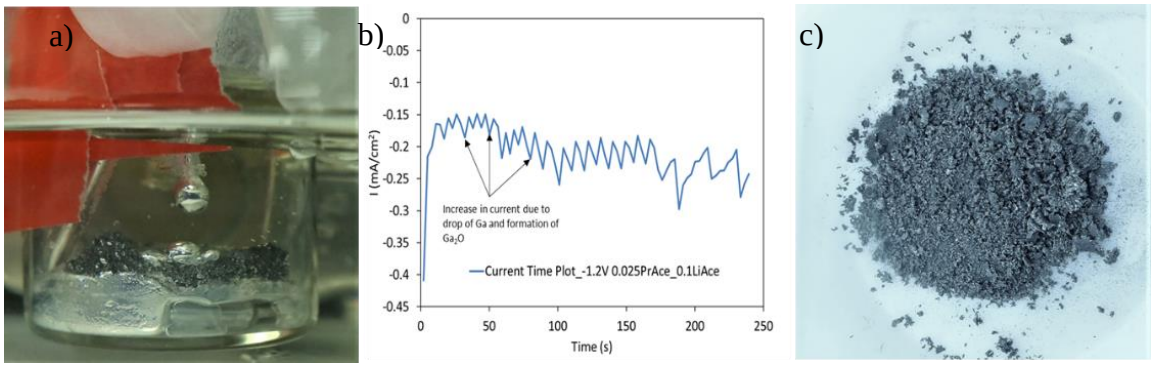

Figure 2.14. BE experiment at -1.2 V vs Ag/AgCl. a) Dropping of liquid Ga with gray precipitate formed in the presence of 0.05 M PrOAc and 0.1 LiOAc electrolyte at 30 ° C, b) current vs. time curves while dropping Ga into the pool, and c) gray precipitate from electrolyte after BE after drying at 80 °C.

The phase diagram of the Pr-Ga system shown in Figure 2.15 suggests that a phase transformation from liquid gallium to solid product can be promoted by minimum additions of Pr. For example, the addition of as little as 1% Pr could result in the formation of an alloy with a melting point close to 200 °C. However, the formation of the gray precipitate does not prove that an alloy has been formed, or that Pr is being reduced. Rather it suggests the presence of some chemical reaction involving the Ga oxide and Pr where a different phase was formed.

The application of a suitable reducing potential is needed to facilitate the removal of Pr in significant amounts from the catholyte. Table 2.1 shows that for a solution with 50 mM PrOAc, the amount of Pr removed from the catholyte, and captured in the gray precipitate, with and without potential application was 53.9% and 1.6 %, respectively. In the absence of applied potential, the formation of precipitate occurs but is limited by the formation of the unstable Ga_2O intermediate. Applied potential promotes the reduction of Ga(III) favoring continuous regeneration of Ga(I) and therefore co-disproportionation as hypothesized in Equations 2.13-2.15, which in the presence of Pr enhances the formation of the Pr-Ga product according to the Equations 2.13 and 2.14.

$$3Ga_2O_3 + 12H^+ + 12e^- \rightarrow 3Ga_2O + 6H_2O \qquad [2.13]$$

$$3Ga_2O + Pr^{3+} \rightarrow Ga_3Pr + 3GaO^+ \qquad [2.14]$$

$$2GaO^+ + H_2O = Ga_2O_3 + 2H^+ \qquad [2.15]$$

Higher Pr removals from the electrolyte, up to 83%, were obtained at -1.3 V. However, the characteristics of the product formed at -1.3 V are like those obtained during the bulk electrolysis experiments without agitation. This suggests a different mechanism, which could include the

formation of $Pr(OH)_3$ influenced by high local pH at the cathode surface promoted by HER as discussed above.

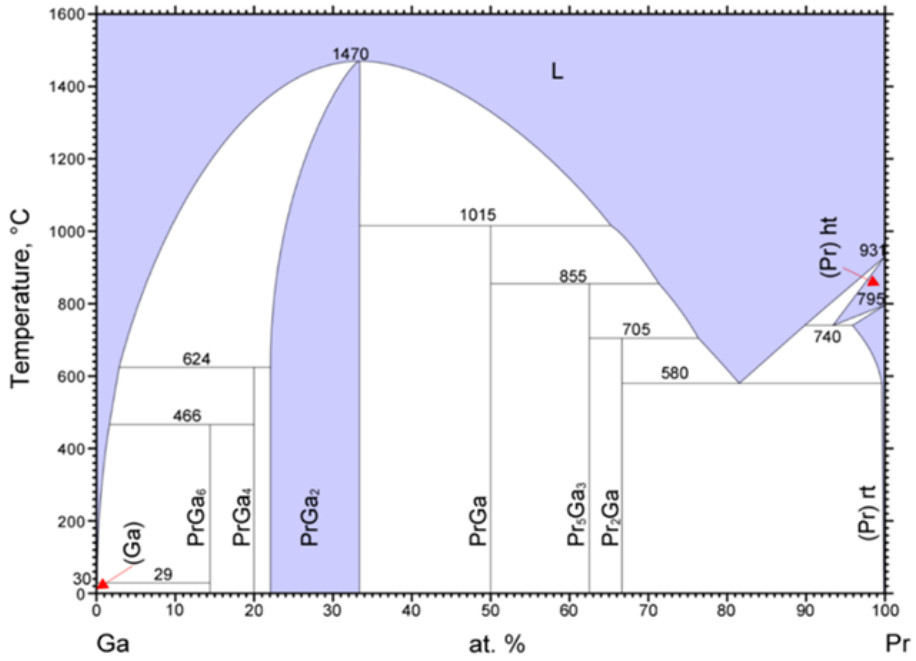

Figure 2.15. Equilibrium phase diagram for the Ga-Pr system.

Table 2.1 Percentage of Pr captured in the gray precipitate from the electrolyte.

Catholyte Composition	Potential (V)	Charge (C)	Time Run (hr)	Initial pH	Final pH	%Pr captured in precipitate
25 mM PrOAc	-1.3	180	20.0	6.5	11.0	83.3
25 mM PrOAc	-1.2	88	20.0	6.9	9.6	69.2
50 mM PrOAc	-1.2	122	20.0	6.5	7.8	53.9
50 mM PrOAc	No Potential	0	20.0	7.2	6.9	1.6

Characterization of the precipitate

SEM and EDS were employed to determine morphology and composition of the gray precipitate. Figure 2.16a and Figure 2.17, and Figure 2.16b are SEM images of the gray precipitate obtained at -1.2 V and -1.3 V, respectively. While both experiments were performed for the same length of time and in the same atmospheric conditions, a change in potential influenced the precipitate surface morphology. Comparisons between the precipitates for -1.2 V and -1.3 V suggests a coarser and aggregated texture at -1.2 V and a smoother texture at -1.3 V. EDS analysis of the precipitate obtained at -1.3 V shows a higher oxygen content than that obtained at -1.2 V as shown in Figure 2.16a.

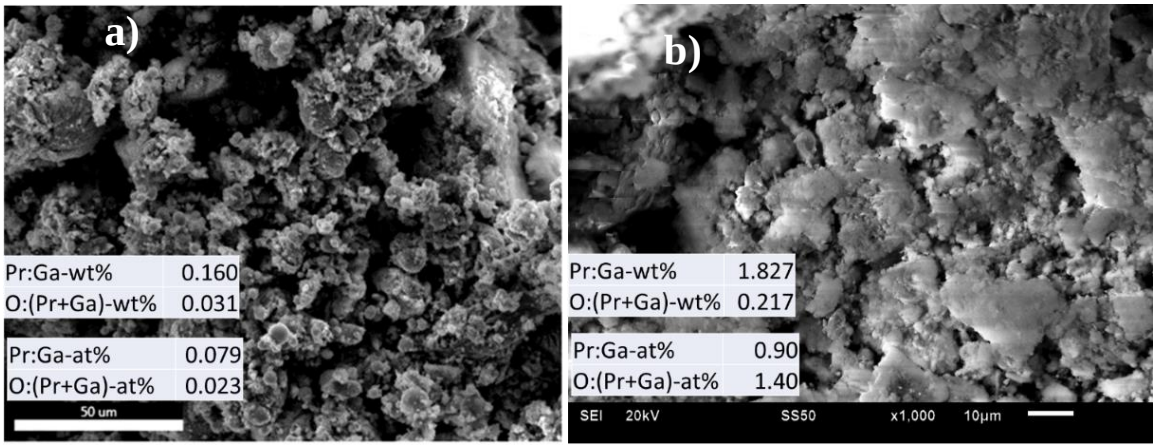

Figure 2.16. SEM images of the gray precipitate at a) -1.2 V and b) -1.3 V. The inserts are wt% ratios and atomic percent (at%) ratios based on EDS analysis.

Furthermore, EDS analysis of the precipitate obtained at -1.2 V (Figure 2.17a) show the presence of both Pr and oxygen in the precipitate. Close observation of Figure 8b, shows a spatial agreement between areas of high O and Pr, suggesting Pr oxides formed. A tentative explanation for this phenomenon could be that though the Pr can be reduced in the liquid Ga electrode, the product might not be stable in aqueous solution and undergoes rapid oxidation by reaction with water, leading to the formation of oxides.

These observations from the EDS analysis prompted further XRD analysis. Figure 2.18 shows that Ga metal is the only crystalline phase that can be identified from the product obtained at -1.2 V. The absence of identifiable Pr species suggests that no Pr metal or Ga-Pr alloys exist as a crystalline structure in the powder. This agrees with observations in Figure 2.17b. Further analysis of the overall oxygen content revealed an average value of 38 wt% O. Also, analysis of the gray precipitate by Raman spectrum as seen in Figure 2.19 shows the presence of Ga_2O_3 and Pr_2O_3 peaks with comparable values to Wang [224] , Zarembowitch [225], and Gouteron [226]. A combination of Ga_2O_2 and Pr_2O_3 can be seen at 414.60 cm^{-1} and at 163.34 cm^{-1}. A closer observation of the Raman spectrum shows that the precipitate is composed mainly of Ga oxides. Additional characterization can be found in the accompanying supplementary document.

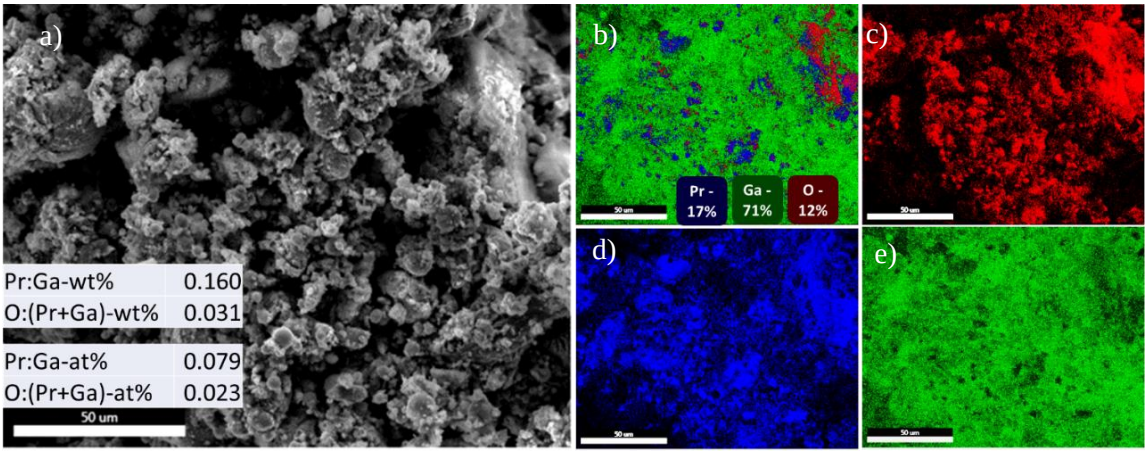

Figure 2.17. a) SEM imagery of gray precipitate at -1.2 V. b) EDS mapping showing Ga, Pr and O distribution at x100 at -1.2 V, c) red color O, d) blue color Pr, and e) Green color Ga.

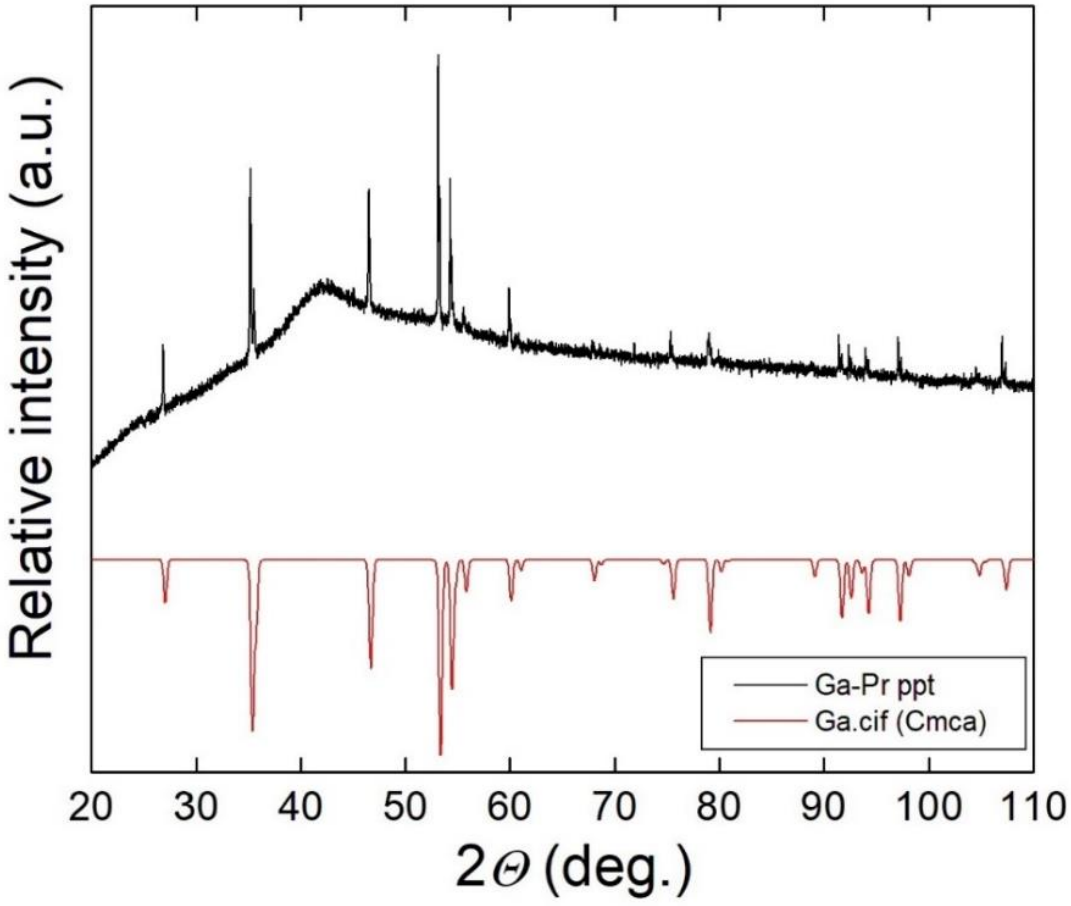

Figure 2.18. XRD analysis for precipitate (black) with a reference Ga spectrum (red). Prominent and matching peaks suggest a crystalline Ga structure in the precipitate. No additional peaks are observed for crystalline products involving Pr.

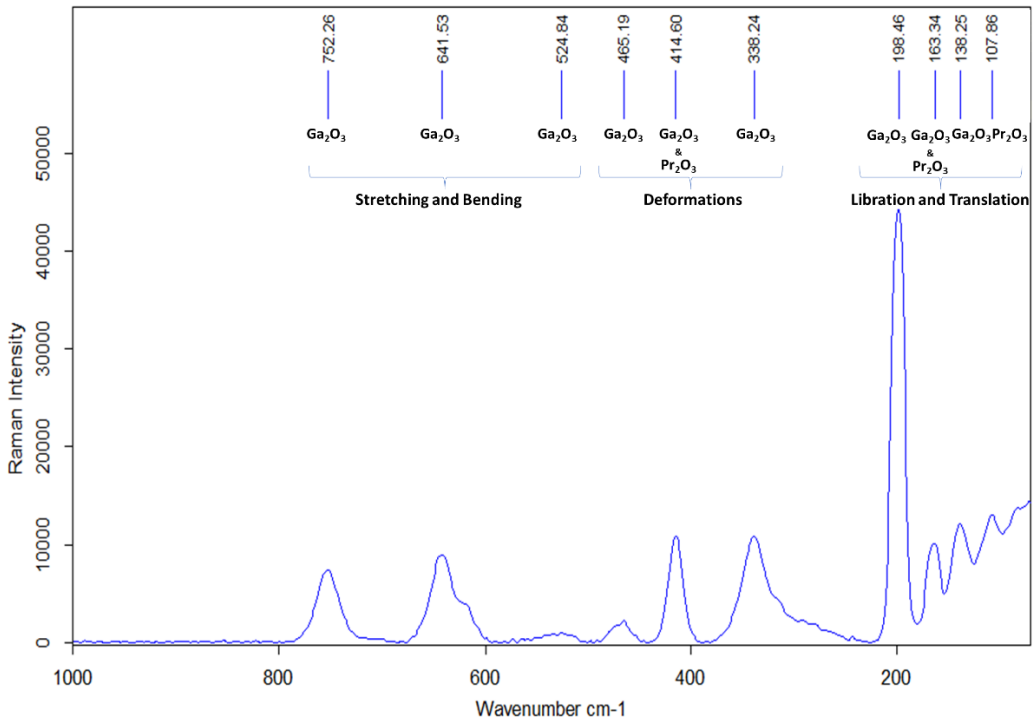

Figure 2.19. Raman spectrum of dark gray precipitate.

Conclusion

An alternate path to REE processing was investigated using liquid Ga as a cathode material. The reduction of Ga oxides in the presence of Pr showed an order of magnitude increase, when compared to in the absence of Pr, accompanied by the formation of a solid powder phase rich in Pr. Window opening CV and scan rate analysis established that Ga reduction follows a kinetic controlled mechanism where a catalytic reaction follows an electron transfer. This mechanism was then explained by means of Ga disproportionation, which is enhanced by the presence of Pr. Therefore, Pr enhanced disproportionation led to the formation of an additional solid phase (gray precipitate) during BE where > 50% of the Pr can be concentrated from diluted aqueous electrolytes. The formation of this gray precipitate only occurred when Ga was circulated and introduced back into the Ga pool via a pump. Circulation of the liquid Ga enabled the formation of surface oxides which are crucial for the formation of the gray precipitate. Furthermore, digestion of this precipitate in 1 M HCl produced H_2 gas and returns Ga to its original state. The above process discussed proves the feasibility of recovering REEs in a solid concentrate using liquid Ga cathode redox chemistry as capture mechanism.

Chapter 3: Preliminary Investigation of MnO_2 as Possible Metal Oxide Host Material for Immobilized Neodymium in Aqueous Neodymium Chloride

Introduction

Electrochemical intercalation has gained keen interest among researchers due to its versatility and reversible nature[169]. During electrochemical intercalation, the host material undergoes an electrochemical reduction, and positively charged ions are driven into the van der Waal gaps of the host material as seen in Figure 3.1 [138]–[141]. This creates materials with unique capabilities, stoichiometry, and characteristics [141].

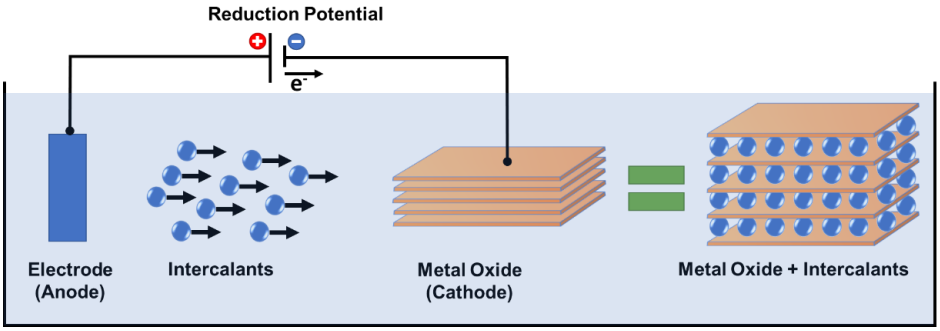

Figure 3.1. *The electrochemical intercalation process.*

A vast number of cations such as Li [175]–[179], Na [180]–[184], K [185]–[188]and Zn [189]–[191] have been studied for intercalation into various host material for energy storage applications. While intercalation has been extensively employed for energy storage, its possibilities could translate to other applications such as rare earth elements (REEs) recovery and recycle. Such applications could include concentration of REEs from dilute streams. Furthermore, this could bridge the gap between aqueous and ionic electrolytes for REE capture and reduction since in ionic electrolyte water hydrolysis before REE reduction to metal is avoided [197].

However, one of the draw backs for the reduction of rare earth elements (REEs) in near ambient temperate ionic environments is the need of a suitable material as the anode. While most research have evolved around the design of the cathode, there is the possibility of designing the cell around the anode. A promising path to solving this anode setback is to facilitate an anode reaction through a feeder electrode. This would employ the use of a conductive metal oxide electrode intercalated (loaded) with REEs which can be unloaded with the application of an anodic potential similar to Li

batteries [142]–[144] into an ionic electrolyte for further reduction to metal. Furthermore, stability of the host material under the influence of an external potential is key for successful intercalation [139].

Metal oxide electrodes such as manganese oxides (MnO_2) have sparked interest among researchers due to their promising characteristics [191] [192] [193]. Compared to metal electrodes, the presence of redox couples present in metal oxides such as MnO_2, permit the enhancement of reaction rates and hinder the surface adsorption of hydrogen [172] [173]. The most preferred form of manganese oxide is manganese dioxide (MnO_2) due to good electrochemical stability under various charge and discharge conditions, as well as purity [227]. However, due to the poor conductivity of MnO_2, conductive chemicals such as carbon (between 10 and 30 wt%) is added to boost electrical conductivity [228].

Pang et al. [193] suggested that the mechanism governing the intercalation of MnO_2 can be described by equations 3.1 and 3.2:

$$MnO_2 + H^+ + e^- \leftrightarrow MnOOH \qquad [3.1]$$

or

$$MnO_2 + C^+ + e^- \leftrightarrow MnOOC \qquad [3.2]$$

where C represents cations such as Na^+, K^+, or Li^+ or possibly Nd^{3+}. In a paper by Toupin et al, the thickness and characteristics of MnO_2 was investigated [194]. They concluded that due the agglomeration of MnO_2 when deposited, thin films performed better than thick films [194]. This chapter hereby investigates the loading of REE (Nd) into MnO_2, and the subsequent unloading of Nd^{3+} into a blank aqueous electrolyte and ionic electrolyte.

Experimental

Materials

Analytical grade MnO_2, potassium chloride (KCl) and neodymium chloride ($NdCl_3$) tetrahydrate 99.9%, were used for electrolyte preparations in deionized water (DI) (>18 MΩ). 1-Butyl-1-methylpyrrolidinium Trifluoromethanesulfonate was used as the ionic liquid.

Electrode Preparation

Two slurries were made for two types of the MnO_2 electrode. One was made without carbon (80 wt.% MnO_2, 20 wt.% PVF) and with carbon (80 wt.% MnO_2, 10 wt.% C, 10 wt.% PVF). Carbon was added to enhance conductivity. The solvent was N-methyl-2-pyr-rolidone. Analytical grade MnO_2, PVF and N-methyl-2-pyr-rolidone was used. Carbon powder (Carbon Black - Vulcan XC 72R) was obtained

from FUELCELL Store. Slurries were then painted on carbon paper (Toray Teflon Treated Carbon Paper- 060 - TGP-H-060) substrates from FUELCELL Store. The electrodes were dried following a step wise approach to avoid exfoliation and detachment of the attached layer: first air dried at room temperature, followed by drying at 60 °C for four hours followed and a final drying at 120 C overnight.

Electrochemical measurements

Cyclic voltammetry (CV) experiments and bulk experiments were conducted in a single cell as shown in Figure 3.2. The working electrode was MnO_2. The scan rate was 20 mV/s. The auxiliary electrode was Pt for CV and bulk electrolysis (BE), respectively. Potentials were measured and reported versus an Ag/AgCl (3 M NaCl) (BASi) reference electrode. BioLogic SP-50 potentiostat controlled by EC-Lab software was used to preform Chronoamperometry and Chronopotentiometry experiments. IR compensation was applied to CV curves and bulk experiments.

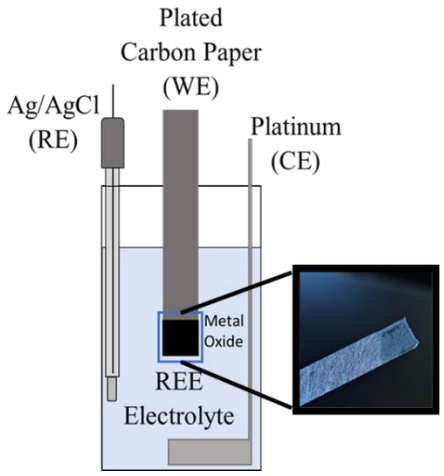

Figure 3.2**.** Single compartment setup for CV experiments and bulk experiments. A stir bar was used during bulk experiments to circulate electrolyte.

Material analysis and characterization

Following Chronoamperometry and Chronopotentiometry experiments in $NdCl_3$ electrolyte, the MnO_2 electrode was taken out of the cell and rinsed with copious amounts of DI water. The electrode was then transferred to a KCl electrolyte for unload of any adsorbed Nd^{3+} ions. Following deintercalation of Nd^{3+} ions, the electrode was digested in 3:1 HCl-HNO_3 for ICP-MS analysis to obtain and accurate mass loading for MnO_2.Concentrations of Mn and Nd^{3+} were measured using an iCAP Q inductively coupled plasma mass spectrometer (ICP-MS) (Thermo Scientific).

Redox charge and peak analysis measurements employed the use of EC-Lab V.11.33 by BioLogic Instruments. Charge calculation without background subtraction employed the use of EC-Lab integration function.

SEM and EDS analysis of electrode samples prior and after electrolysis were conducted employing the use of a JEOL JSM-6610LV and EDAX AMETEK Apollo X controlled by EDAX software. SEM and EDS allowed the study of surface morphology, elemental composition, and elemental distribution. SEM and EDS samples were prepared by placing the electrodes unto double sided carbon tape and then securing the sample holders.

Results and Discussion

Cyclic Voltammetry on MnO_2 in KCl and $NdCl_3$ solutions

CV experiments of the MnO_2 electrode without carbon powder was undertaken in 1 M KCl electrolyte and 1 M KCl with a 100mM $NdCl_3$ additive, respectively. Figure 3.3a shows the CV with MnO_2 electrode in 1 M KCl between -1.2 and 1.2 V vs. Ag/AgCL. Oxidation peaks a_1, a_2, and a_3 are observed at approximately -0.25 V, 0.65 V and 1.0 V respectively. Concurrently, associated reduction peaks, c_1, c_2, and c_3 are observed at approximately -0.45 V, -0.1 V, and 0.9 V respectively. The c_2 and c_1 peaks are attributed to the two-step reduction of Mn^{4+} to Mn^{3+} and M^{3+} to Mn^{2+} respectively [229], [230], while peaks a_1 and a_2 correspond to the oxidation of Mn^{2+} to Mn^{3+} and Mn^{3+} to Mn^{4+} respectively. Based on previous studies, peaks c_3 and a_3 likely correspond to the reduction of aqueous $Mn^{4+}_{(aq)}$ to Mn^{3+} and the oxidation of Mn^{3+} to $Mn^{4+}_{(aq)}$ respectively [229], [231]. Reactions of peaks are shown by the following equations:

$$Mn^{2+} \rightleftharpoons Mn^{3+} + e^- \ldots\ldots\ldots \left[{a_1}/{c_1} = {-0.25\ V\ vs\ Ag/AgCl}/{-0.45\ V\ vs\ Ag/AgCl}\right] \quad [3.3]$$

$$Mn^{3+} \rightleftharpoons Mn^{4+} + e^- \ldots\ldots\ldots \left[{a_2}/{c_2} = {0.65\ V\ vs\ Ag/AgCl}/{-0.1\ V\ vs\ Ag/AgCl}\right] \quad [3.4]$$

$$Mn^{3+} \rightleftharpoons Mn^{4+}_{(aq)} + e^- \ldots\ldots\ldots \left[{a_2}/{c_2} = {1.0\ V\ vs\ Ag/AgCl}/{0.9\ V\ vs\ Ag/AgCl}\right] \quad [3.5]$$

Furthermore, the broadness of these peaks is indicative of a pseudocapacitive electrode and could suggest slow diffusion of species into the layers electrode [232]–[234]. Also, the almost rectangular shaped CV sweep for the insert in Figure 3.3a between ca. -0.1 and 1.2 V vs Ag/AgCl is due to the capacitive behavior of MnO_2 in KCl. Lee and Goodenough observed this behavior while working with MnO_2 in KCl electrolyte [235]. This phenomenon occurs when the rate of discharge and charge is constant over a given cycle. Upon voltage reversal at the cathodic and anodic switch potentials, the rapid current response is as a result of the expeditious chemisorption and desorption of the K^+ ion in

the KCl electrolyte [235]. Suggesting that the intercalation of cations may be preceded by surface adsorption followed by diffusion [231]. Furthermore, upon voltage reversals at -1.2 V vs Ag/AgCl and 1.2 V vs Ag/AgCl the increase in current density is attributed the hydrogen and oxygen evolution respectively (water electrolysis).

It is noteworthy to mention that in the presence of Nd^{3+}, the current response is significantly enhanced as seen in Figure 3.3b. With the addition of Nd^{3+}, the enhancement of one broad prominent oxidation peak can be seen at ca. 0.65 V with the related reduction peak at ca. 0.1 M. These peaks can be attributed to the Mn^{4+}/Mn^{3+} redox couple.

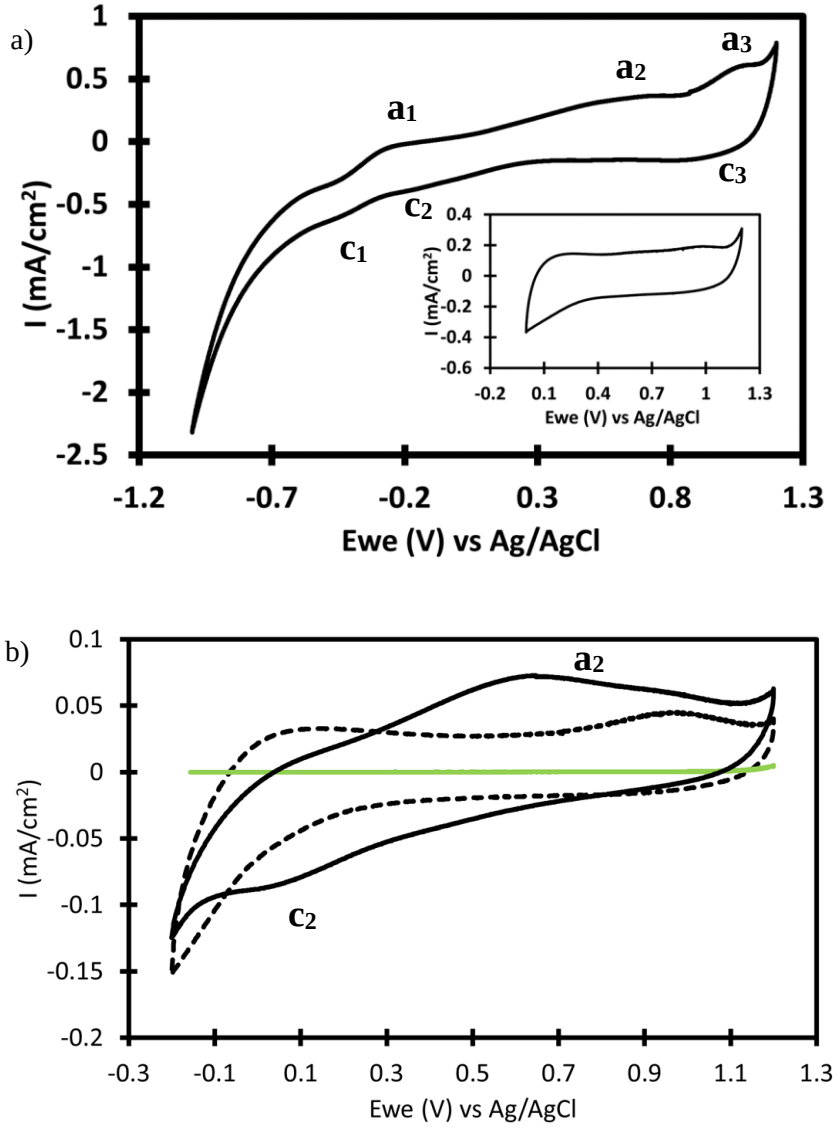

Figure 3.3**.** a) CV of MnO_2 in 1 M KCl scanned from 1.2 V to -1.2 V vs Ag/AgCl with insert scanned from 0V to -1.2 V. b) Green curve is CV of carbon paper in 1 M KCl, dashed black curve is CV of carbon paper and MnO2 in 1 M KCl, and solid black curve is CV of carbon paper and MnO2 in 1 M KCl +with a 100 mM $NdCl_3$ additive.

Verification Nd Contribution During Voltammetry Sweep

To verify that the observed peaks from Figure 3.3b, were enhanced by the addition of $NdCl_3$, the MnO_2 electrode was tested with common cations, 1 M KCl with additives of 100mM $NdCl_3$, 100mM NaCl, 100mM LiCl, and 100mM $ZnCl_2$. From Figure 3.4 it is observed that Zn and Nd enhance the redox peaks for Mn but are different. Variation in Nd^{3+} and Zn^{2+} sweeps could result from surface property and modification based on ion electrode interaction. Furthermore, CV plots for K, Na, and Li are similar to that reported by Wen et al [236]. This study proves that the peaks observed in Figure 3.3b is due to the addition of Nd^{3+}.

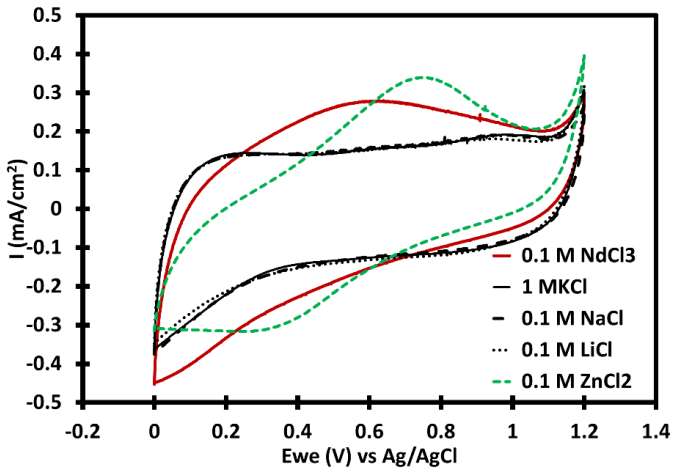

Figure 3.4**.** a) CV of MnO_2 in 1 M KCl and an additive scanned from 0V to -1.2 V vs Ag/AgCl at 20 mV/s.

To prove the reversibility of the electrode, anodic and cathodic charge sweeps were calculated and compared. Table 3.1 shows that the anodic sweep and cathodic sweep charge calculations are similar to each other based on the difference between the two values, indicating that all oxidative species formed during the oxidation sweep are reduced during the reduction sweep.

Table 3.1**.** Anodic and cathodic sweep charge for CVs of 0.1 M Nd, Na, Li and Zn in 1 M KCl with a potential range of 0 V to 1.2 V vs Ag/AgCl.

Element	Anodic Sweep Charge Density (mC/cm^2)	Cathodic Sweep Charge Density (mC/cm^2)
K	9.32	8.91
Nd	12.2	11.5
Na	9.24	8.89
Li	9.30	8.84
Zn	11.7	10.9
Nd after Zn	10.2	8.14

Concentration of Nd vs peak charge density

Electrolyte concentrations of 25mM to 100 mM Nd were investigated in 1 M KCl at 20 mV/s. Each CV test was followed by a ten-minute CA test at 1.0 V to deintercalate previous intercalated Nd ions. From Figure 3.5a, the addition of Nd^{3+} to the KCl electrolyte shows a stark increase of the cathodic peak current density. Furthermore, as the concentration of Nd increases, the current density increases. Figure 3.5b shows a linear relationship between the peak charge density and the concentration of Nd for 25mM to 100 mM with a R^2 correlation of 0.94. These findings confirms that the increase in charge density is a result of Nd concentration.

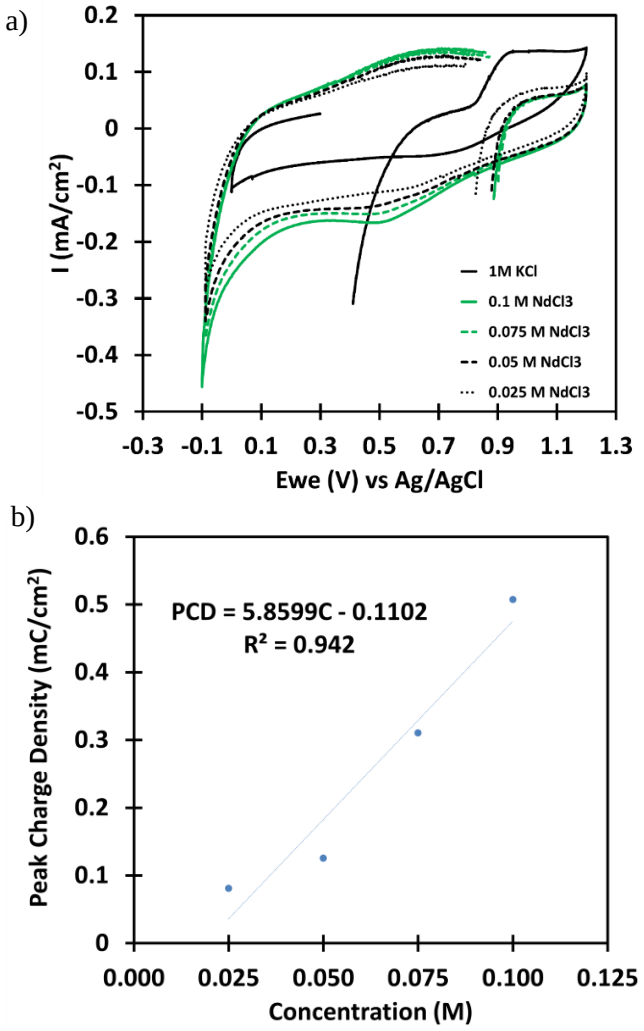

Figure 3.5. a) 25 mM, 50 mM, 75 mM, and 100 mM $NdCl_3$ + 1 M KCl CV concentration experiments with a potential window of -0.1 to 1.2 V vs Ag/AgCl and b) linear concentration of Nd with peak charge density.

Effect of Reduction Potential

To investigate the effect of potential on the immobilization process, a blank experiment where no potential was applied was compared against a potential driven immobilization experiment. The

electrolyte used was 1 M KCl with 100 mM $NdCl_3$. The potential applied was 0.5 V, and the electrolyte was agitated and lasted for two hours. Following both tests the electrode was washed with copious amounts of DI water and placed in acetonitrile to study any unload of Nd. Likewise, a 1.0 V potential was applied to the potential driven electrode to also study any unload of Nd. Following ICPM-S analysis, the ratio of Nd in the electrolytic experiment was four times greater than the immersion tests. EDS analysis as seen in Table 3.2 shows an average 8.7 increase in Nd wt% with the application of potential over the absence of potential.

Table 3.2. EDS data for average values for submerged (non-potential), applied potential and subsurface analysis.

	C-wt%	C-at%	O-wt%	O-at%	Nd-wt%	Nd-at%	Mn-wt%	Mn-at%
No Potential	25.5	47.8	18.9	28.1	0.6	0.1	55.0	24.0
Potential	18.4	40.3	17.6	35.7	5.2	1.1	66.8	40.2
*Potential	-	-	6.49	19.29	0.49	0.16	92.99	80.5

*Sub-surface analysis with potential application

However, EDS analysis is an analytical method of the surface of the samples without any subsurface information. To fully understand the possibility of Nd being intercalated into the MnO_2, the subsurface of the electrode was excavated using a FIB and the surface of the trench was analyzed with EDS as seen in Figure 3.6. Table 3.2 shows that the no Nd is been intercalated into the MnO_2 and that at this point all reaction taking place are occurring on the surface.

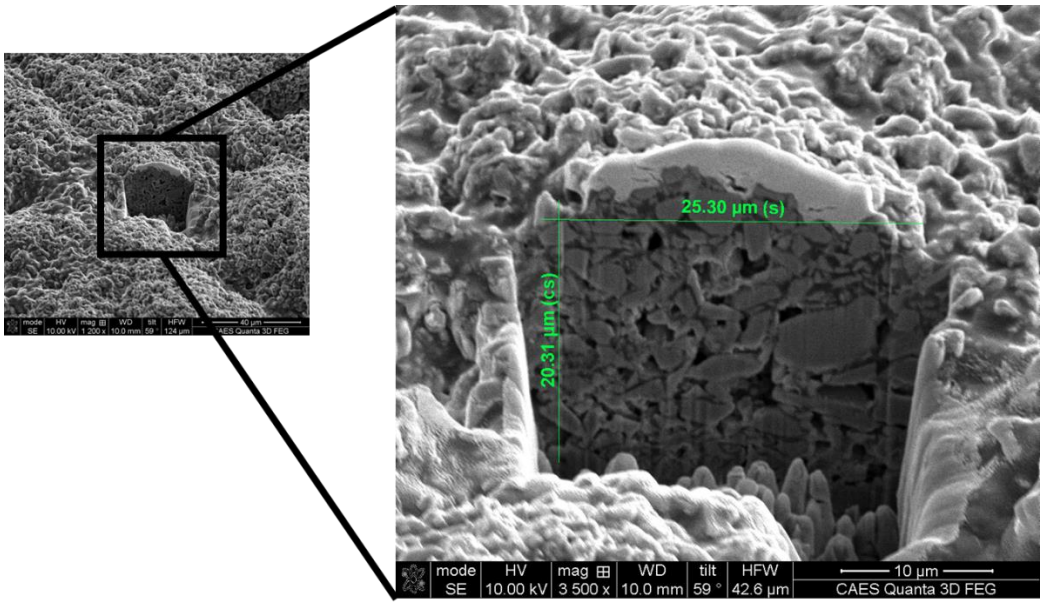

Figure 3.6. Excavated surface of MnO_2 electrode using FIB to enable analysis of subsurface MnO_2.

Bulk Electrolysis Experiments

Chronoamperometry Charge Experiments

Following studies on the effect of a potential driven experiment, three bulk experiments were run at different charges to improve the amount of Nd intercalated into the MnO_2 electrode. The potential applied was 0.5 V. From Table 3.3 it is observed that with increasing charge, the amount of Nd increases form 150 µg to 280 µg with approximately the same loading of MnO_2. Furthermore, the increase of Mn dissolution at higher charges is notable as shown in Figure 3.7 where significant electrolyte discoloration supports the losses of Mn reported in Table 3.3. This loss is significant compared to the amount of Nd immobilized. To put it into perspective, the loss of Mn is more than two and a half fold, and in some cases threefold more than the gain of Nd as seen in Table 3.3. The dissolution of Mn into the electrolyte through a disproportionation reaction according to Equation 6 is one of the drawbacks of employing Mn as an energy storage device. This dissolution leads to a decline in capacity and subsequently a decrease in the lifetime of the pseudocapacitor [237]–[239]. Furthermore, as charge increases, faradaic efficiency (FE) decreases. This decrease could also be a result of loss in Mn Up until this point the ability to intercalate Nd on/into the MnO_2 has been demonstrated but at low quantities. Issues such as the dissolution of Mn may play an effect. Furthermore, the method being used may be the limiting factor to the intercalation of Nd.

$$2Mn^{3+} \rightarrow Mn^{4+} + Mn^{2+}_{(aq)} \qquad [3.6]$$

Table 3.3. Concentration of Nd^{3+} in 0.9 cm^2 MnO_2 electrodes based on applied charge of 0.5 C, 1 C, and 2.17 C.

Charge (C)	Nd (mg)	MnO_2 Loading (mg)	Faradaic Efficiency %	Dissolution of Mn (mg)	Mn Loss: Nd Gained	%Mn Lost in Analyte
0.50	0.015	10.8	6.02	0.046	3.07	0.668
1.00	0.017	10.2	3.41	0.060	3.53	0.924
2.17	0.028	10.9	2.59	0.080	2.86	1.160

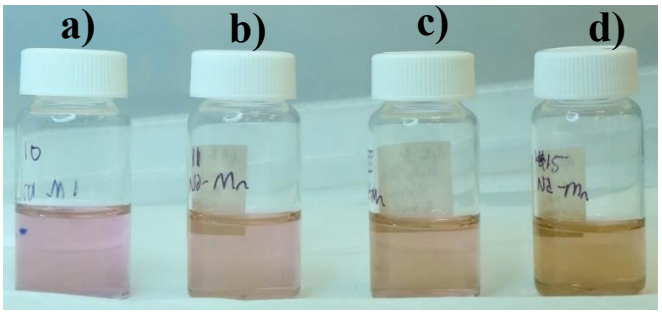

Figure 3.7**.** a) Pre-Experimental analyte, b) Analyte after passing 0.5 C, c) Analyte after passing 1 C , c) Analyte after passing 2.17 C

Up to this point, the amount of Nd extracted into the electrode has been very minimal. Suggesting that the reactions involving Nd intercalation is slow and takes time. Cycling the electrode through CVs between the oxidation and reduction potential was considered as an approach to possibly bolster the intercalation of Nd into the Mn electrode.

Effect of CVs prior to CA

To test the effect of CVs prior to running a CA, two electrodes were employed. One electrode was run without CVs prior to performing a CA. The second electrode was cycled between 0 V and 1.2 V vs. Ag/AgCl.. Prior to a CA. Table 3.4 indicates that while preforming CVs prior to a CA improves the capture of Nd by about twice the amount from 9.1 x 10^{-2} mg to 1.59 x 10^{-1} mg, this may not be the best route to increase Nd yield. Furthermore, an increase in FE from 9.13% to 16.0% in also observed when the cell is cycled.

Table 3.4. Comparison between cycling and noncycling of an electrode prior to CA tests. Area of electrodes for both experiments were 4cm^2 and Charge applies to both electrodes is 2C.

Concentration of $NdCl_3$	Charge (C)	Type of Experiment	MnO_2 (mg)	MnO_2 (mg/cm^2)	Nd (mg)	Nd (mg/cm^2)	Faradaic Efficiency (%)
1 M	2	Cycle	52.9	13.2	0.159	0.040	16.0
1 M	2	No-Cycle	50.5	12.6	0.091	0.023	9.13

While the mechanism for surface absorption works, treating the electrode as a capacitor is not sufficient to permit the intercalation of Nd^{3+} or increase the amount of Nd on the surface of the electrode. Factors affecting, the diffusion of Nd^{3+} into the MnO_2 electrode could be as a result of incomplete activation of the MnO_2 or the effect of Mn dissolution during CA. Studies have shown that the addition of a Mn^{2+} additive to the electrolyte helps promote stability, and coulombic of the electrode during cycling [191], [240]–[242]. Zhang et al. demonstrated the rechargeability of a zinc-manganese dioxide battery using aqueous zinc triflate as electrolyte $Mn(CF_3SO_3)_2$, MnO_2 as the cathode, Zn as anode and $Mn(CF_3SO_3)_2$ as additive. They observe a stark increase in charge and discharge during the cycling of the battery. Furthermore, they attributed the stability of the β-MnO_2 due to the Mn additive which suppresses the dissolution of Mn^{3+} to Mn^{2+} through disproportionation. They observed the successful intercalation of Zn^{2+}, and the increase in columbic efficiency compared to other conventional cation batteries like Na, K, and Li, and partly attribute this to the addition of the Mn additive of 0.1 M, which compensate for the dissolution Mn [191]. However, the capacity reported by Zhang et al. [191], though high, may be skewed by the presence of the Mn^{2+} acting as an addition reactive species. Wu et al [243]observed that by including Mn^{2+} as an additive, Mn is

intercalated simultaneously with Zn^{2+}. They corroborated this by observing an increase in electrode capacity with an increase in Mn additive from 0 to 100 mM.

Cycling our electrochemical cell similar to a battery requires chronopotentiometry experiments at current values based on the theoretical capacity of the host metal. To test the viability of the electrode as a pseudo battery, the electrode was tested in $ZnSO_2$, $ZnSO_2$ with $MnSO_2$ additive, and $NdCl_3$. Each experiment was run at C/40 (theoretical capacity of host electrode divided by 40) and cycled to overcome the activation phase of the MnO_2. Cycling included running chronopotentiometry tests at -0.247 mA (intercalating), and 0.247 mA (deintercalating) respectively for at least 2 cycles. Each cycle lasted at least three hours. Figure 3.8 shows the various capacities for the test electrodes. Both the Zn and Zn with Mn additive were run for the full cycle. The Electrode with the 1 M $NdCl_3$ electrolyte was stopped halfway during the third cycle with prior two cycles run for at least 3 hours. The capacity of Zn plus Mn additive electrode had the highest capacity than just the Zn electrolyte.

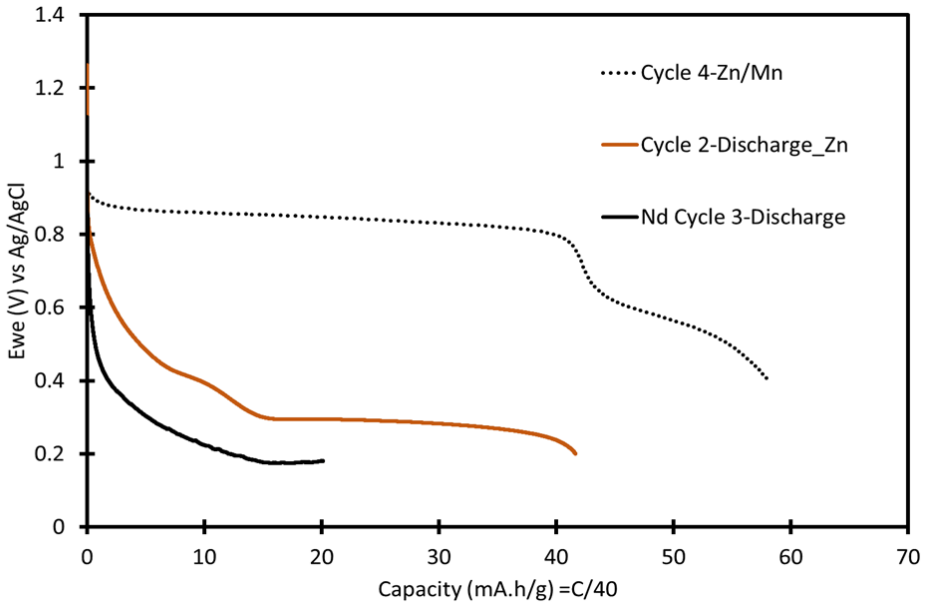

Figure 3.8. Discharge curves for MnO_2 in various electrolytes showing different capacities

Further probing with EDS analysis, Figure 3.9 shows that in the Zn^{2+} only electrolyte, the presence of Zn^{2+} on the electrode is substantially greater than with the Zn^{2+} and Mn additive electrolyte. Thus, corroborating the studies done by Wu et al [243]. Suggesting that the additive contributes to the capacity of the electrode and is part of the reaction species as seen in Figure 3.9b. Further investigation into the electrode in the $NdCl_3$ shows that treating the electrolyte as a battery by capacitive current cycling increases the Nd^{3+} content in the electrode by more than 10 wt% as seen in Figure 3.9c. Furthermore, probing the subsurface of the electrode using FIB analysis shows that Nd^{3+}

is intercalated and diffuses into the electrode as seen in Figure 3.10. These prior experiments show that capacitive current cycling encourages the intercalation process and that the reactions governing the intercalation of Nd^{3+} into the MnO_2 electrode are first surface reaction followed by diffusion into the electrode to promote intercalation.

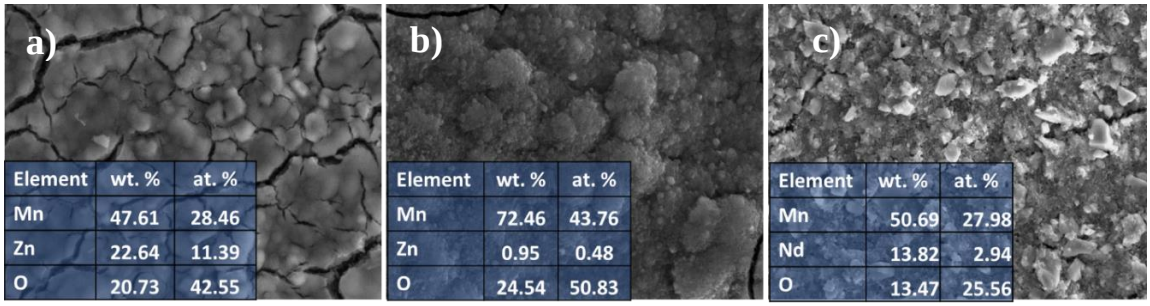

Figure 3.9. a) 1 M $ZnSO_2$, b) 1 M $ZnSO_2$ and 0.1 M Mn additive, and c) 1 M $NdCl_3$ and 0.1 M Mn . These are average values of four analyzed spots. For Nd some values as high as 19 wt. % and 4.45 at. % were observed.

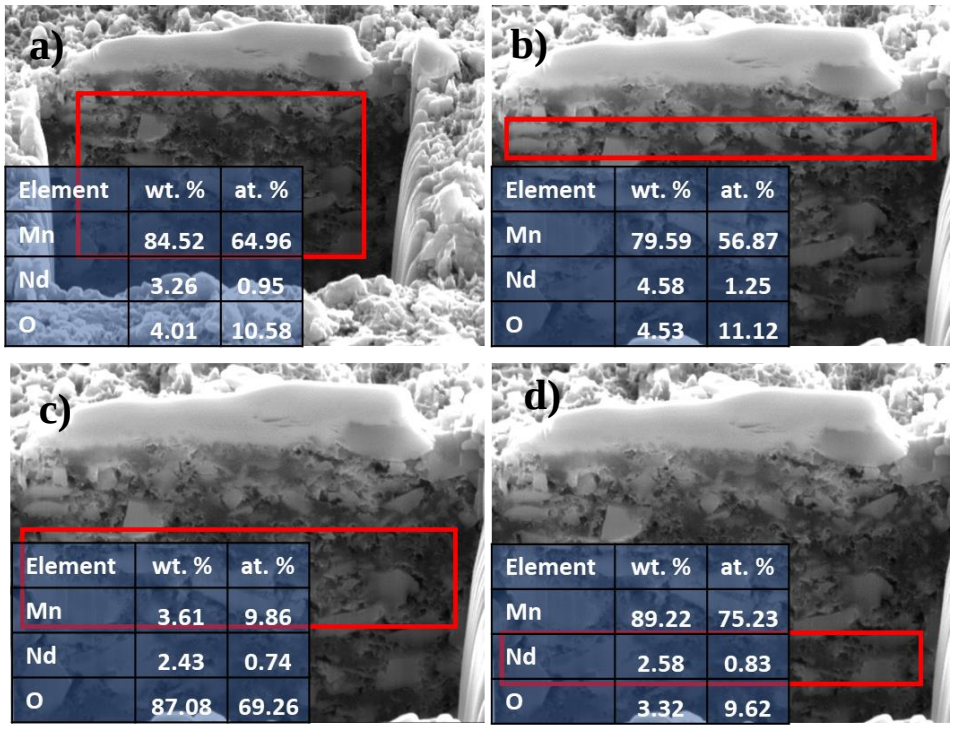

Figure 3.10. Sub-Surface Analysis for Nd. a) Average values for Nd below subsurface b) right below surface c) mid-section, d) further below the surface

Up to this point the immobilization of Nd^{3+} into an MnO_2 electrode has been proven. However, optimizing the capacitive cycling current is of necessity to enhance and improve the immobilization of Nd^{3+}.

Selecting an Optimal Capacity Rate to Enhance Nd^{3+} Immobilization

Various capacitive rate experiments were conducted from C/5 to C/40 to determine an appropriate C rate to run bulk experiments. Parameters of interest were the dissolution of Mn during the experiment, the reaction time for conditioning of the MnO_2 prior to immobilization of Nd^{3+}, and the amount of Nd^{3+} intercalated into the MnO_2. All capacity experiments were stopped at 1.890 mA.h to allow for adequate comparison. This value was obtained by running the fastest capacity rate; C/5 and observing where the cutoff concentration polarization occurred. Subsequent experiments were then run up to this value following conditioning of MnO_2 as seen in Table 3.5.

Table 3.5. MnO_2 cycled at various capacity rates.

Capacity rate	Limiting Capacity (mA.h)	Stop Time for conditioning cycle	Hours to Conditioning	Days to Conditioning
C/5	1.89	57.5 mins	15	0.63
C/10	1.89	1 hr 55 mins	20	0.83
C/20	1.89	3 hrs 50 mins	44	1.83
C/40	1.89	7 hrs 40 mins	88	3.67

The cycling time for each charge and discharge cycle was selected based on the time needed to reach a capacity rate of 1.89 mAh. Conditioning of MnO_2 occurred when the discharge curves deviated from a flat initial plateau to a slanted plateau to more negative potentials than the initial discharge curve. The cell was cycled until conditioning was achieved. As seen in Table 3.5, the conditioning of MnO_2 at different capacity rates occurs as the different cycle and different times. A complete view of all cycles can be seen in Figure 3.11. With a cycle time of 3 hours for both the charge and discharge, conditioning of the MnO_2 at C/5 take 15 hours. At the C/10 and with a cycling time of 4 hours, conditioning takes 20 hours, and 44 hours for C/20. However, the conditioning time for C/40 is much longer and takes 88 hours with a cycling time of 8 hours per cycle.

The insert in Figure 3.12 shows that the C/20 and C/40 are very similar in features despite the wide gaps in conditioning time. Suggesting that between the two capacity rates, C/20 is optimal, with lower duration time. Figure 3.12 also shows two plateaus at C/10. Suggesting an initial intercalation process (first plateau) followed by a second plateau govern by the possible intercalation of Nd. Sun et al. in investigating Zn^{2+} intercalation into Mn observed that the first plateau is the intercalation of H^+ simultaneously with Zn^{2+}. However, during the second plateau, they observed that Zn^{2+} intercalation is more dominant [244]. Suggesting that the second plateau in C/10 could be Nd^{3+} dominating. Only one dominant plateau can be seen during C/5 before the concentration polarization occurs at 1.89

mA.h. Comparable to C/10, the reaction and conditioning of MnO_2 occurs at a much faster rate and may involve the simultaneous immobilization of H^+ and Nd^{3+}, leaving no distinction in the capacity plot. Another possibility could be that due to a faster reaction rate and leaving no time to condition the MnO_2 to allow intercalation of Nd^{3+}, surface adsorption on the Nd^{3+} is more dominant than intercalation of Nd^{3+}. Hence, a much quicker concentration polarization.

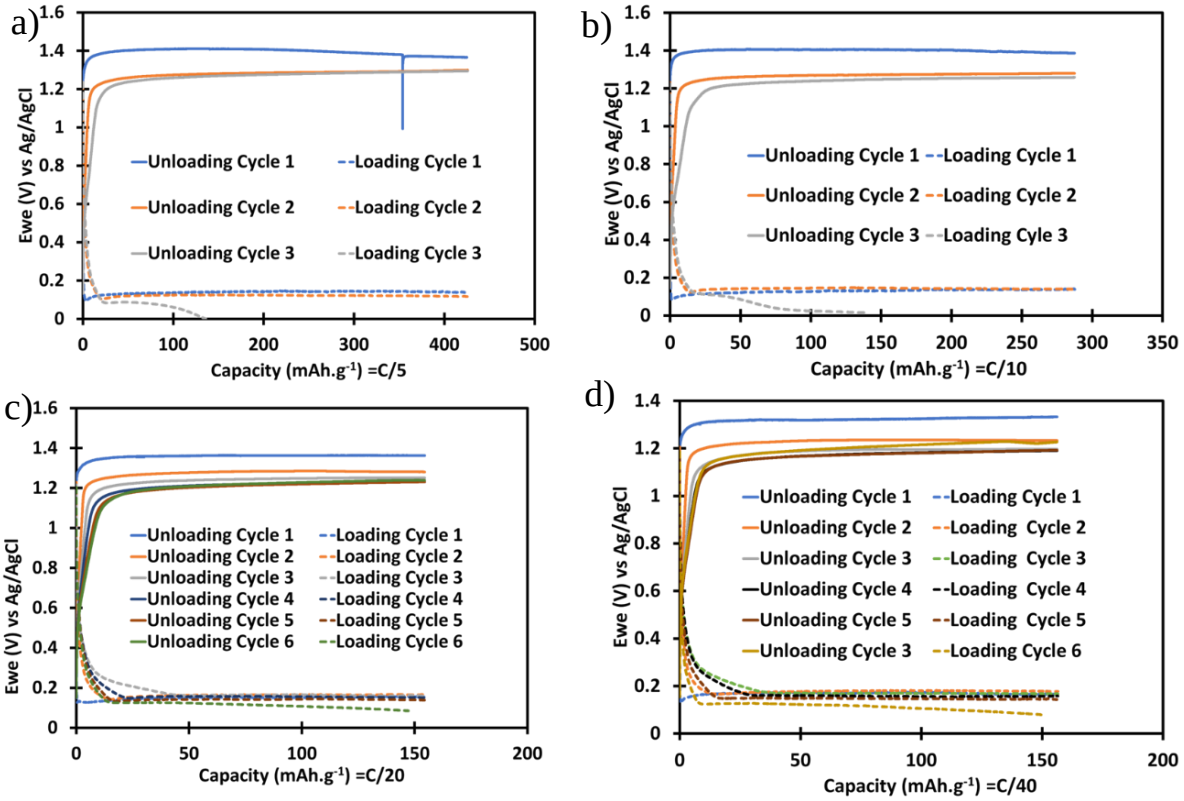

Figure 3.11. Different capacitive cycles for MnO_2 a) C/5, b) C/10, c) C/20, d) C/40

From Table 3.6, ICP-MS analysis shows that the C/40 shows the highest dissolution of Mn per charge with the lowest at C/5 followed by C/20. Furthermore, C/20 showed the most intercalation of Nd^{3+} and the most optimal in activation time and dissolution of MnO_2. This conclusion is based on the following factors. Whereas C/5 shows the second highest intercalation of Nd, the amount of charge needed to reach 2.682 mg of Nd intercalated is 113.2 C compared to 84.9 for C/20.

Secondly the faster rate of C/5 having a much earlier polarization could be that C/5 does not favor intercalation but is governed by surface accumulation of Nd^{3+} leading to an exhaustion of reaction sites. Hence a quicker concentration polarization.

Furthermore, C/40 has been shown in prior experiments to foster the intercalation of Nd^{3+}. Figure 12 also showed that C/40 and C/20 are similar. Also, C/20 has the highest faradic efficiency and the

second lowest dissolution rate for Mn when the Mn is activated. To minimize the dissolution rate of Mn whiles permitting the intercalation of Nd^{3+}, C/20 was chosen for further studies in non-aqueous media. Hence to take a much safer route and avoid the quick dissolution of Mn as well as permit the intercalation of Nd, C/20 was chosen.

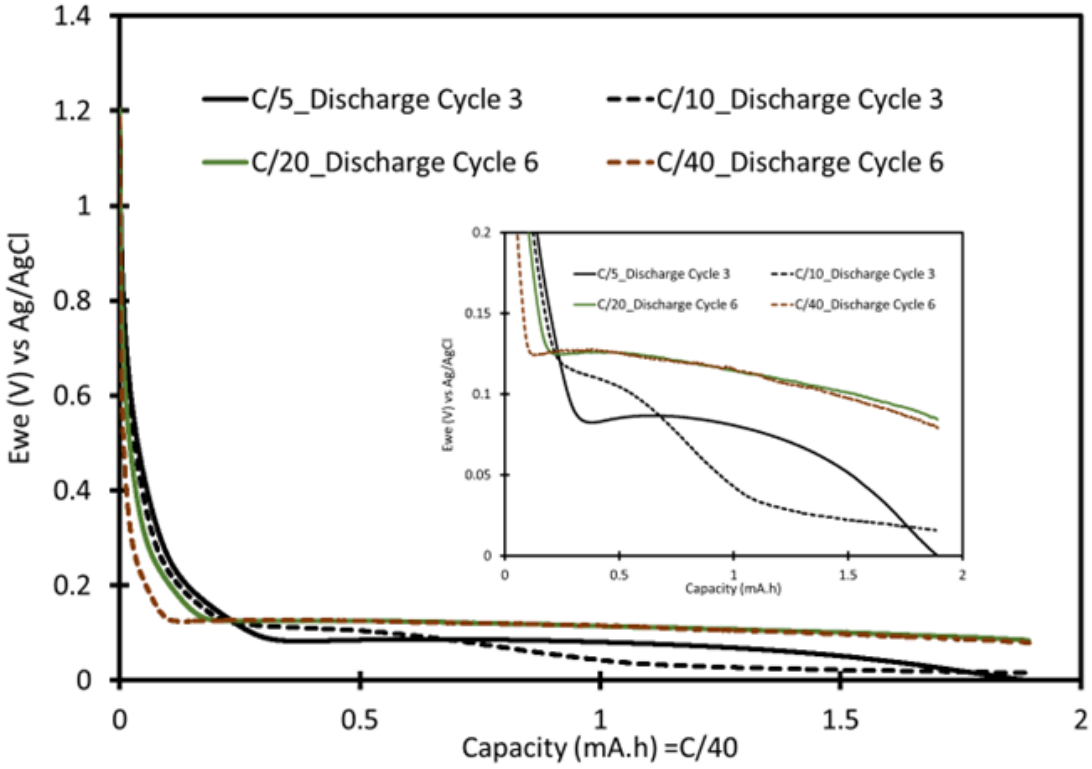

Figure 3.12. Various capacitive discharge curves for MnO_2 in 1 M $NdCl_3$.

Table 3.6. ICP-MS analysis of various electrolytes run a various capacity rate to determine amount of Nd captures and dissolution rate of Mn.

Capacity	Loading of MnO_2/cm^2	Applied Charge (C)	Total Nd Immobilized (mg)	Mn Dissolved in Solution (mg)	Mn Loss: Nd Gained	*Faradaic Efficiency (%)	% of Mn Lost	Dissolution of Mn (ug)/ C	Hours to Activation
C/5	3.49	113	2.68	0.148	0.055	79.1	1.70	1.30	15
C/10	3.43	77.8	2.17	0.389	0.179	64.1	4.50	5.00	20
C/20	3.19	84.9	3.55	0.222	0.063	105	2.80	2.62	44
C/40	3.16	85.1	1.06	0.547	0.514	31.4	6.90	6.43	88

*FE calculated based on 1.89mAh

Testing On MnO_2 Electrode in Ionic Liquid

Following immobilization of Nd in a 4cm^2 MnO_2 electrode at -0.493 mA, the electrode was introduced in 1-butyl-1-methylpyrrolidinium triflate ionic liquid. The unloading potential applied was 0.493 mA. The duration of the experiment was 8 hours The RE and CE, were a Pt wire and Pt electrode respectively. A set up of the experiment can be seen in Figure 3.13.

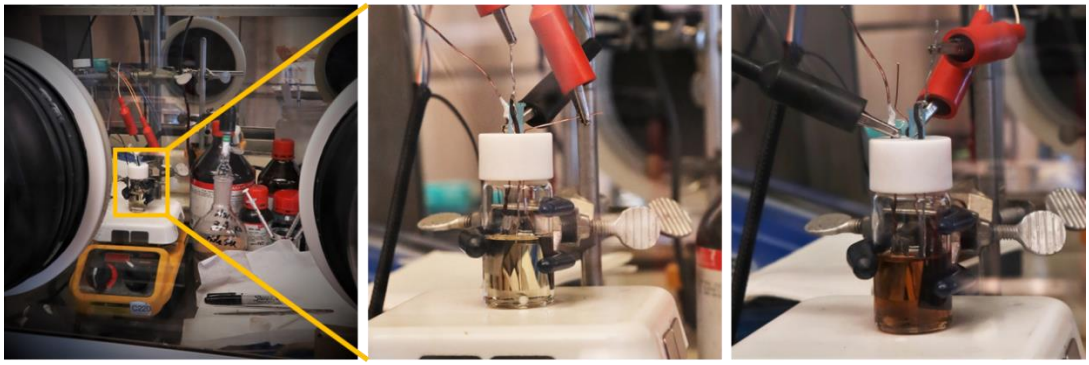

Figure 3.13. Deintercalation setup for MnO_2 Nd intercalated electrode in 1-Butyl-1-methylpyrrolidinium Trifluoromethanesulfonate.

Figure 3.14a and b are in the unloading and loading curves for the MnO_2 electrodes in 1 M $NdCl_3$ and 1-Butyl-1-methylpyrrolidinium trifluoromethanesulfonate respectively.

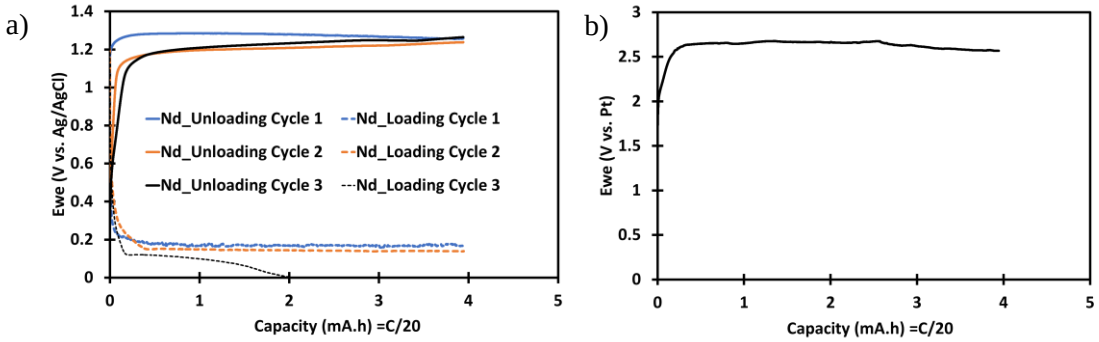

Figure 3.14. a) loading and unloading curves for MnO_2 electrode in 1 M $NdCl_3$. b) deintercalation curves for MnO_2 intercalated Nd electrode in 1-Butyl-1-methylpyrrolidinium Trifluoromethanesulfonate.

Table 3.7 shows that after applying a current of 0.493 mA for 8 hours, only 8.65% of the total mass of Nd, which was 3.32 mg intercalated into the electrode was unloadd. Furthermore, the amount of Mn in the ionic liquid, is very negligible showing that Mn is stable in the ionic liquid. Calculating the Faradaic efficiency of the deintercalation process yields 4.0 %. While this value is low, it shows that with a longer deintercalation duration, more Nd^{3+} can be unloaded from the electrode. However, for a practical application, less deintercalation time will be favorable.

Table 3.7. Amount of Nd^{3+} unloaded during deintercalation in 1-Butyl-1-methylpyrrolidinium Trifluoromethanesulfonate.

Duration (hrs.)	Capacitive Current (mA) C/20	Total Mass of Nd^{3+} Intercalated (mg)	MnO_2 Loading (mg)	FE for Loading (%)	Mass of Nd Unload in IL (mg)	Mass of Nd in Electrode (mg)	Mass of Mn in IL (mg)	FE Unload in IL (%)
8	0.493	3.32	13.2	92.5	0.287	3.03	0.0204	4.0

Conclusion

The immobilization of Nd^{3+} was studied using a MnO_2 electrode at different capacity rates. Cyclic voltammetry plots display capacitive and diffusion behavior. Suggesting that Nd capture is both adsorption and intercalation. In the presence of Nd current is enhanced, and redox peaks are more prominent. The cycling rate of C/20 was optimal with less dissolution of Nd. The MnO_2 electrode displayed high FE values for Nd^{3+} capture in aqueous solution. Unload in IL was proven but a more positive current or longer electrolysis duration may be required to enable substantial unload of Nd. The limiting factor of using MnO_2 as an electrode is the less stability is aqueous solution due to dissolution. The optimal electrode for intercalation must be stable in both aqueous and ionic solutions. This characteristic is crucial to reuse. Furthermore, most of the bulk storage of MnO_2 takes place at the surface and involves only a thin layer. Thus, there is a limit to how much material can be used in producing the electrode. While MnO_2 showed promise in Nd^{3+} intercalation in REE aqueous solution, dissolution in the electrolyte and a limited amount of Mn makes it a less ideal candidate.

Chapter 4: Faradaic Immobilization and Unloading of Trivalent Rare Earth Elements in a Disordered Graphitic Electrode

Introduction

The pursuit of materials with fast charging and discharging capabilities continues to be an area of keen interest in the field of energy storage. This has made pseudocapacitors very popular among energy storage researchers. Pseudocapacitors (PCs) are materials whose charge storage is driven by surface faradaic redox reactions but include some sort of battery-like intercalation [232], [234], [245]–[252]. Compared to traditional batteries, charging, and discharging of PCs happens in minutes and sometimes in seconds. Hence their rising popularity in the field of energy storage [235], [253]–[255]. The most common examples of PCs are RuO_2, MnO_2, transition metals oxides and hydroxides, and MXenes [232], [234], [249], [252]. In the field of energy storage, PCs have been employed for the immobilization of metal ions such as Li [256]–[258], Na [259]–[261], and K [262]–[264], and have shown superb capacitance ranging from 200 F g^{-1} to >2000 F g^{-1} [233]. Such high capacity and fast cycling present opportunities for other beneficial applications such as low temperature rare earth elements (REEs) recycling and immobilization. To date, no known study has employed the use of pseudocapacitors for the immobilization of REE ions.

REEs such as neodymium (Nd) have not been widely studied for near room temperature aqueous electrochemical intercalation into graphitic materials. However, high temperature methods have been employed as intercalation mechanism for REEs into graphite to create graphite intercalated compounds (GICs) with better electrical conductivity [265], [266] and as a method to develop alternatives to the amalgam-reduction method for REE separation[267]. Furthermore, Vickey and Campbell observed that heavy REEs (i.e. Gd, Y, Yb, Lu) were intercalated into the graphite defects and not the graphite interlayer spacing [267]. While graphite has been a popular host material for intercalated species, it is inadequate for the immobilization of REEs due to smaller interlayer spacing [261], [268], [269]. The challenge of storing ions larger than Li has prompted researchers to explore materials with larger interlayer spacings and abundance of defects [268].

The rich presence of defects, disordered planes, and large pore sizes make turbostratic carbons (TCs), containing a mixture of sp^2 and sp^3 hybridized carbon [270]–[273], such as soft and hard carbons ideal candidates for large ion storage [169], [274] [275]. Also, these materials have high surface area, high stability, and long-term performance making them even more lucrative as charge storage devices [276]–[280]. While no known research has focused on REE storage with TCs, various researchers have aimed at elucidating the storage mechanisms of TCs involving Na^+ ions [261], [277], [281],

[282]. Cheng et al. observed that the charge storage mechanism of Na in hard carbon is partially intercalation, and defect adsorption [261]. Other researchers have likewise explored this area thoroughly and have arrived at the same conclusion [277], [281], [282]. Furthermore, not only Na^+ but Li^+ and K^+ among many other cations have also been studied for intercalation into various TCs materials as energy storage applications [175]–[177], [185], [188].

Promising applications for studying the storage of REEs in TCs at near room temperature in aqueous solution involve energy storage, capture and separation of REEs from diluted streams, or as a media to connect aqueous with non-aqueous electrochemical systems. This last concept would employ the use of TC intercalated with REEs as a feeder anode to unload REEs into non-aqueous electrolytes for further reduction into REE metals [142]–[144]. We herein study the electrochemical immobilization of Nd into a TC (Vulcan XC-72R) in aqueous media and the subsequent unload into non-aqueous electrolytes.

Experimental

Electrode Preparation

Carbon paste slurries were made from 80 wt.% Carbon powder (Carbon Black - Vulcan XC 72R), 20 wt.% polyvinylidene fluoride, and N-methyl-2-pyrrolidone (NMP) as solvent. The solvent to powder ratio was 2:1. Slurries were painted on 4 cm^2 carbon paper (Toray Teflon Treated Carbon Paper- 060 - TGP-H-060) substrates. The mass loading of the electrode was 32 mg carbon. Electrodes were dried at room temperature. The carbon powder and substrates were purchased from FUELCELL Store and the NMP was purchased from Sigma Aldrich.

Electrolyte Configuration

Aqueous and ionic liquid (IL) electrolytes were employed for electrolysis. Aqueous electrolytes were 250 mM $NdCl_3$ and 1 M KCl in DI water. IL electrolytes were prepared by adding the following salts to Acetonitrile (CH_3CN or MeCN) to make ca. 300 mM of solution:

- 1-Butyl-1-methylpyrrolidinium Bis(trifluoromethanesulfonyl)imide ($C_{11}H_{20}F_6N_2O_4S_2$)
- Tetrabutylphosphonium chloride (TBPCL)
- trihexyl(tetradecyl)phosphonium bis(trifluoromethanesulfonyl) amide CYPHOSIL 109
- 1-Butyl-3-methylimidazolium triflate from Ionic Liquids Technology (io-li-tec)

All electrolytes were agitated until homogeneity between salt and solvent was achieved. All other ILs were purchased from Sigma Aldrich.

Electrochemical experiments

The electrochemical experiments were conducted in a three-electrode cell as shown in Figure 4.1. The working electrode was the carbon electrode. The auxiliary electrode was Pt. Potentials were measured and reported versus an Ag/AgCl (3 M NaCl) (BASi) or a Pt wire reference electrode during electrolysis in aqueous and IL electrolytes respectively. A BioLogic SP-50 potentiostat controlled by EC-Lab software was used to perform electrochemical experiments. IR compensation was applied to CV curves and bulk experiments.

Electrochemical techniques of cyclic voltammetry (CV) and chronopotentiometry (CP) were conducted to elucidate the storage mechanism of Nd^{3+} in the carbon electrode. A cathodic current was employed during CP experiments for loading the REEs into the carbon electrode and an anodic current was employed for unloading the REEs from the electrode. Thus, the carbon electrode was alternatively the cathode or the anode depending on the electrochemical experiment taking place.

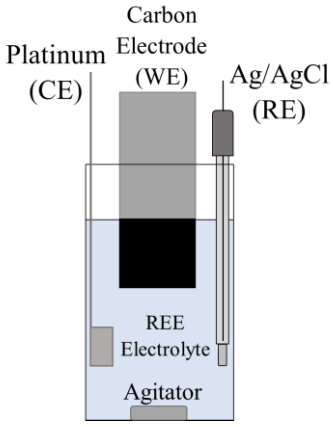

Figure 4.1 Electrochemical setup for cyclic voltammetry and bulk electrolysis experiment. Agitator was absent during CV experiments.

Analysis and characterization methods

Following CP immobilization of Nd^{3+} from $NdCl_3$ electrolyte, the carbon electrodes were washed with copious amounts of DI water, dried, and introduced to 1 M KCl or an IL to electrochemically unload immobilized Nd^{3+}. After electrochemical unload, the electrodes were treated with 3:1 HCl-HNO_3 (aqua regia) to quantify remaining Nd^{3+} in the electrode. The concentration of Nd unloadd in the KCl or IL, as well as the HCl-HNO_3 leachate was measured using an iCAP Q inductively coupled plasma mass spectrometer (ICP-MS) from Thermo Scientific. SEM and EDS analysis were employed to study elemental composition, and surface morphology. A JEOL JSM-6610LV and EDAX AMETEK Apollo X controlled by EDAX software was employed for SEM and EDS studies. FIB analysis was employed to investigate the subsurface of the carbon electrode. XRD analysis was

conducted to investigate structural makeup and possible changes to the carbon electrode prior to, and after REE immobilization using a Bruker D8 Advance Diffraction System (Cu Kα radiation, λ = 1.54056 Å).

Results and Discussion

Baseline Definition for Nd Immobilization

A baseline was established to validate the faradaic immobilization of Nd into the carbon electrode. To establish the baseline, a 4 cm^2 electrode with a carbon loading of 32 mg was immersed overnight in 250 mM $NdCl_3$ in the absence of any applied current density. After immersion, the electrode was rinsed thoroughly with DI water and dried overnight at 120 °C for EDS analysis. Following EDS analysis, the electrode was digested in aqua regia for further characterization.

EDS analysis in Figure 4.2 shows that close to 2.0 wt.% and 6 wt.% of Nd^{3+} is present on the surface and subsurface of the carbon electrode respectively following the baseline test. ICP-MS analysis reveals that these values correspond to a total Nd mass of 0.0813 mg which can be attributed to surface adsorption. Therefore, for electrochemical immobilization any quantity beyond this value can be safely assigned to the electrochemical process.

a)

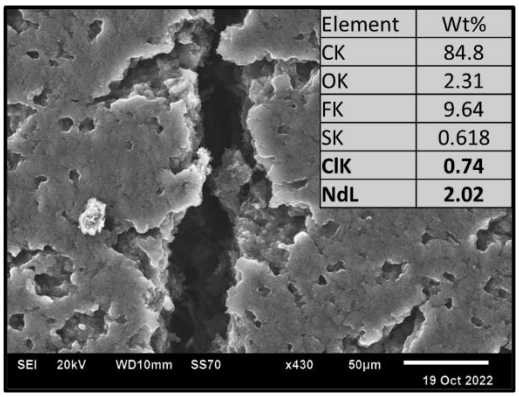

b)

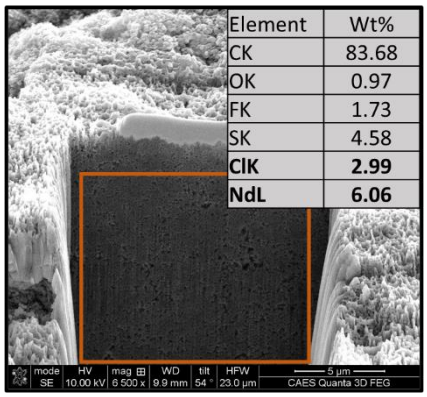

Figure 4.2 SEM images and EDS analysis of a) surface and b) subsurface of a blank carbon electrode immersed in 1M $NdCl_3$

Electrochemical Experiments

Cyclic Voltammetry (CV) and Specific Capacity (SC) in Aqueous Nd Electrolyte

The electrochemical behavior of the carbon electrode was studied within the potential window of -0.3 V to 0.5 V vs Ag/AgCl. Scan rates ranging from 1 mV/s to 100 mV/s were employed for CV studies. The electrolyte composition was 250 mM $NdCl_3$. The CV sweeps in Figure 4.3a illustrates the classic potential current response of a pseudocapacitive electrode [283]. At lower scan rates a broad

reduction peak observed between 0 and -0.1 V vs Ag/AgCl is more pronounced. The presence of the broad peak is further indicative of a pseudocapacitive electrode and could suggest slow diffusion of species into the layers carbon electrode [232]–[234]. Furthermore, prompt current density increase upon voltage reversal at cathodic and anodic switch potentials suggest expeditious chemisorption and desorption of the Nd^{3+} ions at the surface of the electrode [235] [284]. These observations are in tandem with the proposed charge storage mechanisms of pseudocapacitors where charge is stored through a combination of surface redox pseudocapacitance, or intercalation pseudocapacitance [248], [249], [285]. Furthermore, as the scan rate decreases, the specific capacity of the carbon electrode increases as shown in Figure 4.3b. Suggesting that at slower electrolysis, times the storage of Nd is increased. Compared to literature, these capacity values were found similar, and in some cases higher, that those reported for Vulcan XC 72R and Vulcan XC 72 as seen in Table 4.1.

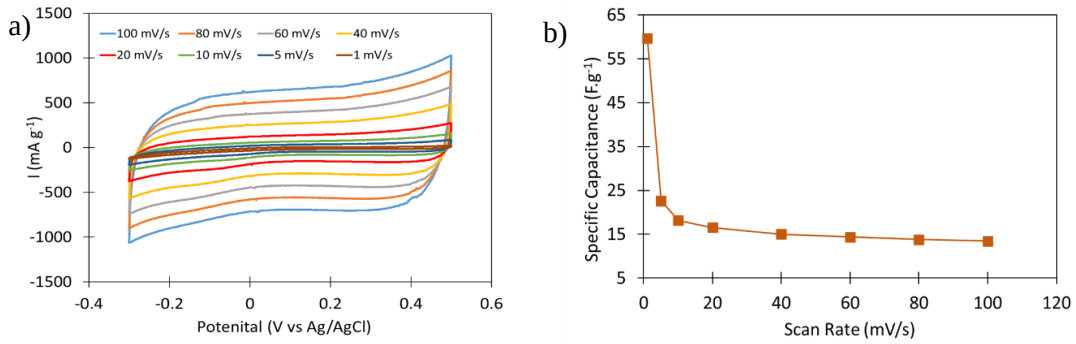

Figure 4.3 a) Cyclic voltammetry of 32 mg carbon electrode in 250 mM aqueous $NdCl_3$ electrolyte. b) specific capacity of 8 $mg.cm^{-2}$ carbon electrode in 250 mM aqueous $NdCl_3$ electrolyte.

Table 4.1 Specific capacity of various configuration of Vulcan compared to electrode used in this work.

Electrode Material	Electrolyte	Scan Rate (mV/s)	C ($F\ g^{-1}$)	Potential Window (V)	Reference
Vulcan XC-72R	0.1M $NaHCO_3$	50	5	0.3 to 0.8 V vs. RHE	[286]
Vulcan – (HNO_3-H_2SO_4)	0.1M $NaHCO_3$	50	30	0.3 to 0.8 V vs. RHE	[286]
Vulcan XC-72R – (HNO_3)	0.1M $NaHCO_3$	50	36	0.3 to 0.8 V vs. RHE	[286]
Vulcan XC-72R – (HNO_3)	0.1M $NaHCO_3$	50	42	0.3 to 0.8 V vs. RHE	[286]
Vulcan XC-72	0.1 M K_2SO_4	50	15.5	-1.0 to – 0.3 V vs. SHE	[287]
Vulcan XC-72	-	5	18	-0.5 to 0.5 V vs Ag/AgCl	[288]
Carbon Black	-	5	65	-0.5 to 0.5 V vs Ag/AgCl	[288]
Vulcan XC-72R	**0.25 M $NdCl_3$**	**5/60**	**22.7/14.4**	**0 to 1 V vs. Ag/AgCl**	**This Work**

Investigating Storage Capacity of the Carbon electrode

Adequate and efficient immobilization of Nd^{3+} into the carbon electrode requires an understanding of the storage capacity of the carbon electrode in the presence of Nd. While this is not known for Vulcan XC-72R, a careful stepwise approach can be employed to get an idea of this value. From the CV scans at different scan rates, it was observed that the slowest scan rate yielded the highest specific capacitance. Likewise, a much smaller current density application will yield a storage capacity closer to the true value of the electrode [289], [290]. To investigate this, a cathodic current of density 18.75 mA g^{-1} based on the carbon loading (32 mg) was chosen to run Nd loading over a 24-hour period. The electrolyte was 1 M $NdCl_3$. The cutoff potential was 0 V vs Ag/AgCl. After approximately 19 hours of electrolysis the experiment reached the cutoff potential with corresponding storage capacity of 11.41 mAh or 356.9 mAh.g^{-1} and a charge density of 1284 C g^{-1}. Various electrolysis duration can be investigated and designed based on this value to optimize Nd immobilization. For practical application, a shorter run time at an applied current density that does not compromise electrode integrity is desired.

Optimizing Electrolysis Duration

Based on the charge density of 1284 C g^{-1}, 2-, 4- and 6-hour experiments, corresponding to applied current densities of 178 mA.g^{-1}, 89.1 mA.g^{-1}, and 59.4 mA.g^{-1}, respectively were investigated. The employed electrolyte was 11 mL of 250 mM $NdCl_3$. Following electrolysis, visual inspection of the electrode surface after washing and air drying displayed a pastel purple precipitate on the electrode run for 2 hours as seen in Figure 4.4a. However, no visible precipitate is observed for electrodes run for 4 and 6 hours runs as seen in Figure 4.4b and 4c.

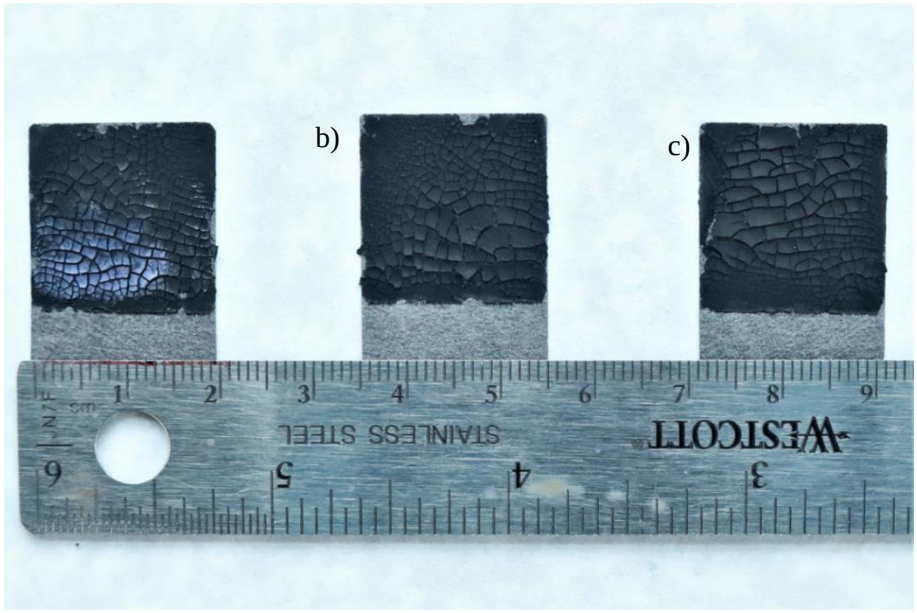

Figure 4.4 a) Pastel purple precipitate on the surface of all electrodes after 2 hours of electrolysis at -5.71 mA. b) and c) visual absence of pastel precipitate on electrode following 4 and 6 hours of electrolysis at -2.85 mA and -1.90 mA respectively.

Noteworthy is that a higher applied current density is employed at 2 hours. This results in stronger polarization of the cathode, capable of leading to hydrogen evolution reaction (HER) at the surface of the electrode. As a result, dissociated OH^- ions can interact with the Nd^{3+} to form $Nd(OH)_3$. A similar observation was made by Medina et al, where HER at the surface of the cathode was used to concentrate La from solution in the form of $La(OH)_3$ [291].

EDS analysis of the various electrodes as seen in Table 4.2 and visually represented in Figure 4.5 show that the ratio of oxygen to Nd of the 2-hour electrode strongly support the formation of $Nd(OH)_3$. While this is a mechanism for immobilization of Nd^{3+}, the end product of $Nd(OH)_3$ is not preferred. Thus, making 2 hours an unideal electrolysis time for Nd^{3+} immobilization. Comparing the EDS values of 4 and 6 hours shows that 4 hours is an optimal time with a better ratio of carbon and chlorine to Nd than 6 hours.

Table 4.2 Various elemental ratios to Nd of EDS measurements

Time (Hr.)	O:Nd	C:Nd	Cl:Nd
2	3.81	34	0.506
4	1.22	64	0.420
6	1.8	100	0.482

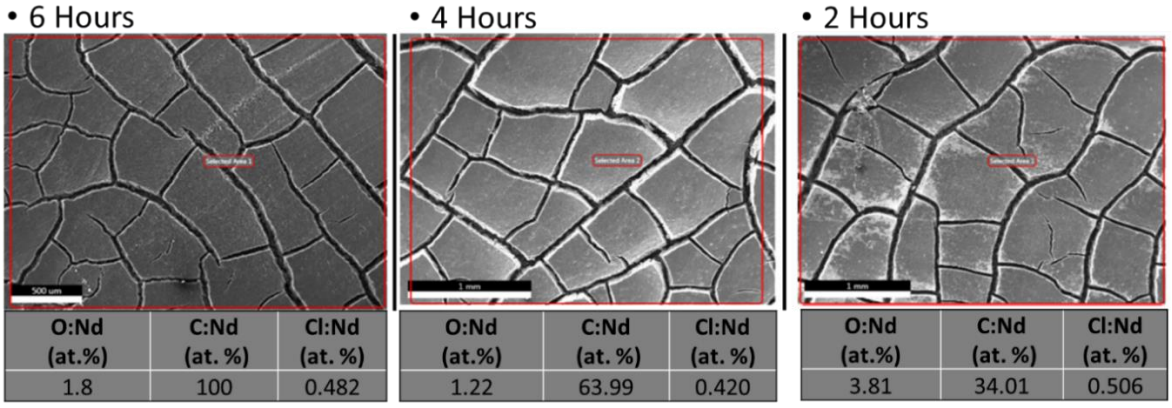

Figure 4.5 EDS analysis of similar electrode subject to an electrolysis time of 6, 4 and 2 hours showing various elemental ratios with Nd.

Like capacity vs. potential curves, the features of a time vs. potential curve can shed light on the type of storge mechanism occurring in TCs. Slopes may represent intercalation between layers, and

plateaus may represent storage between nano-pores. In studying the immobilization of Na^+ into hard carbon, researchers attributed the sloping region of the time vs. potential curve to the intercalation of Na^{3+} between the layers of the carbon electrode. They further attribute the plateau region to the adsorption of Na^+ within defects such as pores [261], [278]. Bai et al. also demonstrated that Na ions fill the pores during the plateau region by prefiling the pores of carbon electrode with sulfur prior to Na electrolysis. Due to the presence of sulfur, Na^+ ions were not incorporated into the carbon electrode pores, and consequently the plateau region disappeared [282]. These observations along with other studies can be used as a guide in hypothesizing the mechanisms associated with Nd^{3+} storage in this study [276], [277], [292], [293]. Figure 4.6 displays identical time curves for 2 and 4 hours of electrolysis. Suggesting an identical capture mechanism for 2 and 4 hours with the absence of HER at 4 hours. Based on the above studies with Na, the plateau region observed in Figure 4.6 can be attributed somewhat to the storage of Nd within the pores of the carbon electrode.

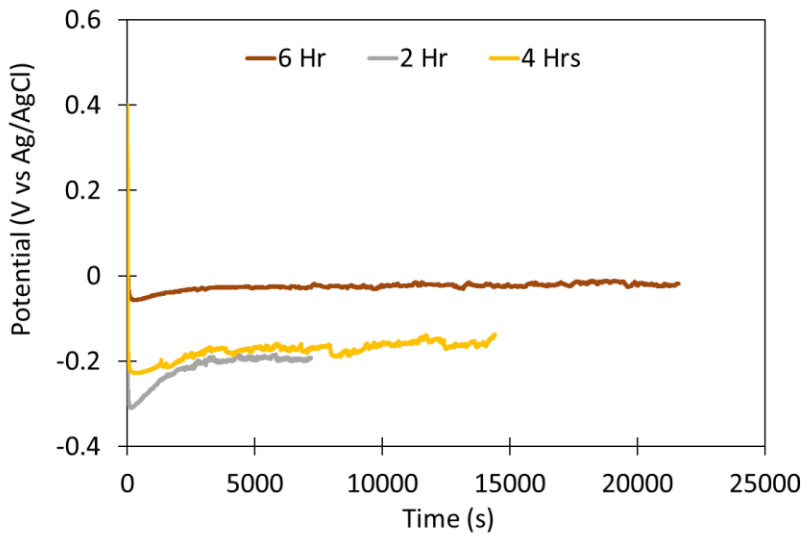

Figure 4.6 Time vs. potential curve for 2-, 4- and 6-hour experiments.

Following electrolysis, the electrodes were digested in aqua regia to leach out any residual Nd. This was done to determine the total amount of Nd immobilized in the electrode. Assuming that all Nd immobilized is a result of electrolysis, the expected amount of Nd in the carbon electrode based on charge density can be calculated as

$$m_i = \frac{3.6\, M_{w_i} C_h}{n_i F} \qquad [4.1]$$

where m_i is the mass (g) of the immobilized ion, M_{wi} (g/mol) is the molecular weight of the immobilized ion, C_h (mAh) is the electrical charge capacity of the host, n_i is the number of electrons going towards the reaction and F (C/mol) is Faraday's constant.

ICP-MS analysis of the various analytes in Table 4.3 shows an average of 7.3, 4.6, and 3.5 mg of Nd immobilized in the electrode for electrolysis durations of 2, 4, and 6 hours respectively. Furthermore, faradaic efficiency (FE) was calculated based on an expected 20.5 mg theoretical value, obtained from the low current experiment for Nd based on Equation 1. FE decreases from an average of 35.7% to 22.5% to 16.9% for 2, 4, 6 hours respectively. It should also be noted that at 2 hours, the formation of $Nd(OH)_3$ probably accounts for a significant portion of the FE value. Suggesting that 4 hours is optimal if $Nd(OH)_3$ is to be avoided.

Table 4.3 Parameters for electrolysis and ICPM-S measurements of Nd in carbon following electrolysis.

Time (Hr)	Applied Current Denisty (mA g^{-1})	Mass of Carbon (mg)	Charge per mg of Carbon (C)	Charge per cm^2 (C)	ICP-MS - Nd in Carbon (mg)	Standard Deviation	Faradaic Efficiency	Carbon : Nd
2	-178	32.0	1.28	10.3	7.02	0.277	34.3	4.6
2	-178	32.0	1.28	10.3	7.58		37.0	4.2
4	-89.1	32.0	1.28	10.3	4.88	0.263	23.8	6.6
4	-89.1	32.0	1.28	10.3	4.35		21.2	7.4
6	-59.4	32.0	1.28	10.3	3.61	0.144	17.6	8.9
6	-59.4	32.0	1.28	10.3	3.32		16.2	9.6

XRD Analysis of Vulcan XC-72R

Information on the structural and chemical changes on the electrode following electrolysis of 4 and 14.5 hours was obtained through XRD. 14.5 hours was chosen to significantly load the electrode to clearly distinguish the effects of Nd. Loading at 14.5 hours also employed a current density of -89.1 mA g^{-1} in 250 mM $NdCl_3$. XRD information was collected over the range of 2-θ angles of 15 to 80° as seen in Figure 7. It should be noted that the XRD spectra in Figure 7a have been offset for clarity.

Figure 4.7 shows the classic graphite peak corresponding to the {002} family of planes at 25.3° for all samples. This peak is related to the interlayer spacing between the concentric Vulcan XC-72R sheets and arises from parallelism of graphitic layers [294]. However, the broadness of this peak suggest the presence of irregular less-crystalline disordered structures [295], [296]. The disordered and nonparallel nature of these layers indicate the presence of voids and pores between them [297] which can be filled with intercalants [298]. Broadened peaks are also characteristic of TCs containing a mixture of sp^2 and sp^3 hybridized carbon [270]–[273] of which Vulcan XC-72R is a part. Results from XRD also show a dramatic structural change within the carbon electrode at 14.5 hours. Suggesting a nearly damaged structure with shortened length between the carbon layers [299].

Furthermore, the peak associated with the electrolysis duration of 14.5 hours is broadened with a decrease in intensity compared to the blank carbon and 4-hour electrode. Cheng et al. observed this phenomenon during Na^+ insertion into hard carbon. The significant change in structure was attributed to the high Na^+ storage capacity [261]. Likewise, the structural change from this study could suggest the storage of Nd^{3+} within the carbon microstructure. Furthermore, no visible peak shift of the {002} plane is observed. Suggesting that the intercalation of Nd^{3+} between carbon layers is nonexistent or contributes very little to the immobilization of Nd^{3+}. This could be one reason why the sloping region in the time vs potential curves is less pronounced. However, due to the amorphous nature of the carbon, subtle changes are also difficult to detect because of broad diffraction peaks and low graphitization [261], [277], [281].

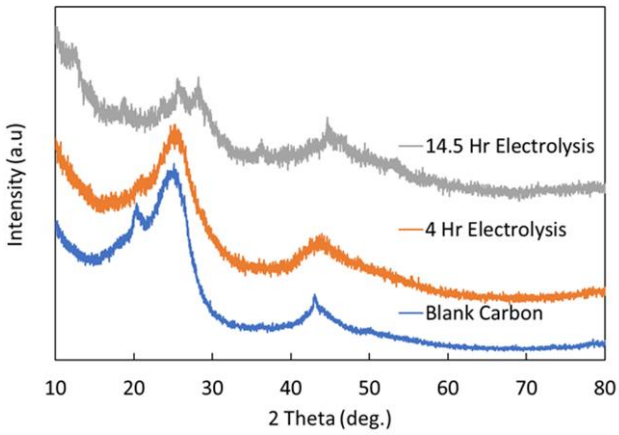

Figure 4.7 *XRD of blank carbon, electrolysis after 4 and 14.5 hours. XRD spectra offset for clarity.*

Also observed at 43° is a low intensity broad peak corresponding to planes of sp^2 hybridized carbon related to the family planes of {100} and {110} [300]. These planes are characteristic TCs [294] [301]. As the duration of electrolysis increases, these planes experience a shift to higher 2-θ angles and associated peaks broaden from a sharp apex. Alcorn, et al. observed that such a shift was the result of Li insertion between defects of the carbon electrode [162]. In this research such an observation could suggest the possibility of Nd^{3+} ions between the pores of the carbon electrode. Hence the more dominant plateau region.

Along with the XRD spectra, structural properties of Vulcan-XC-72R was elucidated in Table 4.4 employing the use of the Scherrer [302], Warren-Scherrer [294], and Braggs law equations [303], [304]

$$L = \frac{k\lambda}{\beta cos\theta} \text{ (Scherrer Equation)} \qquad [4.2]$$

$$L = \frac{0.92\lambda}{\Delta \sin\theta} \text{ (Warren Scherrer Equation} \qquad [4.3]$$

$$d = \frac{n\lambda}{2\sin\theta} \text{ (Bragg's Law Equation)} \qquad [4.4]$$

where L is the crystallite height perpendicular to the plane of refraction, k is coefficient for crystallite shape (0.89 for spherical particles), λ is the x-ray wavelength and β and $\Delta \sin\theta$ is the full width at half maximum (FWHM) of the diffraction peak (in radians), and θ is the angles corresponding to the peak maximum, where d is the interlayer spacing and n is the order of diffraction.

Table 4.4 Structural properties of the Vulcan XC-72R employing the use of Scherrer, Warren-Sherer, and Braggs Law equation.

			Scherrer Eqn.			Scherrer Eqn.		Scherrer-Warren Eqn.	
Samples	FWHM 25.3° (rad)	FWHM 43° (rad)	Lc-25.3° (Å)	d-25.3° (Å)	No. Layers-25.3°	La-43° (Å)	d-43° (Å)	Lc-25.3° (Å)	La-43° (Å)
Blank	0.183	0.092	7.68	3.53	2.18	16.14	2.11	7.75	15.5
4 Hrs.	0.218	0.144	6.47	3.53	1.83	10.28	2.11	6.52	9.88
14.5 Hrs.	0.224	0.191	6.29	3.53	1.78	7.72	2.11	6.34	7.43

No significant difference was observed between the Scherrer and Warren-Scherrer equations for both Vulcan XC-72R thickness (L_c) and lateral spacing (L_a) between Vulcan XC-72R domains as seen in Table 1. The interlayer spacing of the family of planes corresponding to {002} was 3.53 and is in agreement with literature for graphite family of materials [295], [305]–[307]. Furthermore, a decrease of 7.7 Å to 6.3 Å in L_c at 25.3° with increasing electrolysis duration corresponds to a decrease from 2.18 to 1.78 layers respectively. This decrease in L_c suggests the displacement of planes through possible interstitial Nd^{3+} ions in the less ordered stacking of planes.

Furthermore, the L_a value for the blank carbon at the {100} plane compares to that observed by Short and Walker [294]. The change in L_a as electrolysis duration increases is more drastic, where one observes a decrease from ca. 16 Å to ca. 7 Å. Suggesting a decrease in crystallite size. Calculating the spacing between Vulcan XC-72R domains at 43° yields 2.1 Å. Investigating the layered disorder of TCs, Zheng et al. observed that Li would not intercalated into the van der Waal gaps of TC layers [299]. However, the possibility of Li intercalating into voids between graphite domains is possible [275]. Suggesting that the shift of the {100} plane to higher 2-θ values is possibly the immobilization of Nd ions with the pores of the carbon electrode.

The goal of immobilizing Nd^{3+} into TCs such as Vulcan XC-72R is to enable the unload of Nd into ionic liquids (ILs). Up until this point, optimal electrolysis duration based on applied current density, and structural changes have been studied and an electrolysis duration of 4 hours has been selected for further study.

Electrochemical Unload of REEs in 1 M KCl and Ionic liquid (IL)

The feasibility of unloading Nd^{3+} ions from a loaded carbon electrode into 1 M KCl and various ILs was investigated. Four ILs configurations were studied. Prior to unload in 1 M KCl and ILs, various electrodes underwent 4-hour electrolysis in 250 mM $NdCl_3$ at -89.1 mA g^{-1}. Following electrolysis, electrodes were washed with copious amounts of DI water and subjected to an identical unload current density of 89.1 mA g^{-1} in 1 M KCl, or a configuration of IL for 4 hours. Chronopotentiometry time curves in Figure 4.8a show an increase in oxidation potential followed by a sustained potential plateau for Nd^{3+} unload in KCl, pyrrolidinium and CYPHO. However, electrolysis in TBPCl, shows an initial increase in oxidation potential followed by a rapid decrease to almost zero. Suggesting that a preferential side reaction rather than the unload of Nd^{3+} is favored. Furthermore, imidazolium initially appears to have a decreasing potential following a potential rise but recovers to a high potential with a stable plateau.

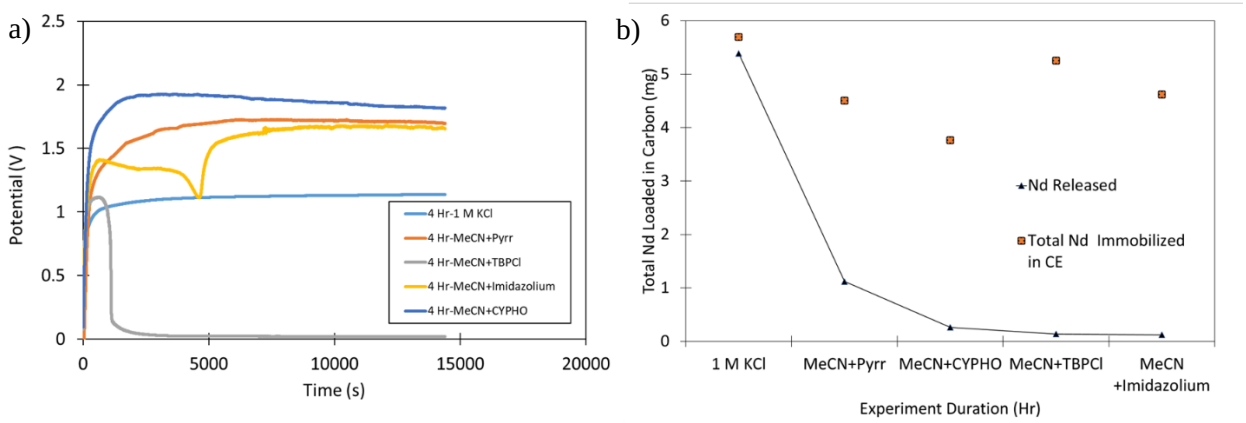

Figure 4.8 a) Chronopotentiometry potential and time curves for unload of Nd in KCl vs Ag/AgCl and various pseudo ionic liquids (PI-Ls vs. Pt). b) comparison between loading in 250 mM $NdCl_3$ and unload in KCl and various ILs.

Table 4.5 shows a unload efficiency of 94.6% in 1M KCl. Pyrrolidinium, CYPHO, imidazolium, and TBPCl, show a unload efficiency of 24.9, 7.0, 2.7, and 2.6% respectively. Suggesting that pyrrolidinium performs better than the other ILs. A visual representation of this is seen in Figure 4.8b with the deceasing trend between KCl and the ILs.

In aqueous media decomposition of the electrolyte results in the formation of gaseous products (H_2 gas) which do not stick onto the surface of the electrode. Thus, electrons on the surface of the

electrode are in direct contact with ions in the electrolyte [308]. However, in organic media decomposition of the electrolyte at the electrode surface could lead to side reactions which hinder the unload of Nd ions and impede charge transfer [237] [308]–[310] [311]. However, studies have shown that high temperature and high charge rate can overcome side reactions in organic electrolyte [309]. This prompted further investigation of the unload of Nd in pyrrolidinium at much higher charge current density.

Table 4.5 Comparison of loading in 250 mM $NdCl_3$ and unloading in 1 M KCl and various ILs.

Experiment Duration (Hr)	Total Nd in CE (mg)	Unloading Media	Nd^{3+} Unloaded (mg)	Unload Efficiency	C/Nd
4	5.70	1 M KCl	5.39	94.6	5.6
4	4.50	MeCN + Pyrr.	1.12	24.9	7.1
4	3.77	MeCN +CYPHO	0.26	7.0	8.5
4	4.62	MeCN +Imidazolium	0.12	2.7	6.9
4	5.26	MeCN + TBPCl	0.14	2.6	6.1

Investigating the Influence of a More Positive Current Density on Nd^{3+} Release in Pyrrolidinium

The effect of a more positive current was studied for Nd^{3+} unloading in pyrrolidinium. A preloaded (CP in aqueous $NdCl_3$) electrode containing Nd^{3+} was subjected to three separate concurrent 356.6 mA g^{-1} pulses. Each pulse lasted for 1 hour and was done in separate pyrrolidinium electrolytes. 356.6 mA g^{-1} is four times higher than what was used as the previous unloading current, 89.1 mA g^{-1}. As such, electrode integrity could also be investigated at very high positive potential using this approach. Following the three separate electrolysis, the electrode showed no visible structural depletion and was digested in aqua regia to determine surplus Nd^{3+}.

Figure 4.9 shows a huge potential difference between the electrode run at 89.1 mA g^{-1} (red dashed line) and those run at 356.6 mA g^{-1} (yellow, blue, and green lines). For the first hour (yellow line), the potential rises to ca. 2.6 V vs. Pt and plateaus. During the second 1 hour (blue line) in fresh pyrrolidinium, the potential rises to a much higher value of ca. 3 V vs. Pt, plateaus for about 21 minutes and decreases to an eventual plateau at ca. 2.6 V vs. Pt. For the final hour (green line) in fresh pyrrolidinium, the potential rises to ca. 3 V vs. Pt similar to the second hour run, decreases to ca. 2.6 V vs. Pt and rises rapidly to the cutoff potential of 3.5 V vs. Pt. The rapid increase in potential to the cutoff potential is observed when the reaction of interest has been completely exhausted [312]–[314].

A second study was done to investigate the effect of a continuous higher oxidation current. A separate electrode loaded with Nd^{3+} was placed under an oxidation current density of 356.6 mA g^{-1} for 3 hours. This was done to investigate the degradation of the electrode over time and to select an efficient way of unloading Nd^{3+} ions into ILs. Following electrolysis, the time curve for the second study (black trace) never reached a concentration polarization. But rather displayed an initial increase followed by a decrease and plateau. One would expect to see a similar sustained increase for 1 hour just as with the separate electrolytes. However, this difference in potential could be due to subtle electrode differences at the surface and its relationship with the products formed during degradation of the organic electrolyte layer.

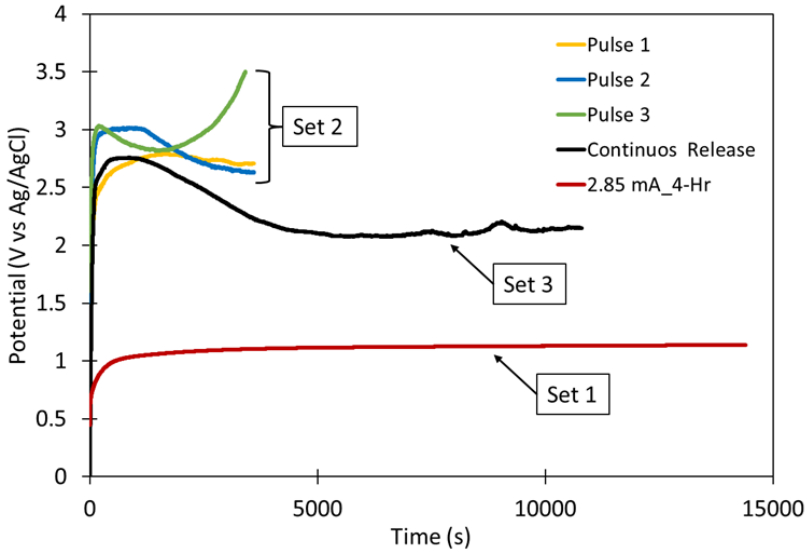

Figure 4.9 Time vs. Potential curves for three electrodes subjected to various electrochemical tests. All electrodes are 8 $g.cm^{-2}$. Set one was run for 4 hours at 89.1 mA g^{-1}. Set 2 was run three times at 356.6 mA g^{-1} for an hour each. Set 3 was run at 356.6 mA g^{-1} for 3 hours.

ICP-MS of the electrolytes in Table 4.6 show that the immobilization of Nd^{3+} into the electrode is a faradaic process. This is because a more positive current is needed to liberate Nd ions into the IL. The unload efficiency for set 1 corresponding to 89.1 mA g^{-1} is the lowest with a value of 24.9% as seen in Table 4.6. However, the study in different electrolytes at 356.6 mA g^{-1} shows a higher unload efficiency of 63% for the first unload in set 2 shown in Figure 4.9. Followed by a decrease in subsequent unloading. Suggesting that a higher current density is essential for initial unload. Decreases in subsequent unloads for set 2 are expected due to the trend observed in Figure 4.9. Also, the unload efficiency of set three corresponding to 356.6 mA g^{-1} for three hours is 46.4%. This was expected due to the time vs potential curve (black trace) observed. While both electrodes (pulsed and non-pulsed) were prepared similarly, slight differences could also affect reproducibility at the

electrode surface. The data from these experiments show that a higher oxidation current in IL is key for unload of Nd. Also, pulsing the electrode is adequate as it somehow overcomes side reactions from IL degradation. Thus, this study proves the ability to immobilize Nd from aqueous solution and unload into ILs.

Table 4.6 ICP-MS analysis of similar electrode under various electrochemical tests. Each set corresponds to a separate 8mg.cm^{-2} Vulcan XC-72R electrode.

	Experiment	Unload Media	Applied Current density (mA g^{-1})	Charge Density (C g^{-1})	Amount of Nd^{3+} in Electrode (mg)	Amount of Nd Unloaded (mg)	Unload Efficiency (%)	Charge / mg Carbon	Charge per area (C.cm^{-2})	Carbon / Nd
Set 1	4-Hour	MeCN + Pyrr.	89.1	1284	4.50	1.12	24.9	1.28	10.3	7.11
	Pulse 1	MeCN + Pyrr.	356.6	1300	4.81	3.06	63.5	1.30	10.4	6.65
Set 2	Pulse 2	MeCN + Pyrr.	356.6	1284	1.75	0.39	8.1	1.28	10.3	18.2
	Pulse 3	MeCN + Pyrr.	356.6	1219	1.37	0.03	0.7	1.22	9.75	23.4
Set 3	Continuous Unload	MeCN + Pyrr.	356.6	3844	3.93	1.82	46.4	3.85	30.8	8.15

Concentration of Nd^{3+} and Reusability of Electrode

Changes in physical and chemical structure during separate successive electrolysis of an electrode alter time vs. potential curves. However, the time vs. potential curve curves of an electrode with a stable physical and chemical structure should have little to no variability during successive electrolytic tests. The feasibility of reusing the carbon electrode to concentrate Nd into a blank solution of 1 M KCl was investigated. The electrolyte was 250 mM $NdCl_3$. The duration and current density applied during Nd^{3+} immobilization were -89.1 mA g^{-1} and 4 hours respectively. The first two unloads were done in the same KCl solution. The duration of each unload was 4 hours at 89.1 mA g^{-1}. Six subsequent unloadings after the first two were done in separate KCl electrolytes. These had a duration of 2 hours at 178 mA g^{-1}. The increase to a more positive unloading current was employed to investigate the stability of the electrode during unloading in aqueous electrolyte. Fresh $NdCl_3$ was employed for each loading of Nd^{3+}.

Figure 4.10 shows that with the exception of the initial loading of Nd^{3+} into the electrode, time vs. potential curves are similar during Nd^{3+} immobilization. The deviation of the initial time vs. potential curve in Figure 4.10a is an example of the structural change due to initial immobilization of Nd^{3+}. Furthermore, unloading of Nd^{3+} in KCl also shows similarities within plots as seen in Figure 4.10b.

The effect of the more positive current following the first initial two unloading is displayed as an upward shift to more positive values as seen in Figure 4.10b.

Table 4.7 shows that Nd^{3+} can be concentrated into a single blank solution of 1 M KCl. Successive unloading into different KCl electrolytes shows an average of 4.19 mg of Nd and a standard deviation of 0.454. Suggesting a consistent and more stable electrode. Observed during the unloading of Nd was the presence of some binder dissolution (dark brown powder) as seen in Figure 4.11. However, the carbon electrode remained visibly intact. This test proves the stability of the electrode and promising nature of the Vulcan XC-72R for Nd^{3+} capture and unload in aqueous solution.

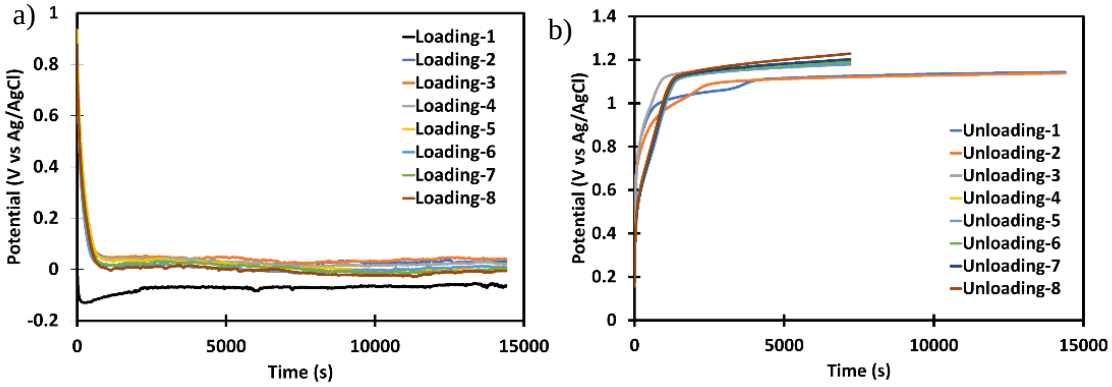

Figure 4.10 a) Intercalating potential time curves at -2.85 mA for 4 hours in 250 mM $NdCl_3$, and b) Potential time curves for unload of Nd into 1 M KCl at 89.1 mA g^{-1} for the first two unloads and 178 mA g^{-1} for all subsequent unloads

Table 4.7 Concentration of Nd into a single KLC solution as well as unload into different KCl solutions.

Cycling Number	Nd(mg)	Unload Duration (Hr.)
*0	8.05	8
1	3.36	2
2	3.95	2
3	4.12	2
4	4.72	2
5	4.56	2
6	4.44	2
Average	**4.19**	
Standard Deviation	**0.454**	

* Represents concentration experiment and unloading of two loading of Nd^{3+} into single KCL solution

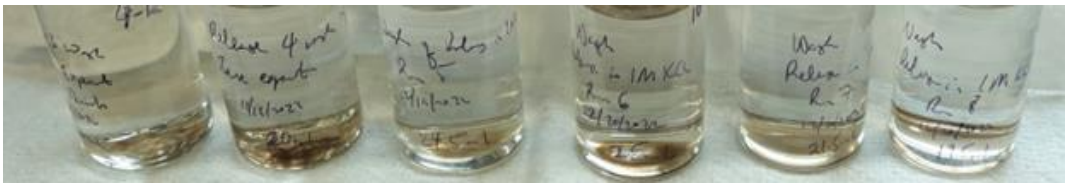

Figure 4.11**.** Dark brown sediment at the bottom of vial showing possible binder degradation.

Conclusion

A 32 mg electrode of a TC (Vulcan XC-7R) was loaded with Nd^{3+} ions and unloaded in both aqueous KCl and ILs. Duration of electrolysis corresponds to applied current densities and play a major function in the appropriate electrochemical capture of Nd ions. Above -89.1 mA g^{-1}, the formation of $Nd(OH)_3$ is very likely. However, at 89.1 mA g^{-1} which corresponds to an electrolysis time of 4 hours, HER is almost nonexistent. A 4-hour electrolysis duration was optimal for Nd immobilization and was chosen for further studies. The ability to concentrate Nd ions in a single blank solution such as KCl was proven. Furthermore, the stability of the electrode was tested, and multiple cycling tests showed consistency in Nd capture. However, while the carbon electrode might not degrade, the binder might degrade over time. Thus, making the binder the limiting factor to electrode lifetime. Also, unload in various IL were tested and pyrrolidinium proved to be the most favorable IL. Further tests on pyrrolidinium at more positive unload current density showed greater unload of Nd. Suggesting strongly that the magnitude of the applied current density affects the unload of intercalated Nd species and overcomes side reactions due to degradation of the organic electrolyte.

Chapter 5: Conclusion

Low temperature (<40 °C) electrochemical immobilization of rare earth elements (REEs) provides a promising approach for retrieving REEs from mining ores and end-of-life products (recyclability). Ga and its oxides were investigated as possible material for immobilizing REEs. During the reduction of Ga oxides in the presence of Pr^{3+}, > 50% of the Pr^{3+} was concentrated from diluted aqueous electrolytes. Circulation of the liquid Ga enabled the formation of surface oxides which are crucial for the capture of Pr^{3+}. Furthermore, when Ga oxides are digested in 1 M HCl, Ga reverts to a metal and can be recycled and used for further capture of Pr.

Likewise, MnO_2 was also investigated. The capture mechanism for MnO_2 involved adoption and diffusion. Capture of Nd^{3+} from the REE electrolyte was on the milligram scale order. A cycling rate of C/20 was optimal with less dissolution of Nd^{3+}. The limiting factor of using MnO_2 as an electrode is less stability in aqueous solution due to dissolution. MnO_2 undergoes a disproportionation reaction in aqueous solution, leading to the loss of material during electrolysis. For intercalations, an electrode needs to be stable in both aqueous and ionic liquid electrolytes. This characteristic is crucial to reuse and cyclability. While MnO_2 showed promise in Nd intercalation in REE aqueous solution, dissolution makes it a less ideal candidate.

Also, a tubostratic carbon material was investigated. The carbon electrode showed excellent stability during cycling as well as consistent Nd^{3+} capture. The ability to concentrate Nd ions in a single blank solution such as KCl was proven. Unload in various IL were tested and pyrrolidinium proved to be the most favorable IL. In IL, a more positive unload current density showed greater unload of Nd^{3+}. Suggesting strongly that the magnitude of the applied current density affects the unload of intercalated Nd species and overcomes side reactions due to degradation of the organic electrolyte.

The demonstration of low temperature REE capture from aqueous streams was proven. These processes can be improved on and employed as alternate green capture methods for REEs.

Furthermore, this technology can be used as part of the process stream for spent nuclear fuel for immobilizing rare earth and other cations. The realization of this would greatly reduce the chemical and energy consumption of conventional spent fuel reprocessing methods. Also, an alternative use for this technology could be the unloading of nuclear reactor poisons or neutron absorbers to control the criticality of a nuclear reactor via an anode reaction.

References

[1] J.-C. G. Bünzli, “Lanthanides,” *Kirk-Othmer Encyclopedia of Chemical Technology*. pp. 1–43, Jul. 19, 2013, doi: doi:10.1002/0471238961.1201142019010215.a01.pub3.

[2] S. B. Castor and J. B. Hedrick, “Rare earth elements,” *Ind. Miner. rocks*, pp. 769–792, 2006.

[3] P. Davris, E. Balomenos, M. Taxiarchou, D. Panias, and I. Paspaliaris, “Current and alternative routes in the production of rare earth elements,” *BHM Berg-und Hüttenmännische Monatshefte*, vol. 162, no. 7, pp. 245–251, 2017.

[4] P. C. Dent, “Rare earth elements and permanent magnets,” *J. Appl. Phys.*, vol. 111, no. 7, p. 07A721, 2012.

[5] C. J. Ferron and P. Henry, “A review of the recycling of rare earth metals,” *Can. Metall. Q.*, vol. 54, no. 4, pp. 388–394, 2015.

[6] H. Royen and U. Fortkamp, “Rare earth elements-purification, separation and recycling,” *Environ. Res. Inst. Stock. Sweden*, 2016.

[7] T. Cheisson and E. J. Schelter, “Rare earth elements: Mendeleev’s bane, modern marvels,” *Science (80-.).*, vol. 363, no. 6426, pp. 489–493, 2019.

[8] E. O. Opare, E. Struhs, and A. Mirkouei, “A comparative state-of-technology review and future directions for rare earth element separation,” *Renew. Sustain. Energy Rev.*, vol. 143, p. 110917, 2021.

[9] K. J. Strnat, “Rare-earth magnets in present production and development,” *J. Magn. Magn. Mater.*, vol. 7, no. 1, pp. 351–360, 1978, doi: https://doi.org/10.1016/0304-8853(78)90218-4.

[10] K. Zhang, A. N. Kleit, and A. Nieto, “An economics strategy for criticality–Application to rare earth element Yttrium in new lighting technology and its sustainable availability,” *Renew. Sustain. Energy Rev.*, vol. 77, pp. 899–915, 2017.

[11] D. Schüler, M. Buchert, R. Liu, S. Dittrich, and C. Merz, “Study on rare earths and their recycling,” *Öko-Institut eV Darmstadt*, vol. 49, pp. 30–40, 2011.

[12] J.-R. Riba, C. López-Torres, L. Romeral, and A. Garcia, “Rare-earth-free propulsion motors for electric vehicles: A technology review,” *Renew. Sustain. Energy Rev.*, vol. 57, pp. 367–379, 2016.

[13] X. Song, M.-H. Chang, and M. Pecht, “Rare-earth elements in lighting and optical applications and their recycling,” *Jom*, vol. 65, no. 10, pp. 1276–1282, 2013.

[14] N. Curtis, “Rare earths, we can touch them everyday,” *Lynas Present. JP Morgan Aust. Corp. Access Days, New York, 27e28 Sept.*, 2010.

[15] K. Binnemans *et al.*, “Recycling of rare earths: a critical review,” *J. Clean. Prod.*, vol. 51, pp. 1–22, 2013.

[16] V. Zepf, “Rare Earth Elements: What and where they are,” in *Rare earth elements*, Springer, 2013, pp. 11–39.

[17] U. S. D. of Energy, “Critical materials strategy.” US Department of Energy Washington, DC, USA, 2011.

[18] E. Alonso *et al.*, “Evaluating rare earth element availability: A case with revolutionary demand from clean technologies,” *Environ. Sci. Technol.*, vol. 46, no. 6, pp. 3406–3414, 2012.

[19] M. K. Jha, A. Kumari, R. Panda, J. R. Kumar, K. Yoo, and J. Y. Lee, “Review on hydrometallurgical recovery of rare earth metals,” *Hydrometallurgy*, vol. 165, pp. 2–26, 2016.

[20] N. T. Nassar, X. Du, and T. E. Graedel, “Criticality of the rare earth elements,” *J. Ind. Ecol.*, vol. 19, no. 6, pp. 1044–1054, 2015.

[21] F. Habashi, “Extractive metallurgy of rare earths,” *Can. Metall. Q.*, vol. 52, no. 3, pp. 224–233, Jul. 2013, doi: 10.1179/1879139513Y.0000000081.

[22] D. J. Astley, J. R. B. Gilbert, I. R. Scholes, J. S. Jacobi, and G. R. Brookes, “Electrowinning metals.” Google Patents, Aug. 02, 1977.

[23] T. E. Norman, “Electrolytic cell for electrowinning of metals.” Google Patents, Dec. 12, 1978.

[24] R. D. Prengaman and J. L. Howard, “Method of manufacturing electrowinning anode.” Google Patents, Feb. 15, 1983.

[25] A. Brenner, *Electrodeposition of alloys: principles and practice*. Elsevier, 2013.

[26] S. Singh and A. L. Pappachan, “Electrowinning of cerium group metals from fused chloride bath,” *Bull. Mater. Sci.*, vol. 2, no. 3, pp. 155–159, 1980, doi: 10.1007/BF02745402.

[27] Z. Xing, J. Lu, and X. Ji, “A Brief Review of Metallothermic Reduction Reactions for Materials Preparation,” *Small Methods*, vol. 2, no. 12, p. 1800062, Dec. 2018, doi: 10.1002/smtd.201800062.

[28] R. A. Sharma, “Metallothermic reduction of rare earth chlorides.” Google Patents, Jul. 14, 1987.

[29] T. H. Okabe and D. R. Sadoway, “Metallothermic reduction as an electronically mediated reaction,” *J. Mater. Res.*, vol. 13, no. 12, pp. 3372–3377, 1998, doi: DOI: 10.1557/JMR.1998.0459.

[30] R. A. Sharma, “Metallothermic reduction of rare earth oxides with calcium metal,” 1986.

[31] J. L. Moriarty, “The industrial preparation of the rare earth metals by metallothermic reduction,” *JOM*, vol. 20, no. 11, pp. 41–45, 1968.

[32] H. Zeiringer, “Proces for the production of rare earth metals and alloys.” Google Patents, Nov. 22, 1988.

[33] D. K. Bose, O. K. Mehra, and C. K. Gupta, “Preparation of rare earth-silicon-iron alloy by metallothermic reduction,” *J. Less Common Met.*, vol. 110, no. 1–2, pp. 239–242, 1985.

[34] G. Meyer, “The Reduction of Rare-Earth Metal Halides with Unlike Metals – Wöhler’s Metallothermic Reduction,” *Zeitschrift für Anorg. und Allg. Chemie*, vol. 633, no. 15, pp. 2537–2552, Nov. 2007, doi: 10.1002/zaac.200700386.

[35] H. Liu, Y. Zhang, Y. Luan, H. Yu, and D. Li, “Research Progress in Preparation and Purification of Rare Earth Metals,” *Metals (Basel).*, vol. 10, no. 10, p. 1376, 2020.

[36] N. KRISHNAMURTHY and C. K. GUPTA, “Rare Earth Metals and Alloys by Electrolytic Methods,” *Miner. Process. Extr. Metall. Rev.*, vol. 22, no. 2, pp. 477–507, Jan. 2001, doi: 10.1080/08827509808962512.

[37] B.-L. Yan *et al.*, “Synthesis of Ti powders with different morphologies via controlling the valence state of the titanium ion in KCl-NaCl molten salt,” *J. Electroanal. Chem.*, vol. 876, p. 114496, 2020.

[38] Z. Zhou *et al.*, “Molten salt electrolytic synthesis of silicon-copper composite nanowires with enhanced performances as lithium ion battery anode,” *J. Alloys Compd.*, vol. 751, pp. 307–315, 2018.

[39] J. Zhang *et al.*, “Preparation of high-purity straight silicon nanowires by molten salt electrolysis,” *J. Energy Chem.*, vol. 40, pp. 171–179, 2020.

[40] R.-R. Xu and Q. Su, “Chapter 2 - High Temperature Synthesis,” R. Xu and Y. B. T.-M. I. S. C. (Second E. Xu, Eds. Amsterdam: Elsevier, 2017, pp. 9–43.

[41] F. J. Vidal-Iglesias, J. Solla-Gullón, A. Rodes, E. Herrero, and A. Aldaz, “Understanding the Nernst equation and other electrochemical concepts: an easy experimental approach for students,” *J. Chem. Educ.*, vol. 89, no. 7, pp. 936–939, 2012.

[42] E. Morrice, C. Wyche, and T. A. Henrie, *Electrowinning Molten Lanthanum From Lanthanum Oxide*, no. 6075–6080. US Department of the Interior, Bureau of Mines, 1962.

[43] E. Morrice, *Electrowinning cerium-group and yttrium-group metals*, vol. 5868. US Department of the Interior, Bureau of Mines, 1961.

[44] R. Thudum, A. Srivastava, S. Nandi, A. Nagaraj, and R. Shekhar, “Molten salt electrolysis of neodymium: electrolyte selection and deposition mechanism,” *Miner. Process. Extr. Metall.*, vol. 119, no. 2, pp. 88–92, 2010.

[45] M. F. Chambers and J. E. Murphy, *Electrolytic production of neodymium metal from a molten chloride electrolyte*, vol. 9391. US Department of the Interior, Bureau of Mines, 1991.

[46] E. H. Kobisk and W. B. Grisham, "Application of reduction-distillation method for preparing high-purity rare-earth isotope metals," *Mater. Res. Bull.*, vol. 4, no. 9, pp. 651–662, 1969.

[47] W. F. Hillebrand and T. H. Norton, "Electrolytic deposition of cerium, lanthanum and didymium," *Ann. Phys. U. Chem*, vol. 155, pp. 633–639, 1875.

[48] W. Muthmann, H. Hofer, and L. Weiss, "On the preparation of metals of the cerium group by molten electrolysis," *Ann. Chem.*, vol. 320, pp. 231–269, 1902.

[49] A. Hirsch, *The preparation and properties of metallic cerium*. The Society, 1911.

[50] H. C. Kremers and R. G. Stevens, "Observations on the rare earths. XIV. The preparation and properties of metallic lanthanum," *J. Am. Chem. Soc.*, vol. 45, no. 3, pp. 614–617, 1923.

[51] M. Billy and F. Trombe, "Preparation of pure cerium," *Compt. rend.*, vol. 193, pp. 421–423, 1931.

[52] I. S. Hirschhorn, "Commercial production of rare earth metals by fused salt electrolysis," *JOM*, vol. 20, no. 3, pp. 19–22, 1968.

[53] E. S. Shedd, J. D. Marchant, and T. A. Henrie, *Electrowinning and tapping of lanthanum metal*, vol. 6882. US Department of the Interior, Bureau of Mines, 1966.

[54] T. A. Henrie and E. Morrice, "V. A high-temperature electrowinning cell for rare earths," *JOM*, vol. 18, no. 11, pp. 1207–1208, 1966.

[55] E. Morrice and T. A. Henrie, *Electrowinning high-purity neodymium, praseodymium, and didymium metals from their oxides*, vol. 6957. US Department of the Interior, Bureau of Mines, 1967.

[56] E. Morrice and R. G. Knickerbocker, "Rare-Earth Electrolytic Metals," *Rare Earths*, pp. 126–144, 1961.

[57] K. J. CATHRO, R. L. DEUTSCHER, and R. A. SHARMA, "Electrowinning magnesium from its oxide in a melt containing neodymium chloride," *J. Appl. Electrochem.*, vol. 27, no. 4, pp. 404–413, 1997, doi: 10.1023/A:1018457503240.

[58] B. Cai *et al.*, "Estimating perfluorocarbon emission factors for industrial rare earth metal electrolysis," *Resour. Conserv. Recycl.*, vol. 136, pp. 315–323, 2018.

[59] X. Zhu, S. Sun, C. Liu, and G. Tu, "Solubility of RE2O3 (RE= La and Nd) in light rare earth fluoride molten salts," *J. Rare Earths*, vol. 36, no. 7, pp. 765–771, 2018.

[60] A. Kaneko, Y. Yamamoto, and C. Okada, "Electrochemistry of rare earth fluoride molten salts," *J. Alloys Compd.*, vol. 193, no. 1–2, pp. 44–46, 1993.

[61] E. Morrice, “Molten salt electrowinning of rare-earth and yttrium metals and alloys,” in *New frontiers in rare earth science and applications*, 1985.

[62] W. Muthmann and J. Scheidemandel, “On the extraction of the rare earth metals by the electrolysis of the fluorides,” *Ann. Chem.*, vol. 355, pp. 116–136, 1907.

[63] H. Vogel, B. Flerus, F. Stoffner, and B. Friedrich, “Reducing greenhouse gas emission from the neodymium oxide electrolysis. Part I: analysis of the anodic gas formation,” *J. Sustain. Metall.*, vol. 3, no. 1, pp. 99–107, 2017.

[64] P. M. J. Gray, “The production of pure cerium metal by electrolytic and thermal reduction processes,” *Trans. Inst. Min. Met.*, vol. 61, 1952.

[65] D. Kingsnorth, “The global rare earth industry today—plagued by illegal production in China,” in *11th Rare Earth Conference, Metal Events Ltd., Singapore*, 2015.

[66] E. Stefanidaki, G. M. Photiadis, C. G. Kontoyannis, A. F. Vik, and T. Østvold, “Oxide solubility and raman spectra of NdF 3–LiF–KF–MgF 2–Nd 2 O 3 melts,” *J. Chem. Soc. Dalt. Trans.*, no. 11, pp. 2302–2307, 2002.

[67] E. Stefanidaki, C. Hasiotis, and C. Kontoyannis, “Electrodeposition of neodymium from LiF–NdF3–Nd2O3 melts,” *Electrochim. Acta*, vol. 46, no. 17, pp. 2665–2670, 2001.

[68] G. D. Smith, *From monopoly to competition: The transformations of Alcoa, 1888-1986*. Cambridge University Press, 2003.

[69] J. Wisniak, “Henri étienne sainte-claire deville: a physician turned metallurgist,” *J. Mater. Eng. Perform.*, vol. 13, no. 2, pp. 117–128, 2004.

[70] M. M. Trescott, “Julia B. Hall and aluminum,” *J. Chem. Educ.*, vol. 54, no. 1, p. 24, 1977.

[71] K. Yasuda, K. Saegusa, and T. H. Okabe, “Aluminum subhalide as a reductant for metallothermic reduction,” *High Temp. Mater. Process.*, vol. 30, no. 4, pp. 411–423, 2011.

[72] U. B. Pal, D. E. Woolley, and G. B. Kenney, “Emerging SOM technology for the green synthesis of metals from oxides,” *Jom*, vol. 53, no. 10, pp. 32–35, 2001.

[73] A. Bogacz, S. Rumianowski, W. Szymanski, and W. Szklarski, “Technology of light lanthanide metals production,” in *Advances in Molten Salts*, Begell House, 1999.

[74] W. Klemm and H. Bommer, “Contribution to the knowledge of the rare earths,” *Z. anorg. allg. Chem*, vol. 231, pp. 138–171, 1937.

[75] T. Uda, K. T. Jacob, and M. Hirasawa, “Technique for Enhanced Rare Earth Separation,” *Science (80-.).*, vol. 289, no. 5488, pp. 2326 LP – 2329, Sep. 2000, doi: 10.1126/science.289.5488.2326.

[76] K. C. Sole, P. M. Cole, A. M. Feather, and M. H. Kotze, “Solvent extraction and ion exchange applications in Africa’s resurging uranium industry: a review,” *Solvent Extr. ion Exch.*, vol. 29, no. 5–6, pp. 868–899, 2011.

[77] R. M. Diamond and D. C. Whitney, “Resin selectivity in dilute to concentrated aqueous solutions,” *Ion Exch.*, vol. 1, pp. 277–351, 1966.

[78] V. Rychkov *et al.*, “Rare Earth Element Preconcentration from Various Primary and Secondary Sources by Polymeric Ion Exchange Resins,” *Sep. Purif. Rev.*, pp. 1–16, 2021.

[79] F. G. Helfferich, *Ion exchange*. Courier Corporation, 1995.

[80] D. I. Smirnov, T. V Molchanova, L. I. Vodolazov, and V. A. Peganov, “The sorption recovery of rare earth elements, yttrium and aluminium from the red mud,” *Tsvetnye Met.*, pp. 64–69, 2002.

[81] D. I. Smirnov and T. V Molchanova, “The investigation of sulphuric acid sorption recovery of scandium and uranium from the red mud of alumina production,” *Hydrometallurgy*, vol. 45, no. 3, pp. 249–259, 1997.

[82] M. Mikhaylenko, “Development and Screening of Resins to Recover REE and Scandium from Different Sources,” in *Extraction 2018*, Springer, 2018, pp. 2113–2122.

[83] N. M. Shokobayev, C. Bouffier, and T. S. Dauletbakov, “Rare earth metals sorption recovery from uranium in situ leaching process solutions,” *Rare Met.*, vol. 34, no. 3, pp. 195–201, 2015.

[84] V. N. Rychkov *et al.*, “Selective ion exchange recovery of rare earth elements from uranium mining solutions,” in *AIP Conference Proceedings*, 2016, vol. 1767, no. 1, p. 20017.

[85] L. A. Bobkova, “Sorption selectivity of rare-earth elements ions by KB-2E macroreticular carboxylic cation exchanger,” in *Advanced Materials Research*, 2015, vol. 1085, pp. 101–106.

[86] G. R. Choppln and F. Ohene-Aniapam, “Equilibrium Sorption of on Am (III), Ce (III) and Eu (III) Bio-Rex 70 Ion Exchange Resin,” *Solvent Extr. Ion Exch.*, vol. 1, no. 3, pp. 585–595, 1983.

[87] R. Arnold and L. B. S. Hing, “Selectivity of carboxylic ion-exchange resin for lanthanide ions,” *J. Chem. Soc. A Inorganic, Phys. Theor.*, pp. 306–308, 1967.

[88] R. Bogoczek and J. Surowiec, “Chemical modification of styrene-divinylbenzene copolymers by dialkyl phosphites,” *Polymer (Guildf).*, vol. 27, no. 4, pp. 631–634, 1986.

[89] R. Bogoczek and J. Surowiec, “Synthesis of phosphorus-containing wofatit cation exchangers and their affinity toward selected cations,” *J. Appl. Polym. Sci.*, vol. 26, no. 12, pp. 4161–4173, 1981.

[90] S. D. Alexandratos, M. A. Strand, D. R. Quillen, and A. J. Walder, “Synthesis and characterization of bifunctional phosphinic acid resins,” *Macromolecules*, vol. 18, no. 5, pp. 829–835, 1985.

[91] S. D. Alexandratos, D. R. Quillen, and M. E. Bates, “Synthesis and characterization of bifunctional ion-exchange/coordination resins,” *Macromolecules*, vol. 20, no. 6, pp. 1191–1196, 1987.

[92] J. I. Bregman and Y. Murata, “Phosphonous and phosphonic cation exchange resins,” *J. Am. Chem. Soc.*, vol. 74, no. 7, pp. 1867–1868, 1952.

[93] X. Hérès *et al.*, “Selective extraction of rare earth elements from phosphoric acid by ion exchange resins,” *Metals (Basel).*, vol. 8, no. 9, p. 682, 2018.

[94] S. Dutta, P. K. Mohapatra, G. D. Dhekane, A. K. Das, and V. K. Manchanda, “Solid phase extraction of europium and uranium using Tulsion CH-90 resin,” *Desalination*, vol. 232, no. 1–3, pp. 216–224, 2008.

[95] A. Yuchi, T. Sato, Y. Morimoto, H. Mizuno, and H. Wada, “Adsorption mechanism of trivalent metal ions on chelating resins containing iminodiacetic acid groups with reference to selectivity,” *Anal. Chem.*, vol. 69, no. 15, pp. 2941–2944, 1997.

[96] M. J. Page, K. Soldenhoff, and M. D. Ogden, “Comparative study of the application of chelating resins for rare earth recovery,” *Hydrometallurgy*, vol. 169, pp. 275–281, 2017.

[97] Y. Yang and S. D. Alexandratos, “Affinity of polymer-supported reagents for lanthanides as a function of donor atom polarizability,” *Ind. Eng. Chem. Res.*, vol. 48, no. 13, pp. 6173–6187, 2009.

[98] G. Jeanneret-Gris, “Chelating resins and method for their use in the extraction of metal ions.” Google Patents, Apr. 06, 1993.

[99] S. D. Alexandratos and D. W. Crick, “Polymer-supported reagents: Application to separation science,” *Ind. Eng. Chem. Res.*, vol. 35, no. 3, pp. 635–644, 1996.

[100] R. A. Beauvais and S. D. Alexandratos, “Polymer-supported reagents for the selective complexation of metal ions: an overview,” *React. Funct. Polym.*, vol. 36, no. 2, pp. 113–123, 1998.

[101] E. Müller, R. Berger, E. Blass, D. Sluyts, and A. Pfennig, “Liquid–liquid extraction,” *Ullmann’s Encycl. Ind. Chem.*, 2000.

[102] C. Hanson, “Recent advances in liquid-liquid extraction,” 2013.

[103] J. Zhang, B. Zhao, and B. Schreiner, “Separation hydrometallurgy of rare earth elements,” 2016.

[104] F. Xie, T. A. Zhang, D. Dreisinger, and F. Doyle, “A critical review on solvent extraction of rare earths from aqueous solutions,” *Miner. Eng.*, vol. 56, pp. 10–28, 2014.

[105] N. A. Ismail, M. A. A. Aziz, M. Y. M. Yunus, and A. Hisyam, “Selection of extractant in rare earth solvent extraction system: A review,” *Int. J. Recent Technol. Eng*, vol. 8, no. 1, pp. 728–743, 2019.

[106] D. F. Peppard and G. W. Wason, “Liquid-liquid extraction of trivalent rare earths using acidic phosphonates as extractants,” in *Rare Earth Research*, vol. 37, The Macmillan Company New York, 1961.

[107] C. G. Brown and L. G. Sherrington, “Solvent extraction used in industrial separation of rare earths,” *J. Chem. Technol. Biotechnol.*, vol. 29, no. 4, pp. 193–209, 1979.

[108] L. Sherrington, “Commercial processes for rare earths and thorium,” *Handb. Solvent Extr.*, pp. 717–723, 1983.

[109] L. Deqian, W. Zhonghuai, S. Wenzhong, M. Shulan, and M. Gengxiang, “Recommended separation processes for ion-absorbed rare earth minerals,” in *Hydrometallurgy’94*, Springer, 1994, pp. 627–634.

[110] D. J. Bauer and R. E. Lindstrom, *Naphthenic Acid Solvent Extraction of Rare-earth Sulphates*, vol. 6396. US Department of the Interior, Bureau of Mines, 1964.

[111] D. Zheng, N. B. Gray, and G. W. Stevens, “Comparison of naphthenic acid, versatic acid and D2EHPA for the separation of rare earths,” *Solvent Extr. ion Exch.*, vol. 9, no. 1, pp. 85–102, 1991.

[112] J. Arichi, G. Goetz-Grandmont, and J. P. Brunette, “Solvent extraction of europium(III) from nitrate medium with 4-acyl-isoxazol-5-ones and 4-acyl-5-hydroxy-pyrazoles. Effect of salts and diluents,” *Hydrometallurgy*, vol. 82, no. 1, pp. 100–109, 2006, doi: https://doi.org/10.1016/j.hydromet.2006.04.004.

[113] T. S. Urbanski, P. Fornari, and C. Abbruzzese, “The extraction of cerium (III) and lanthanum (III) from chloride solutions with LIX 54,” *Hydrometallurgy*, vol. 40, no. 1, pp. 169–179, 1996, doi: https://doi.org/10.1016/0304-386X(94)00082-E.

[114] J. S. Preston, P. M. Cole, A. C. du Preez, M. H. Fox, and A. M. Fleming, “The recovery of rare earth oxides from a phosphoric acid by-product. Part 2: The preparation of high-purity cerium dioxide and recovery of a heavy rare earth oxide concentrate,” *Hydrometallurgy*, vol. 41, no. 1, pp. 21–44, 1996, doi: https://doi.org/10.1016/0304-386X(95)00067-Q.

[115] J. S. Preston, P. M. Cole, W. M. Craig, and A. M. Feather, “The recovery of rare earth oxides from a phosphoric acid by-product. Part 1: Leaching of rare earth values and recovery of a mixed rare earth oxide by solvent extraction,” *Hydrometallurgy*, vol. 41, no. 1, pp. 1–19, 1996, doi: https://doi.org/10.1016/0304-386X(95)00051-H.

[116] J. S. Preston, A. C. Du Preez, P. M. Cole, and M. H. Fox, “The recovery of rare earth oxides from a phosphoric acid by-product. Part 3. The separation of the middle and light rare earth fractions and the preparation of pure europium oxide,” *Hydrometallurgy*, vol. 42, no. 2, pp. 131–149, 1996.

[117] O. A. Desouky, A. M. Daher, Y. K. Abdel-Monem, and A. A. Galhoum, “Liquid–liquid extraction of yttrium using primene-JMT from acidic sulfate solutions,” *Hydrometallurgy*, vol. 96, no. 4, pp. 313–317, 2009, doi: https://doi.org/10.1016/j.hydromet.2008.11.009.

[118] K. H. Hsu, C. H. Huang, T. C. King, and P. K. Li, “Separation of praseodymium and neodymium in high purity (99.9%) by counter-current exchange extraction and its mechanism,” in *Proceedings of International Solvent Extraction Conference*, 1980, vol. 80, pp. 80–82.

[119] M. Černá, E. Volaufová, and V. Rod, “Extraction of light rare earth elements by amines at high inorganic nitrate concentration,” *Hydrometallurgy*, vol. 28, no. 3, pp. 339–352, 1992, doi: https://doi.org/10.1016/0304-386X(92)90039-3.

[120] G. W. Mason, I. Bilobran, and D. F. Peppard, “Extraction of U(VI), Th(IV), Am(III) and Eu(III) by bis para-octylphenyl phosphoric acid in benzene diluent,” *J. Inorg. Nucl. Chem.*, vol. 40, no. 10, pp. 1807–1810, 1978, doi: https://doi.org/10.1016/0022-1902(78)80230-9.

[121] R. Banerjee, A. Mohanty, S. Chakravarty, S. Chakladar, and P. Biswas, “A single-step process to leach out rare earth elements from coal ash using organic carboxylic acids,” *Hydrometallurgy*, vol. 201, p. 105575, 2021.

[122] Q. Zhao, Z. Zhang, Y. Li, X. Bian, and W. Liao, “Solvent extraction and separation of rare earths from chloride media using α-aminophosphonic acid extractant HEHAMP,” *Solvent Extr. ion Exch.*, vol. 36, no. 2, pp. 136–149, 2018.

[123] K. Shimojo *et al.*, “Highly efficient extraction separation of lanthanides using a diglycolamic acid extractant,” *Anal. Sci.*, vol. 30, no. 2, pp. 263–269, 2014.

[124] R. D. Abreu and C. A. Morais, “Study on separation of heavy rare earth elements by solvent extraction with organophosphorus acids and amine reagents,” *Miner. Eng.*, vol. 61, pp. 82–87, 2014.

[125] T. Sato, “Liquid-liquid extraction of rare-earth elements from aqueous acid solutions by acid organophosphorus compounds,” *Hydrometallurgy*, vol. 22, no. 1–2, pp. 121–140, 1989.

[126] R. Banda, H. Jeon, and M. Lee, “Solvent extraction separation of Pr and Nd from chloride solution containing La using Cyanex 272 and its mixture with other extractants,” *Sep. Purif. Technol.*, vol. 98, pp. 481–487, 2012, doi: https://doi.org/10.1016/j.seppur.2012.08.015.

[127] E. I. Onstott, “Separation of the Lanthanons at Amalgam Cathodes. Measurement of the Separability of Praseodymium and Neodymium in Aqueous Lithium Citrate Electrolytes,” *Anal. Chem.*, vol. 33, no. 11, pp. 1470–1473, 1961.

[128] E. I. Onstott, “Separation of the Lanthanons at Amalgam Cathodes. II. The Separation of Samarium from Gadolinium and Purification of Europium at a Lithium Amalgam Cathode1,” *J. Am. Chem. Soc.*, vol. 78, no. 10, pp. 2070–2076, 1956.

[129] G. M. Kolesov and L. N. Pankratova, “Separation of Rare-earth Elements by Electrolysis at a Mercury Cathode,” *Russ. Chem. Rev.*, vol. 37, no. 9, pp. 701–710, 1968, doi: 10.1070/rc1968v037n09abeh001694.

[130] Ø. Mikkelsen and K. H. Schrøder, “Amalgam Electrodes for Electroanalysis,” *Electroanalysis*, vol. 15, no. 8, pp. 679–687, Jun. 2003, doi: 10.1002/elan.200390085.

[131] V. P. Shvedov and P. G. Antonov, “Separation of Praseodymium and Neodymium by Electrolysis of a Mercury Cathode,” *Radiokhimiya*, vol. 5, no. 3, pp. 342–346, 1962, doi: 10.1017/CBO9781107415324.004.

[132] W. R. Fawcett, “Potential dependence of the elementary steps in the kinetics of electrode reactions involving amalgam formation,” *J. Phys. Chem.*, vol. 93, no. 6, pp. 2675–2682, 1989.

[133] G. M. Kolesov and L. N. Pankratova, “Separation of rare-earth elements by electrolysis at a mercury cathode,” *Russ. Chem. Rev.*, vol. 37, no. 9, p. 701, 1968.

[134] H. N. McCoy, “Europium and ytterbium amalgams,” *J. Am. Chem. Soc.*, vol. 63, no. 6, pp. 1622–1624, 1941.

[135] H. N. Mccoy, H. Morris, and P. W. Selwood, “Europium Amalgam: Separation of Europium from Rare Earth Mixtures,” *Inorganic Syntheses*. pp. 65–69, Jan. 01, 1946, doi: doi:10.1002/9780470132333.ch18.

[136] H. Wang, H. Yuan, S. S. Hong, Y. Li, and Y. Cui, “Physical and chemical tuning of two-dimensional transition metal dichalcogenides,” *Chem. Soc. Rev.*, vol. 44, no. 9, pp. 2664–2680, 2015.

[137] M. Chhowalla, H. S. Shin, G. Eda, L.-J. Li, K. P. Loh, and H. Zhang, “The chemistry of two-dimensional layered transition metal dichalcogenide nanosheets,” *Nat. Chem.*, vol. 5, no. 4, pp. 263–275, 2013.

[138] W. R. McKinnon and R. R. Haering, “Physical mechanisms of intercalation,” *Mod. Asp. Electrochem.*, pp. 235–304, 1983.

[139] J. Zhou *et al.*, “Layered intercalation materials,” *Adv. Mater.*, vol. 33, no. 25, p. 2004557, 2021.

[140] M. S. Whittingham, *Intercalation chemistry: an introduction*. Academic Press New York, 1982.

[141] Y. Jung, Y. Zhou, and J. J. Cha, “Intercalation in two-dimensional transition metal chalcogenides,” *Inorg. Chem. Front.*, vol. 3, no. 4, pp. 452–463, 2016.

[142] M. S. Whittingham, “Lithium batteries: 50 years of advances to address the next 20 years of climate issues,” *Nano Letters*, vol. 20, no. 12. ACS Publications, pp. 8435–8437, 2020.

[143] F. L. Vogel, G. M. T. Foley, C. Zeller, E. R. Falardeau, and J. Gan, “High electrical conductivity in graphite intercalated with acid fluorides,” *Mater. Sci. Eng.*, vol. 31, pp. 261–265, 1977.

[144] D. Ghosh, P. Devi, and P. Kumar, “Intercalation in two-dimensional transition metal chalcogenides: interlayer engineering and applications,” *Prog. Energy*, vol. 4, no. 2, p. 22001, 2022.

[145] K. Li *et al.*, “Aluminum-Ion-Intercalation Supercapacitors with Ultrahigh Areal Capacitance and Highly Enhanced Cycling Stability: Power Supply for Flexible Electrochromic Devices,” *Small*, vol. 13, no. 19, p. 1700380, 2017.

[146] M.-C. Lin *et al.*, “An ultrafast rechargeable aluminium-ion battery,” *Nature*, vol. 520, no. 7547, pp. 324–328, 2015.

[147] T. Koketsu *et al.*, “Reversible magnesium and aluminium ions insertion in cation-deficient anatase TiO2,” *Nat. Mater.*, vol. 16, no. 11, pp. 1142–1148, 2017.

[148] S. Seiler *et al.*, “Effect of friction on oxidative graphite intercalation and high-quality graphene formation,” *Nat. Commun.*, vol. 9, no. 1, pp. 1–9, 2018.

[149] P. Joensen, R. F. Frindt, and S. R. Morrison, “Single-layer mos2,” *Mater. Res. Bull.*, vol. 21, no. 4, pp. 457–461, 1986.

[150] H.-L. Tsai, J. Heising, J. L. Schindler, C. R. Kannewurf, and M. G. Kanatzidis, “Exfoliated−restacked phase of WS2,” *Chem. Mater.*, vol. 9, no. 4, pp. 879–882, 1997.

[151] R. A. Gordon, D. Yang, E. D. Crozier, D. T. Jiang, and R. F. Frindt, “Structures of exfoliated single layers of WS 2, MoS 2, and MoSe 2 in aqueous suspension,” *Phys. Rev. B*, vol. 65, no. 12, p. 125407, 2002.

[152] X. Fan *et al.*, “Fast and efficient preparation of exfoliated 2H MoS2 nanosheets by sonication-assisted lithium intercalation and infrared laser-induced 1T to 2H phase reversion,” *Nano Lett.*, vol. 15, no. 9, pp. 5956–5960, 2015.

[153] E. R. Falardeau, L. R. Hanlon, and T. E. Thompson, “Direct synthesis of stage 1-3 intercalation compounds of arsenic pentafluoride in graphite,” *Inorg. Chem.*, vol. 17, no. 2, pp. 301–303, 1978.

[154] M. S. Dresselhaus and G. Dresselhaus, “Intercalation compounds of graphite,” *Adv. Phys.*, vol. 30, no. 2, pp. 139–326, 1981.

[155] D. E. Nixon and G. S. Parry, “The expansion of the carbon-carbon bond length in potassium graphites,” *J. Phys. C Solid State Phys.*, vol. 2, no. 10, p. 1732, 1969.

[156] T. H. Bointon, I. Khrapach, R. Yakimova, A. V Shytov, M. F. Craciun, and S. Russo, “Approaching magnetic ordering in graphene materials by FeCl3 intercalation,” *Nano Lett.*, vol. 14, no. 4, pp. 1751–1755, 2014.

[157] N. Kim, K. S. Kim, N. Jung, L. Brus, and P. Kim, “Synthesis and electrical characterization of magnetic bilayer graphene intercalate,” *Nano Lett.*, vol. 11, no. 2, pp. 860–865, 2011.

[158] K. Parvez *et al.*, “Exfoliation of graphite into graphene in aqueous solutions of inorganic salts,” *J. Am. Chem. Soc.*, vol. 136, no. 16, pp. 6083–6091, 2014.

[159] N. Liu, P. Kim, J. H. Kim, J. H. Ye, S. Kim, and C. J. Lee, “Large-area atomically thin MoS2 nanosheets prepared using electrochemical exfoliation,” *ACS Nano*, vol. 8, no. 7, pp. 6902–6910, 2014.

[160] X. You, N. Liu, C. J. Lee, and J. J. Pak, “An electrochemical route to MoS2 nanosheets for device applications,” *Mater. Lett.*, vol. 121, pp. 31–35, 2014.

[161] C.-Y. Su, A.-Y. Lu, Y. Xu, F.-R. Chen, A. N. Khlobystov, and L.-J. Li, “High-quality thin graphene films from fast electrochemical exfoliation,” *ACS Nano*, vol. 5, no. 3, pp. 2332–2339, 2011.

[162] F. M. Alcorn, K. L. Kuntz, D. L. Druffel, and S. C. Warren, “Aqueous Intercalation of Graphite at a Near-Neutral pH,” *ACS Appl. Energy Mater.*, vol. 1, no. 9, pp. 5062–5067, 2018.

[163] D. W. Murphy and G. W. Hull Jr, “Monodispersed tantalum disulfide and adsorption complexes with cations,” *J. Chem. Phys.*, vol. 62, no. 3, pp. 973–978, 1975.

[164] D. W. Murphy *et al.*, “Properties of H x TaS2: Correlation between the superconducting T c and an electronic instability in layer compounds,” *J. Chem. Phys.*, vol. 62, no. 3, pp. 967–972, 1975.

[165] M. Burrard-Lucas *et al.*, “Enhancement of the superconducting transition temperature of FeSe by intercalation of a molecular spacer layer,” *Nat. Mater.*, vol. 12, no. 1, pp. 15–19, 2013.

[166] C. Wan *et al.*, “Flexible n-type thermoelectric materials by organic intercalation of layered transition metal dichalcogenide TiS2,” *Nat. Mater.*, vol. 14, no. 6, pp. 622–627, 2015.

[167] F. Xiong *et al.*, “Li intercalation in MoS2: in situ observation of its dynamics and tuning optical and electrical properties,” *Nano Lett.*, vol. 15, no. 10, pp. 6777–6784, 2015.

[168] J. Wan, S. D. Lacey, J. Dai, W. Bao, M. S. Fuhrer, and L. Hu, “Tuning two-dimensional nanomaterials by intercalation: materials, properties and applications,” *Chem. Soc. Rev.*, vol. 45, no. 24, pp. 6742–6765, 2016.

[169] M. S. Stark, K. L. Kuntz, S. J. Martens, and S. C. Warren, “Intercalation of layered materials from bulk to 2D,” *Adv. Mater.*, vol. 31, no. 27, p. 1808213, 2019.

[170] L. Niu, J. N. Coleman, H. Zhang, H. Shin, M. Chhowalla, and Z. Zheng, “Production of two-dimensional nanomaterials via liquid-based direct exfoliation,” *Small*, vol. 12, no. 3, pp. 272–293, 2016.

[171] K. Parvez *et al.*, “Electrochemically exfoliated graphene as solution-processable, highly conductive electrodes for organic electronics,” *ACS Nano*, vol. 7, no. 4, pp. 3598–3606, 2013.

[172] S. Sunohara, K. Nishimura, K. Yahikozawa, M. Ueno, M. Enyo, and Y. Takasu, “Electrocatalysis of transition-metal oxides for reduction and oxidation of nitrite ions,” *J. Electroanal. Chem.*, vol. 354, no. 1–2, pp. 161–171, 1993.

[173] C. E. Langley, B. ŠLJUKIC, C. E. Banks, and R. G. Compton, “Manganese dioxide graphite composite electrodes: application to the electroanalysis of hydrogen peroxide, ascorbic acid and nitrite,” *Anal. Sci.*, vol. 23, no. 2, pp. 165–170, 2007.

[174] A. M. Abdelkader, A. J. Cooper, R. A. W. Dryfe, and I. A. Kinloch, “How to get between the sheets: a review of recent works on the electrochemical exfoliation of graphene materials from bulk graphite,” *Nanoscale*, vol. 7, no. 16, pp. 6944–6956, 2015.

[175] J.-M. Tarascon and M. Armand, “Issues and challenges facing rechargeable lithium batteries,” in *Materials for sustainable energy: a collection of peer-reviewed research and review articles from Nature Publishing Group*, World Scientific, 2011, pp. 171–179.

[176] T. Piao, S. Park, C. Doh, and S. Moon, “Intercalation of lithium ions into graphite electrodes studied by AC impedance measurements,” *J. Electrochem. Soc.*, vol. 146, no. 8, p. 2794, 1999.

[177] B. Dunn, H. Kamath, and J.-M. Tarascon, “Electrical energy storage for the grid: a battery of choices,” *Science (80-.).*, vol. 334, no. 6058, pp. 928–935, 2011.

[178] E. Hitz *et al.*, “Electrochemical intercalation of lithium ions into NbSe2 nanosheets,” *ACS Appl. Mater. Interfaces*, vol. 8, no. 18, pp. 11390–11395, 2016.

[179] G. J. Wang *et al.*, “Electrochemical intercalation of lithium ions into LiV3O8 in an aqueous electrolyte,” *J. Power Sources*, vol. 189, no. 1, pp. 503–506, 2009.

[180] C. Delmas, J.-J. Braconnier, C. Fouassier, and P. Hagenmuller, “Electrochemical intercalation of sodium in NaxCoO2 bronzes,” *Solid State Ionics*, vol. 3, pp. 165–169, 1981.

[181] P. Hartmann *et al.*, “A rechargeable room-temperature sodium superoxide (NaO2) battery,” *Nat. Mater.*, vol. 12, no. 3, pp. 228–232, 2013.

[182] S. Komaba, C. Takei, T. Nakayama, A. Ogata, and N. Yabuuchi, “Electrochemical intercalation activity of layered NaCrO2 vs. LiCrO2,” *Electrochem. commun.*, vol. 12, no. 3, pp. 355–358, 2010.

[183] Y. Kim, K. Ha, S. M. Oh, and K. T. Lee, “High-capacity anode materials for sodium-ion batteries,” *Chem. Eur. J.*, vol. 20, no. 38, pp. 11980–11992, 2014.

[184] V. Palomares, P. Serras, I. Villaluenga, K. B. Hueso, J. Carretero-González, and T. Rojo, “Na-ion batteries, recent advances and present challenges to become low cost energy storage systems,” *Energy Environ. Sci.*, vol. 5, no. 3, pp. 5884–5901, 2012.

[185] R. Rajagopalan, Y. Tang, X. Ji, C. Jia, and H. Wang, “Advancements and challenges in potassium ion batteries: a comprehensive review,” *Adv. Funct. Mater.*, vol. 30, no. 12, p. 1909486, 2020.

[186] Z. Jian, Z. Xing, C. Bommier, Z. Li, and X. Ji, “Hard carbon microspheres: potassium-ion anode versus sodium-ion anode,” *Adv. Energy Mater.*, vol. 6, no. 3, p. 1501874, 2016.

[187] X. Ren, Q. Zhao, W. D. McCulloch, and Y. Wu, “MoS2 as a long-life host material for potassium ion intercalation,” *Nano Res.*, vol. 10, no. 4, pp. 1313–1321, 2017.

[188] W. Luo *et al.*, “Potassium ion batteries with graphitic materials,” *Nano Lett.*, vol. 15, no. 11, pp. 7671–7677, 2015.

[189] L. Kang, M. Cui, Z. Zhang, and F. Jiang, “Rechargeable Aqueous Zinc-Ion Batteries with Mild Electrolytes: A Comprehensive Review,” *Batter. Supercaps*, vol. 3, no. 10, pp. 966–1005, 2020.

[190] H. Liang *et al.*, “Aqueous zinc-ion storage in MoS2 by tuning the intercalation energy,” *Nano Lett.*, vol. 19, no. 5, pp. 3199–3206, 2019.

[191] N. Zhang *et al.*, “Rechargeable aqueous zinc-manganese dioxide batteries with high energy and power densities,” *Nat. Commun.*, vol. 8, no. 1, pp. 1–9, 2017.

[192] G. G. Yadav *et al.*, “Regenerable Cu-intercalated MnO2 layered cathode for highly cyclable energy dense batteries,” *Nat. Commun.*, vol. 8, no. 1, pp. 1–9, 2017.

[193] S.-C. Pang, M. A. Anderson, and T. W. Chapman, “Novel Electrode Materials for Thin-Film Ultracapacitors: Comparison of Electrochemical Properties of Sol-Gel-Derived and Electrodeposited Manganese Dioxide,” *J. Electrochem. Soc.*, vol. 147, no. 2, p. 444, 2000, doi: 10.1149/1.1393216.

[194] M. Toupin, T. Brousse, and D. Bélanger, “Charge storage mechanism of MnO2 electrode used in aqueous electrochemical capacitor,” *Chem. Mater.*, vol. 16, no. 16, pp. 3184–3190, 2004.

[195] M. Kühne, F. Paolucci, J. Popovic, P. M. Ostrovsky, J. Maier, and J. H. Smet, “Ultrafast lithium diffusion in bilayer graphene,” *Nat. Nanotechnol.*, vol. 12, no. 9, pp. 895–900, 2017.

[196] Y. Wang *et al.*, “Electrochemical control of photoluminescence in two-dimensional MoS2 nanoflakes,” *ACS Nano*, vol. 7, no. 11, pp. 10083–10093, 2013.

[197] A. P. Abbott and K. J. McKenzie, “Application of ionic liquids to the electrodeposition of metals,” *Phys. Chem. Chem. Phys.*, vol. 8, no. 37, pp. 4265–4279, 2006.

[198] S. Venkatesh and B. V Tilak, “Chlor-alkali technology.” ACS Publications, 1983.

[199] J. Crook and A. Mousavi, “The chlor-alkali process: A review of history and pollution,” *Environ. Forensics*, vol. 17, no. 3, pp. 211–217, 2016.

[200] E. I. Onstott, “Separation of the Lanthons at Amalgam Cathodes: Measurement of the separability of Praseodymium and Neodymium in Aqueous Lithium Citrates Electrodes.,” *Anal. Chem.*, 1961, doi: 10.1021/ac60179a006.

[201] L. Airey, “The Application of the Cathode Ray Oscillograph to Polarography: General Lay-Out and Uses of the Cathode Ray Polarograph,” *Analyst*, vol. 72, no. 856, pp. 304–307, 1947.

[202] N. J. Langford and R. E. Ferner, “Toxicity of mercury,” *J. Hum. Hypertens.*, vol. 13, no. 10, pp. 651–656, 1999, doi: 10.1038/sj.jhh.1000896.

[203] P. Surmann and H. Zeyat, “Voltammetric analysis using a self-renewable non-mercury electrode,” *Anal. Bioanal. Chem.*, vol. 383, no. 6, pp. 1009–1013, 2005, doi: 10.1007/s00216-005-0069-7.

[204] Y. Chung and C.-W. Lee, “Electrochemistry of gallium,” *J. Electrochem. Sci. Technol.*, vol. 4, no. 1, pp. 1–18, 2013.

[205] D. Belaschk, “Zum elektrochemischen Verhalten des Galliums in wäßrigen Elektrolytlösungen,” *Zeitschrift für Phys. Chemie*, vol. 234, no. 1, pp. 258–279, 1967.

[206] M. Pourbaix, “Atlas of electrochemical equilibria in aqueous solution,” *NACE*, vol. 307, 1974.

[207] D. O. Flamini, S. B. Saidman, and J. B. Bessone, “Electrodeposition of gallium onto vitreous carbon,” *J. Appl. Electrochem.*, vol. 37, no. 4, pp. 467–471, 2007.

[208] W. Monnens, P.-C. Lin, C. Deferm, K. Binnemans, and J. Fransaer, “Electrochemical behavior and electrodeposition of gallium in 1, 2-dimethoxyethane-based electrolytes,” *Phys. Chem. Chem. Phys.*, 2021.

[209] B. Hong *et al.*, “EQCM study on the electrochemical redox behavior of gallium in alkaline solution,” *Hydrometallurgy*, vol. 194, p. 105344, 2020, doi: https://doi.org/10.1016/j.hydromet.2020.105344.

[210] C. J. Powell, “Characteristic energy losses of 8-keV electrons in liquid Al, Bi, In, Ga, Hg, and Au,” *Phys. Rev.*, vol. 175, no. 3, p. 972, 1968.

[211] J.-E. Park *et al.*, “Rewritable, printable conducting liquid metal hydrogel,” *ACS Nano*, vol. 13, no. 8, pp. 9122–9130, 2019.

[212] D. Wang *et al.*, “Shape-transformable, fusible rodlike swimming liquid metal nanomachine,” *ACS Nano*, vol. 12, no. 10, pp. 10212–10220, 2018.

[213] M. Mayyas *et al.*, “Pulsing liquid alloys for nanomaterials synthesis,” *ACS Nano*, vol. 14, no. 10, pp. 14070–14079, 2020.

[214] J. Han *et al.*, “Liquid metal enabled continuous flow reactor: A proof-of-concept,” *Matter*, vol. 4, no. 12, pp. 4022–4041, 2021.

[215] M. B. Ghasemian *et al.*, “Self-limiting galvanic growth of MnO2 monolayers on a liquid metal—applied to photocatalysis,” *Adv. Funct. Mater.*, vol. 29, no. 36, p. 1901649, 2019.

[216] B. Lertanantawong, P. Lertsathitphong, and A. P. O’Mullane, “Chemical reactivity of Ga-based liquid metals with redox active species and its influence on electrochemical processes,” *Electrochem. commun.*, vol. 93, pp. 15–19, 2018.

[217] Y. Wang, S. Wang, H. Chang, and W. Rao, “Galvanic replacement of liquid metal/reduced graphene oxide frameworks,” *Adv. Mater. Interfaces*, vol. 7, no. 19, p. 2000626, 2020.

[218] A. Varadharaj and G. P. Rao, “Cyclic voltammetric studies on gallium film electrodes in alkaline media,” in *Proceedings of the Indian Academy of Sciences-Chemical Sciences*, 1990, vol. 102, no. 2, pp. 177–187.

[219] A. Tsvetanova, E. I. Sokolova, and S. N. Raicheva, “Mechanism of Anodic-Dissolution of Gallium in Acidic Aqueous-Solutions,” *SOVIET ELECTROCHEMISTRY*, vol. 15, no. 2. PLENUM PUBL CORP CONSULTANTS BUREAU, 233 SPRING ST, NEW YORK, NY 10013, pp. 185–188, 1979.

[220] R. S. Perkins, “Anodic oxidation of gallium in alkaline solution,” *J. Electroanal. Chem. Interfacial Electrochem.*, vol. 101, no. 1, pp. 47–57, 1979, doi: https://doi.org/10.1016/S0022-0728(79)80078-9.

[221] R. S. Perkins, “Gallium oxidation in alkaline solution,” *J Electrochem Soc*, vol. 119, no. 6, pp. 713–715, 1972.

[222] M. A. Creighton, M. C. Yuen, M. A. Susner, Z. Farrell, B. Maruyama, and C. E. Tabor, “Oxidation of Gallium-based Liquid Metal Alloys by Water,” *Langmuir*, vol. 36, no. 43, pp. 12933–12941, 2020.

[223] R. S. Nicholson and I. Shain, “Theory of stationary electrode polarography. Single scan and cyclic methods applied to reversible, irreversible, and kinetic systems.,” *Anal. Chem.*, vol. 36, no. 4, pp. 706–723, 1964.

[224] G. Wang, J. Park, X. Kong, P. R. Wilson, Z. Chen, and J. Ahn, “Facile Synthesis and Characterization of Gallium Oxide (β-Ga 2O 3) 1D Nanostructures: Nanowires, Nanoribbons, and Nanosheets,” *Cryst. Growth Des.*, vol. 8, no. 6, pp. 1940–1944, 2008.

[225] J. Zarembowitch, J. Gouteron, and A. M. Lejus, “Raman spectra of lanthanide sesquioxide single crystals with A-type structure,” *Phys. status solidi*, vol. 94, no. 1, pp. 249–256, 1979.

[226] J. Gouteron, D. Michel, A. M. Lejus, and J. Zarembowitch, “Raman spectra of lanthanide sesquioxide single crystals: Correlation between A and B-type structures,” *J. Solid State Chem.*, vol. 38, no. 3, pp. 288–296, 1981.

[227] D. K. Walanda, G. A. Lawrance, and S. W. Donne, “Hydrothermal MnO2: Synthesis, structure, morphology and discharge performance,” *J. Power Sources*, vol. 139, no. 1–2, pp. 325–341, 2005.

[228] K.-H. Kim, J.-Y. Kim, and K.-B. Kim, “Facile coating of poly (3, 4-ethylenedioxythiophene) on manganese dioxide by galvanic displacement reaction and its electrochemical properties for electrochemical capacitors,” *Bull. Korean Chem. Soc.*, vol. 33, no. 8, pp. 2529–2534, 2012.

[229] H. Jung *et al.*, “Redox cycling driven transformation of layered manganese oxides to tunnel structures,” *J. Am. Chem. Soc.*, vol. 142, no. 5, pp. 2506–2513, 2020.

[230] G. J. Islam, H. M. N. Akhtar, M. A. Mamun, and M. Q. Ehsan, “Investigations on the redox behaviour of manganese in manganese (II)–saccharin and manganese (II)–saccharin–1, 10-phenanthroline complexes,” *J. Saudi Chem. Soc.*, vol. 13, no. 2, pp. 177–183, 2009.

[231] N. Jabeen, Q. Xia, S. V Savilov, S. M. Aldoshin, Y. Yu, and H. Xia, “Enhanced pseudocapacitive performance of α-MnO2 by cation preinsertion,” *ACS Appl. Mater. Interfaces*, vol. 8, no. 49, pp. 33732–33740, 2016.

[232] Y. Jiang and J. Liu, “Definitions of pseudocapacitive materials: a brief review,” *Energy Environ. Mater.*, vol. 2, no. 1, pp. 30–37, 2019.

[233] V. Augustyn, P. Simon, and B. Dunn, “Pseudocapacitive oxide materials for high-rate electrochemical energy storage,” *Energy Environ. Sci.*, vol. 7, no. 5, pp. 1597–1614, 2014.

[234] X. Yu *et al.*, “Emergent pseudocapacitance of 2D nanomaterials,” *Adv. Energy Mater.*, vol. 8, no. 13, p. 1702930, 2018.

[235] H. Y. Lee and J. B. Goodenough, “Supercapacitor behavior with KCl electrolyte,” *J. Solid State Chem.*, vol. 144, no. 1, pp. 220–223, 1999.

[236] S. Wen, J.-W. Lee, I.-H. Yeo, J. Park, and S. Mho, “The role of cations of the electrolyte for the pseudocapacitive behavior of metal oxide electrodes, MnO2 and RuO2,” *Electrochim. Acta*, vol. 50, no. 2, pp. 849–855, 2004, doi: https://doi.org/10.1016/j.electacta.2004.02.056.

[237] J. Shin, J. K. Seo, R. Yaylian, A. Huang, and Y. S. Meng, “A review on mechanistic understanding of MnO2 in aqueous electrolyte for electrical energy storage systems,” *Int. Mater. Rev.*, vol. 65, no. 6, pp. 356–387, 2020.

[238] R. J. Gummow, A. De Kock, and M. M. Thackeray, “Improved capacity retention in rechargeable 4 V lithium/lithium-manganese oxide (spinel) cells,” *Solid State Ionics*, vol. 69, no. 1, pp. 59–67, 1994.

[239] R. N. Reddy and R. G. Reddy, “Sol–gel MnO2 as an electrode material for electrochemical capacitors,” *J. Power Sources*, vol. 124, no. 1, pp. 330–337, 2003.

[240] H. Pan *et al.*, “Reversible aqueous zinc/manganese oxide energy storage from conversion reactions,” *Nat. Energy*, vol. 1, no. 5, pp. 1–7, 2016.

[241] M. Chamoun, W. R. Brant, C.-W. Tai, G. Karlsson, and D. Noréus, “Rechargeability of aqueous sulfate Zn/MnO2 batteries enhanced by accessible Mn2+ ions,” *Energy Storage Mater.*, vol. 15, pp. 351–360, 2018.

[242] J. Huang *et al.*, “Polyaniline-intercalated manganese dioxide nanolayers as a high-performance cathode material for an aqueous zinc-ion battery,” *Nat. Commun.*, vol. 9, no. 1, pp. 1–8, 2018.

[243] D. Wu *et al.*, “Quantitative temporally and spatially resolved X-ray fluorescence microprobe characterization of the manganese dissolution-deposition mechanism in aqueous Zn/α-MnO 2 batteries,” *Energy Environ. Sci.*, vol. 13, no. 11, pp. 4322–4333, 2020.

[244] W. Sun *et al.*, “Zn/MnO2 battery chemistry with H+ and Zn2+ coinsertion,” *J. Am. Chem. Soc.*, vol. 139, no. 29, pp. 9775–9778, 2017.

[245] M. Yoshio, R. J. Brodd, and A. Kozawa, *Lithium-ion batteries*, vol. 1. Springer, 2009.

[246] Z. X. Shu, R. S. McMillan, and J. J. Murray, “Electrochemical intercalation of lithium into graphite,” *J. Electrochem. Soc.*, vol. 140, no. 4, p. 922, 1993.

[247] J. Li, C. Daniel, and D. Wood, “Materials processing for lithium-ion batteries,” *J. Power Sources*, vol. 196, no. 5, pp. 2452–2460, 2011.

[248] T. S. Mathis, N. Kurra, X. Wang, D. Pinto, P. Simon, and Y. Gogotsi, “Energy storage data reporting in perspective—guidelines for interpreting the performance of electrochemical energy storage systems,” *Adv. Energy Mater.*, vol. 9, no. 39, p. 1902007, 2019.

[249] Y. Liu, S. P. Jiang, and Z. Shao, “Intercalation pseudocapacitance in electrochemical energy storage: recent advances in fundamental understanding and materials development,” *Mater. Today Adv.*, vol. 7, p. 100072, 2020.

[250] R. Kötz and M. Carlen, “Principles and applications of electrochemical capacitors,” *Electrochim. Acta*, vol. 45, no. 15–16, pp. 2483–2498, 2000.

[251] W. G. Pell and B. E. Conway, “Peculiarities and requirements of asymmetric capacitor devices based on combination of capacitor and battery-type electrodes,” *J. Power Sources*, vol. 136, no. 2, pp. 334–345, 2004.

[252] B. E. Conway, *Electrochemical supercapacitors: scientific fundamentals and technological applications*. Springer Science & Business Media, 2013.

[253] V. Augustyn *et al.*, “High-rate electrochemical energy storage through Li+ intercalation pseudocapacitance,” *Nat. Mater.*, vol. 12, no. 6, pp. 518–522, 2013.

[254] W. Zuo, R. Li, C. Zhou, Y. Li, J. Xia, and J. Liu, “Battery-supercapacitor hybrid devices: recent progress and future prospects,” *Adv. Sci.*, vol. 4, no. 7, p. 1600539, 2017.

[255] J. W. Kim, V. Augustyn, and B. Dunn, “The effect of crystallinity on the rapid pseudocapacitive response of Nb2O5,” *Adv. Energy Mater.*, vol. 2, no. 1, pp. 141–148, 2012.

[256] M. Zukalová, M. Kalbác, L. Kavan, I. Exnar, and M. Graetzel, “Pseudocapacitive lithium storage in TiO2 (B),” *Chem. Mater.*, vol. 17, no. 5, pp. 1248–1255, 2005.

[257] K. Zhu, Q. Wang, J.-H. Kim, A. A. Pesaran, and A. J. Frank, “Pseudocapacitive lithium-ion storage in oriented anatase TiO2 nanotube arrays,” *J. Phys. Chem. C*, vol. 116, no. 22, pp. 11895–11899, 2012.

[258] J. B. Cook *et al.*, “Mesoporous MoS2 as a transition metal dichalcogenide exhibiting pseudocapacitive Li and Na-ion charge storage,” *Adv. Energy Mater.*, vol. 6, no. 9, p. 1501937, 2016.

[259] D. Chao *et al.*, “Pseudocapacitive Na-ion storage boosts high rate and areal capacity of self-branched 2D layered metal chalcogenide nanoarrays,” *ACS Nano*, vol. 10, no. 11, pp. 10211–10219, 2016.

[260] C. An *et al.*, “Graphene wrapped FeSe2 nano-microspheres with high pseudocapacitive contribution for enhanced Na-ion storage,” *Adv. Energy Mater.*, vol. 9, no. 18, p. 1900356, 2019.

[261] D. Cheng *et al.*, “Electrochemical storage mechanism of sodium in carbon materials: A study from soft carbon to hard carbon,” *Carbon N. Y.*, vol. 182, pp. 758–769, 2021.

[262] Q. Liu *et al.*, “Super long-life potassium-ion batteries based on an antimony@ carbon composite anode,” *Chem. Commun.*, vol. 54, no. 83, pp. 11773–11776, 2018.

[263] N. Li, F. Zhang, and Y. Tang, “Hierarchical T-Nb 2 O 5 nanostructure with hybrid mechanisms of intercalation and pseudocapacitance for potassium storage and high-performance potassium dual-ion batteries,” *J. Mater. Chem. A*, vol. 6, no. 37, pp. 17889–17895, 2018.

[264] Y. Wang *et al.*, “Hyperporous sponge interconnected by hierarchical carbon nanotubes as a high-performance potassium-ion battery anode,” *Adv. Mater.*, vol. 30, no. 32, p. 1802074, 2018.

[265] M. El Makrini, D. Guerard, P. Lagrange, and A. Hérold, “Intercalation of rare earth metals in graphite,” *Phys. B+ C*, vol. 99, no. 1, pp. 481–485, 1980.

[266] A. M. Shikin, S. L. Molodtsov, C. Laubschat, G. Kaindl, G. V Prudnikova, and V. K. Adamchuk, “Electronic structure of La-intercalated graphite,” *Phys. Rev. B*, vol. 51, no. 19, p. 13586, 1995.

[267] R. C. Vickery and N. L. Campbell, “Rare earth graphite intercalates,” *J. Am. Chem. Soc.*, vol. 79, no. 22, pp. 5897–5899, 1957.

[268] Y. Wen *et al.*, “Expanded graphite as superior anode for sodium-ion batteries,” *Nat. Commun.*, vol. 5, no. 1, p. 4033, 2014.

[269] Y. Cao *et al.*, “Sodium ion insertion in hollow carbon nanowires for battery applications,” *Nano Lett.*, vol. 12, no. 7, pp. 3783–3787, 2012.

[270] V. A. da Silva and M. C. Rezende, “Effect of the morphology and structure on the microwave absorbing properties of multiwalled carbon nanotube filled epoxy resin nanocomposites,” *Mater. Res.*, vol. 21, 2018.

[271] P. Toth, “Nanostructure quantification of turbostratic carbon by HRTEM image analysis: State of the art, biases, sensitivity and best practices,” *Carbon N. Y.*, vol. 178, pp. 688–707, 2021.

[272] T. Ungar, J. Gubicza, G. Ribarik, C. Pantea, and T. W. Zerda, “Microstructure of carbon blacks determined by X-ray diffraction profile analysis,” *Carbon N. Y.*, vol. 40, no. 6, pp. 929–937, 2002.

[273] Z. Q. Li, C. J. Lu, Z. P. Xia, Y. Zhou, and Z. Luo, “X-ray diffraction patterns of graphite and turbostratic carbon,” *Carbon N. Y.*, vol. 45, no. 8, pp. 1686–1695, 2007.

[274] Y. Li, Y. Lu, P. Adelhelm, M.-M. Titirici, and Y.-S. Hu, “Intercalation chemistry of graphite: alkali metal ions and beyond,” *Chem. Soc. Rev.*, vol. 48, no. 17, pp. 4655–4687, 2019.

[275] Y. Liu, J. S. Xue, T. Zheng, and J. R. Dahn, “Mechanism of lithium insertion in hard carbons prepared by pyrolysis of epoxy resins,” *Carbon N. Y.*, vol. 34, no. 2, pp. 193–200, 1996.

[276] W. Luo *et al.*, “Electrochemically expandable soft carbon as anodes for Na-ion batteries,” *ACS Cent. Sci.*, vol. 1, no. 9, pp. 516–522, 2015.

[277] X. Yao *et al.*, “Defect-rich soft carbon porous nanosheets for fast and high-capacity sodium-ion storage,” *Adv. Energy Mater.*, vol. 9, no. 6, p. 1803260, 2019.

[278] D. A. Stevens and J. R. Dahn, “High capacity anode materials for rechargeable sodium-ion batteries,” *J. Electrochem. Soc.*, vol. 147, no. 4, p. 1271, 2000.

[279] B. Hou *et al.*, “Self-supporting, flexible, additive-free, and scalable hard carbon paper self-interwoven by 1D microbelts: superb room/low-temperature sodium storage and working mechanism,” *Adv. Mater.*, vol. 31, no. 40, p. 1903125, 2019.

[280] J. Choi, M. E. Lee, S. Lee, H.-J. Jin, and Y. S. Yun, “Pyroprotein-derived hard carbon fibers exhibiting exceptionally high plateau capacities for sodium ion batteries,” *ACS Appl. Energy Mater.*, vol. 2, no. 2, pp. 1185–1191, 2019.

[281] S. Alvin *et al.*, “Revealing sodium ion storage mechanism in hard carbon,” *Carbon N. Y.*, vol. 145, pp. 67–81, 2019.

[282] P. Bai, Y. He, X. Zou, X. Zhao, P. Xiong, and Y. Xu, “Elucidation of the sodium-storage mechanism in hard carbons,” *Adv. Energy Mater.*, vol. 8, no. 15, p. 1703217, 2018.

[283] A. Krause, P. Kossyrev, M. Oljaca, S. Passerini, M. Winter, and A. Balducci, "Electrochemical double layer capacitor and lithium-ion capacitor based on carbon black," *J. Power Sources*, vol. 196, no. 20, pp. 8836–8842, 2011.

[284] L. L. Zhang and X. S. Zhao, "Carbon-based materials as supercapacitor electrodes," *Chem. Soc. Rev.*, vol. 38, no. 9, pp. 2520–2531, 2009.

[285] T. Brousse, D. Bélanger, and J. W. Long, "To be or not to be pseudocapacitive?," *J. Electrochem. Soc.*, vol. 162, no. 5, p. A5185, 2015.

[286] S. Pérez-Rodríguez, E. Pastor, and M. J. Lázaro, "Electrochemical behavior of the carbon black Vulcan XC-72R: Influence of the surface chemistry," *Int. J. Hydrogen Energy*, vol. 43, no. 16, pp. 7911–7922, 2018.

[287] Y. Tang, Y. Liu, S. Yu, F. Gao, and Y. Zhao, "Comparative study on three commercial carbons for supercapacitor applications," *Russ. J. Electrochem.*, vol. 51, no. 1, pp. 77–85, 2015.

[288] V. Sahu *et al.*, "Synthesis of hydrophilic carbon black; role of hydrophilicity in maintaining the hydration level and protonic conduction," *RSC Adv.*, vol. 3, no. 12, pp. 3917–3924, 2013.

[289] S. Mu, Q. Liu, P. Kidkhunthod, X. Zhou, W. Wang, and Y. Tang, "Molecular grafting towards high-fraction active nanodots implanted in N-doped carbon for sodium dual-ion batteries," *Natl. Sci. Rev.*, vol. 8, no. 7, p. nwaa178, 2021.

[290] W. Kang *et al.*, "Nanostructured porous manganese carbonate spheres with capacitive effects on the high lithium storage capability," *Nanoscale*, vol. 7, no. 22, pp. 10146–10151, 2015.

[291] A. S. Medina, C. F. Ivory, N. A. Wall, S. B. Clark, and H. Beyenal, "Electrochemical preconcentration mechanism of trivalent lanthanum," *J. Electrochem. Soc.*, vol. 165, no. 13, p. D654, 2018.

[292] B. Cao, H. Liu, B. Xu, Y. Lei, X. Chen, and H. Song, "Mesoporous soft carbon as an anode material for sodium ion batteries with superior rate and cycling performance," *J. Mater. Chem. A*, vol. 4, no. 17, pp. 6472–6478, 2016.

[293] Z. Jian *et al.*, "Insights on the mechanism of Na-ion storage in soft carbon anode," *Chem. Mater.*, vol. 29, no. 5, pp. 2314–2320, 2017.

[294] M. A. Short and P. L. Walker Jr, "Measurement of interlayer spacings and crystal sizes in turbostratic carbons," *Carbon N. Y.*, vol. 1, no. 1, pp. 3–9, 1963.

[295] M. M. Fares, F. A. A. Al-Rub, and A. R. Mohammad, "Ultimate eradication of the ciprofloxacin antibiotic from the ecosystem by nanohybrid GO/O-CNTs," *ACS omega*, vol. 5, no. 9, pp. 4457–4468, 2020.

[296] S. N. C. Ortiz, R. Cabanzo, and E. Mejia-Ospino, “Crude oil/water emulsion separation using graphene oxide and amine-modified graphene oxide particles,” *Fuel*, vol. 240, pp. 162–168, 2019.

[297] T. Zheng, Q. Zhong, and J. R. Dahn, “High-Capacity Carbons Prepared from Phenolic Resin for Anodes of Lithium-Ion Batteries,” *J. Electrochem. Soc.*, vol. 142, no. 11, p. L211, 1995.

[298] T. Zheng, Y. Liu, E. W. Fuller, S. Tseng, U. Von Sacken, and J. R. Dahn, “Lithium insertion in high capacity carbonaceous materials,” *J. Electrochem. Soc.*, vol. 142, no. 8, p. 2581, 1995.

[299] T. Zheng, J. N. Reimers, and J. R. Dahn, “Effect of turbostratic disorder in graphitic carbon hosts on the intercalation of lithium,” *Phys. Rev. B*, vol. 51, no. 2, p. 734, 1995.

[300] H. Ru, K. Xiang, W. Zhou, Y. Zhu, X. S. Zhao, and H. Chen, “Bean-dreg-derived carbon materials used as superior anode material for lithium-ion batteries,” *Electrochim. Acta*, vol. 222, pp. 551–560, 2016.

[301] R. Li *et al.*, “Controlling the thickness of disordered turbostratic nanodomains in hard carbon with enhanced sodium storage performance,” *Energy Technol.*, vol. 6, no. 6, pp. 1080–1087, 2018.

[302] U. A. do Rego, R. Sgarbi, T. Lopes, C. C. dos Santos, A. A. Tanaka, and E. A. Ticianelli, “Effect of Substrate and Pyrolysis Atmosphere of FeNx Materials on Electrocatalysis of the Oxygen Reduction Reaction,” *Electrocatalysis*, vol. 12, no. 5, pp. 548–563, 2021.

[303] L. R. B. Elton and D. F. Jackson, “X-ray diffraction and the Bragg law,” *Am. J. Phys.*, vol. 34, no. 11, pp. 1036–1038, 1966.

[304] B. Greenberg, “Bragg’s law with refraction,” *Acta Crystallogr. Sect. A Found. Crystallogr.*, vol. 45, no. 3, pp. 238–241, 1989.

[305] T. Denaro *et al.*, “Investigation of low cost carbonaceous materials for application as counter electrode in dye-sensitized solar cells,” *J. Appl. Electrochem.*, vol. 39, no. 11, pp. 2173–2179, 2009.

[306] M. C. G. Pedrosa, J. C. Dutra Filho, L. R. de Menezes, and E. O. da Silva, “Chemical Surface Modification and Characterization of Carbon Nanostructures Without Shape Damage,” *Mater. Res.*, vol. 23, 2020.

[307] A. M. Abbas and F. H. Hussein, “Synthesis of few-wall carbon nanotubes using methanol/propanol mixture by chemical vapour deposition,” 2017.

[308] Y. Cui, Z. Yuan, W. Bao, Q. Zhuang, and Z. Sun, “Investigation of lithium ion kinetics through LiMn 2 O 4 electrode in aqueous Li 2 SO 4 electrolyte,” *J. Appl. Electrochem.*, vol. 42, pp. 883–891, 2012.

[309] V. A. Agubra and J. W. Fergus, “The formation and stability of the solid electrolyte interface on the graphite anode,” *J. Power Sources*, vol. 268, pp. 153–162, 2014.

[310] J. Vetter *et al.*, “Ageing mechanisms in lithium-ion batteries,” *J. Power Sources*, vol. 147, no. 1–2, pp. 269–281, 2005.

[311] Y. Chen, H. Huang, L. Liu, Y. Chen, and Y. Han, “Diffusion enhancement to stabilize solid electrolyte interphase,” *Adv. Energy Mater.*, vol. 11, no. 40, p. 2101774, 2021.

[312] T. W. Napporn *et al.*, “Chapter 9 - Electrochemical Measurement Methods and Characterization on the Cell Level,” V. Hacker and S. B. T.-F. C. and H. Mitsushima, Eds. Elsevier, 2018, pp. 175–214.

[313] R. J. Mortimer, “Spectroelectrochemistry, Methods and Instrumentation,” J. C. Lindon, G. E. Tranter, and D. W. B. T.-E. of S. and S. (Third E. Koppenaal, Eds. Oxford: Academic Press, 2017, pp. 172–177.

[314] D. D. Macdonald, “Chronopotentiometry,” in *Transient Techniques in Electrochemistry*, Springer, 1977, pp. 119–184.